ENVIRONMENTAL APPLICATION AND IMPLICATION OF ENGINEERED NANOMATERIALS IN SOIL, WATER, AND PLANT SYSTEMS

By

Jianzhou He

A DISSERTATION

Submitted to
Michigan State University
in partial fulfillment of the requirements
for the degree of

Crop and Soil Sciences – Environmental Toxicology – Doctor of Philosophy

2020

ABSTRACT

ENVIRONMENTAL APPLICATION AND IMPLICATION OF ENGINEERED NANOMATERIALS IN SOIL, WATER, AND PLANT SYSTEMS

By

Jianzhou He

Nanotechnology is promising to develop novel engineered nanomaterials (ENMs) for industrial and consumer products, environmental engineering, and agricultural production. Specifically, ENMs can be used to remove contaminants from wastewater and to produce plant care agrochemicals (e.g., nanopesticides). The rapidly growing use of nano-enabled products is leading to increased release of ENMs into agroecosystems and their uptake by organisms and crop plants, thus posing potential threats to environmental and human health. To maximize environmental benefits and minimize potential risks of ENMs, this dissertation research focused on both environmental application and implication of ENMs in soil, water, and plant systems.

The first study systematically investigated the photodegradation of antibiotic cephalexin (as an emerging contaminant in water) by novel ZnO nanowires under simulated sunlight through a combination of experimental and theoretical techniques including kinetic batch degradation, free radical trapping experiments, degradation product identification by mass spectrometry, and molecular computation. The ZnO nanowires substantially increased the degradation efficiency of cephalexin, especially under circumneutral and alkaline conditions (pH of 7.2–9.2). Anions (HCO_3^-) and natural organic matter inhibited the photodegradation of cephalexin by scavenging radical species (•OH and $•O_2^-$). Finally, cephalexin photodegradation pathways included hydroxylation, demethylation, decarboxylation, and dealkylation. Overall, the ZnO nanowires can be potentially used for removing antibiotics from contaminated water.

The second study examined the effect of biochar amendments on soil sorption of Ag NPs and Ag^+, their soil-bound fractions, and their uptake and translocation by radishes grown in a loamy sand soil spiked with 1 mg kg^{-1} Ag NPs or Ag^+. Biochar amendment had no significant effect on Ag uptake by radishes, which also did not differ with and without Ag addition. Results of Ag sorption, soil-bound fractions, and soil pore water concentrations showed that the bioavailable Ag at the environmentally-relevant concentration (1 mg/kg) was low, which may partially explain the non-significant effect of biochar amendment on the Ag uptake. This study demonstrated that the accumulation risk of Ag NPs and Ag^+ ions in vegetable crops at environmentally-relevant concentrations is very low.

The third study addressed the role of stomata in the internalization of Ag NPs using abscisic acid (ABA)-responsive ecotypes (Ler and Col-7) and ABA-insensitive mutants (*ost1-2* and *scord7*) of *Arabidopsis thaliana* in batch sorption experiments. The sorbed amount of Ag NPs was much lower in the leaves of the Ler and Col-7 ecotypes treated with 10 μM ABA than that in the ABA-free control, mainly due to ABA-induced stomatal closure. However, sorption of Ag NPs by the leaves of the *ost1-2* and *scord7* mutants did not change with and without ABA. Microscopic images showed that internalized Ag NPs were located in the cell membrane, cytoplasm and plasmodesmata. Clearly stomata play an important role in the internalization of ENMs in plants, which has broader implications in foliar application of nanopesticides and minimizing ENMs contamination of food crops. Overall, the sustainable use of nanotechnology will depend on improved knowledge on and proper management of its benefits and potential risks.

This dissertation is dedicated to my parents, Taiming He and Qiongyao Zhang, my love, Dandan Peng, and my beloved daughter, Michelle Peng He. I love you all!

ACKNOWLEDGMENTS

First and foremost, I would like to express my sincere gratitude to my advisor Dr. Wei Zhang for his continuous guidance and support of my Ph.D. study, and for his enthusiasm, knowledge, commitment, patience, and encouragement. In the past four years, Dr. Zhang has been acting not only as a major advisor but also as a mentor for my life. This dissertation would not have been completed without his support and help, which is especially invaluable to me during this COVID-19 pandemic. I am also very grateful to the other members of my dissertation committee, Dr. Hui Li, Dr. Elliot Ryser, and Dr. Sheng Yang He, for their insightful comments and guidance for my doctoral study.

I would also like to thank my group members, colleagues, and friends at Michigan State University, Drs. Yuanbo Li, Yingjie Zhang, Cheng-Hua Liu, Sangho Jeon, Zeyou Chen, Feng Gao, Xun Qian, Shuai Zhang, Yike Shen, Qi Yuan, Ya-Hui Chuang, Anping Peng, Bingyu Wang, Xiaojie Hu, Fengling Liu, Shuang Liu, as well as Geoff Rhodes, Gayathri Gunathilaka, Yu Zhang, Hongyu Dang, Jinfeng Li, and many others, for their help, support, and friendship. I also want to acknowledge the help specifically from Drs. Dengjun Wang, Yaozhong Zhang, and Li Zhang.

Finally, I would like to thank my parents, Taiming He and Qiongyao Zhang, my parents-in-law, Shuyun Peng and Qizhen Ran, my brothers, Xin He and Jianghu Peng, for their unconditional support and unreserved love. My deepest gratitude is owed to my wife, Dandan Peng, for her love, support, and companionship for the past eight years. Special thanks to my beloved daughter, Michelle Peng He.

TABLE OF CONTENTS

LIST OF TABLES

LIST OF FIGURES

CHAPTER I

INTRODUCTION AND OBJECTIVES

Nanomaterials and Nanotechnology

Nanomaterials are materials with at least one dimension sized between approximately 1 to 100 nanometers (nm, = 10^{-9} m) [1], originating from either natural, incidental, or engineered sources. Naturally occurring nanomaterials may come from volcanic ash, ocean spray, forest fires, rock weathering, etc. Nanomaterials can also be generated incidentally as byproducts of mechanical or industrial processes (e.g., combustion, vehicle engine exhausts, and welding fumes). In contrast, engineered nanomaterials (ENMs) are deliberately designed and produced for their unusual, tunable properties or functions [2]. Despite the ubiquity of natural, incidental, and engineered nanomaterials, only in the past decades have their impacts on the environment been extensively studied [2]. This progress mainly resulted from multiple advances in analytic tools and techniques, for example, the development of scanning tunneling microscopy which has provided us with much better understanding of the distinct behaviors of ENMs.

Nanotechnology manipulates matter at the nanoscale to explore distinct properties and phenomena. Since the launch of the National Nanotechnology Initiative (NNI) in 2000, three main developmental stages of nanotechnology have been envisioned, and we are now at the beginning stage translating nanoscale science to marketable technology and products (*Nano 3*) [3]. Worldwide the market value of nanotechnology-incorporated products was $1 trillion in 2013, and was projected to be over $3 trillion by 2020 [4] and about one order of magnitude more by 2030 [3]. In 2005 the Woodrow Wilson International Center for Scholars and the Project on Emerging Nanotechnologies initiated the Nanotechnology Consumer Products Inventory, which was revised in 2013, documenting 1814 nano-enabled consumer products from 622 companies in 32 countries [5]. A very recent search of the scientific literature shows that since 2000 over 8000 articles on the topic of ENMs were published with an exponential increase (Figure 1.1), and is expected to grow

substantially in next ten years and beyond. Nanotechnology will likely continue to grow exponentially by vertical science-to-technology transition and horizontal expansion to other fields (e.g., environmental field).

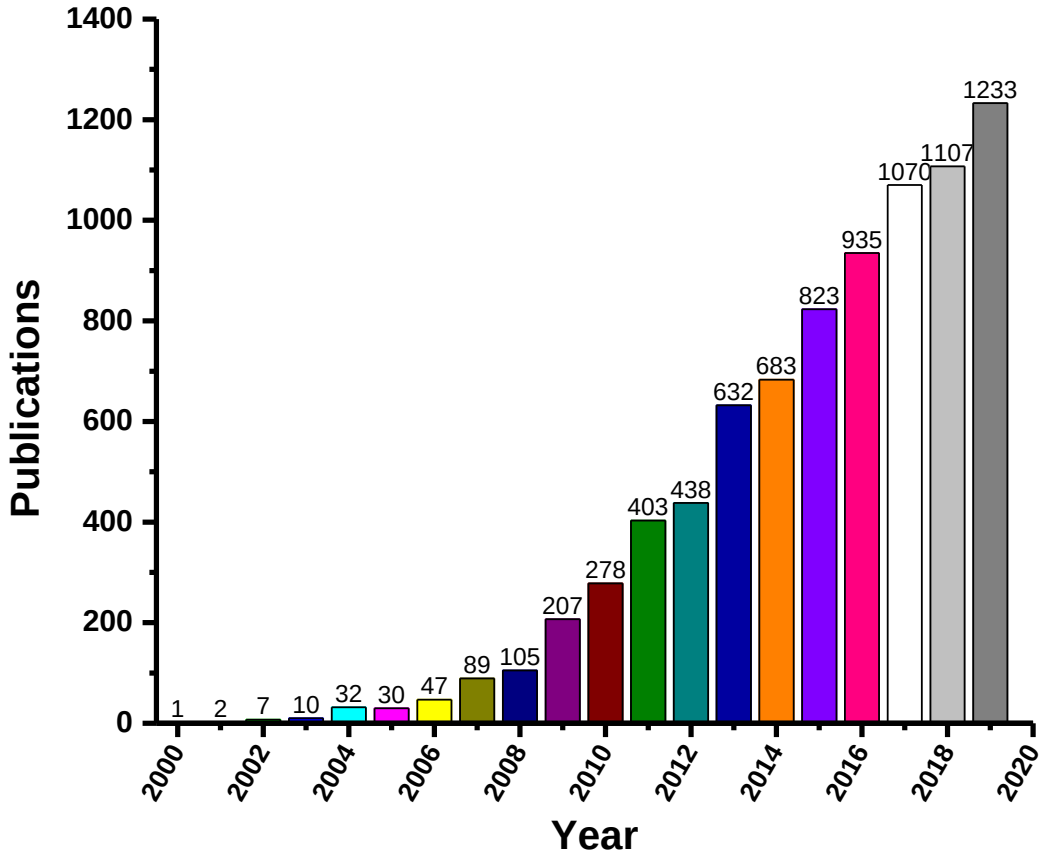

Figure 1.1. Publications trend in engineered nanomaterials research. Web of Science results for the number of annual publications from 2000 to 2019 with search keyword “engineered nanomaterials”.

Environmental Application of Nanotechnology

Nanotechnology for environmental application is one of the most promising approaches to address environmental problems in air, water, and soil. Among them, water treatment using ENMs is a main focal point. The world is facing water scarcity globally, due to shortages and pollution of fresh water resources [6, 7]. More alarmingly, an increasing number of emerging contaminants (e.g., pharmaceuticals) are found in rivers, lakes, groundwater aquifers, and oceans [8-16], which raises substantial concerns on their impact to ecosystem and human health. Pharmaceuticals are not readily removed by conventional wastewater treatment plants (WWTPs) [16-19]. As a result, pharmaceuticals are increasingly being detected at ng L^{-1}–μg L^{-1} levels in aquatic environments [15, 20, 21], which may pose acute and chronic toxicities to aquatic organisms [22-24]. In addition, pharmaceuticals ubiquitously found in reclaimed wastewater and sewage sludge could be released into agricultural soils via crop irrigation and land application of sewage sludge, followed by assimilation and transformation in food crops [25-28]. Thus, the human population may be potentially exposed to pharmaceutical residues or their metabolites via consumption of contaminated food crops. Paltiel et al [29] showed that volunteers consuming reclaimed wastewater-irrigated produce had higher urinary concentrations of carbamazepine and its metabolites compared to those consuming fresh water-irrigated produce. Therefore, rising public health and environmental concerns necessitate the development of effective and robust methods to remove pharmaceuticals from water.

Recent advances in nanotechnology can be harnessed to develop next-generation water treatment techniques [22]. Several ENMs (e.g., TiO_2, ZnO, Bi_xO_y, g-C_3N_4, GO) may be used to remove pharmaceuticals from wastewater through adsorption, photocatalysis, or membrane filtration. In particular, photocatalysis by ENMs has been intensively studied for treating water

and wastewater due to its low cost and high efficiency [30-36]. In fact there have been over 8000 publications on photocatalytic water treatment since 2000 [35]. It has shown that photocatalysis assisted with ENMs exhibits remarkable performance for advanced, robust, and multifunctional water treatment. However, many obstacles still need to be addressed in order to optimize photocatalysis, including effective separation of electron-hole pairs (e^-/h^+) and subsequent generation of reactive radicals, and recovery and separation of ENMs catalysts.

Environmental Implication of Nanotechnology

Like many other emerging technologies, environmental impacts of nanotechnology must be considered. For example, nanotechnology may pose risks to environment and human health [37-39], especially with the rapid production and widespread application of ENMs. Therefore, it is crucial to assess the downstream impact of ENMs release on ecosystems and human health, thereby developing mitigation strategies.

ENMs are increasingly incorporated into many industrial and consumer products, such as textile, paint, clothing, sunscreen, cosmetics, antimicrobial agents, medicine, food additives, and pesticides [5, 40, 41]. The production, use, and disposal of ENMs will lead to their inevitable dissemination into the environment. Environmental discharge of ENMs can occur through multiple pathways, including direct use of ENMs or ENM-containing products, sewage treatment, and landfills. Gottschalk and Nowack [42] concluded that sewage sludge, wastewater, and waste incineration of ENMs-containing products are three major flows of EMMs from a life-cycle perspective. Detailed evidence showed that both colloidal and ionic silver were steadily leached from certain socks during water washing [43]. Under natural weathering conditions, researchers revealed that TiO_2 nanoparticles (NPs) were detached from facade paints and then carried by runoff into natural receiving water [44]. In fact, Ag NPs was detected at 100 ng L^{-1} in the effluent of a

wastewater treatment plant in the US [45]. The predicted environmental concentrations of Ag NPs in surface water, wastewater effluents, and sewage sludge were 0.09–80 ng L^{-1}, 0.016–0.127 μg L^{-1}, and 1.29–6.24 mg kg^{-1}, respectively [46, 47]. The annual increase of ENMs ranged from 1 ng kg^{-1} for fullerenes to 89 μg kg^{-1} for TiO_2 NPs for sludge-treated soils in Europe and the US [46].

Crop plants are prone to ENMs exposure as a result of intentional application of nanopesticides and nanofertilizers, irrigation with reclaimed water, sewage sludge application, and atmospheric deposition [48, 49]. Extensive studies proved that ENMs in soil and water could be potentially taken up by crop plants and subsequently enter into the human food chain [50-57] For instance, agglomeration of Cu NPs was observed in cells of mung bean (*Phaseolus radiatus*) and wheat (*Triticum aestivum*) [58]. Aggregates of CeO_2 NPs can be taken up by corn plants via the apoplastic pathway and translocated further to vascular tissues [59]. Generally, ENMs can enter plant roots via the apoplastic or symplastic pathways [60-66]. It was thought that ENMs could be restricted by a size exclusion limit (40–50 nm) of the plant roots and stopped by the *Casparian* strip barrier following the apoplastic pathway [67]. However, the former restriction may be overcome by endocytosis [62, 68, 69], physical wound and disease damage to roots, and the emergence of new secondary roots [64, 66].

It is believed that reducing the bioavailability of ENMs in soil is critical to minimizing their migration from soil to plant. Soil components (e.g., humic acid) can affect ENMs properties and subsequently their assimilation by plants [70]. Recently, soil amended with biochar was shown to effectively limit plant uptake of ENMs [71-74], due to strong sorption capacity of biochar to many organic and inorganic contaminants (including ENMs). However, the applicability of biochar amendment to realistic exposure level of ENMs in soil has not been tested. This knowledge gap

limits our ability to assess the risks of ENMs via human dietary exposure and the feasibility of biochar amendment as a mitigation strategy.

Additionally, it should be noted that the development of plant protection products (e.g., nanopesticides) has recently drawn immense attention. For example, over one hundred pesticides containing Ag NPs have been registered in the last decade [75-77]. Ag and TiO_2 NPs are being used in fungicides as active ingredients [78, 79], and silica NPs as carriers [80]. Application of nano-enabled agrochemicals can lead to direct contact between ENMs and the plant surface. Earlier studies have shown that ENMs likely enter plants by diffusion through the cuticle wax barrier and/or through openings in cuticle and stomata [68, 81, 82]. For example, Larue et al. [49] provided the first evidence that Ag NPs were entrapped by the cuticle and penetrated into the leaves through stomata. Although several studies addressed the potential of ENMs entry through stomatal openings, no studies have specifically investigated the role and contribution of stomata in the sorption and internalization of ENMs by plant leaves.

Research Objectives

Objective 1: Evaluate photocatalytic degradation of cephalexin by ZnO nanowires. Photocatalysis assisted with novel ENMs (e.g., ZnO nanowires) may be promising for removing pharmaceuticals from water. Here we hypothesize that ZnO nanowires can effectively degrade antibiotics in water under sunlight with the degradation efficiency affected by water chemistries, such as solution pH, inorganic anions, and natural organic matter. To test this hypothesis, we systematically investigated the photocatalytic degradation of the antibiotic cephalexin using ZnO nanowires under simulated sunlight and aimed to learn more about the efficiency, influencing factors, and mechanism of photocatalytic degradation of cephalexin.

Objective 2: Investigate the uptake of silver nanoparticles and ions by radish in soil with biochar amendment. Biochars often have strong sorption capacity to many organic and inorganic contaminants (including ENMs), and thus could potentially decrease crop uptake of ENMs from soil. Here we hypothesize that biochar can reduce the uptake of silver nanoparticles (Ag NPs) and ions by a vegetable crop (radish). However, biochar effectiveness may be different when plants are exposed to Ag NPs at environmentally relevant levels, compared to the previous literature using unrealistically high concentrations. Hence, the objective of this study was to evaluate the feasibility of soil biochar amendments to decrease radish uptake of Ag NPs and ions at environmentally relevant concentrations.

Objective 3: Explore the role of stomata in foliar sorption of silver nanoparticles by *Arabidopsis thaliana*. Foliar uptake is regarded as a significant pathway for the internalization of ENMs into plants, in addition to root uptake, because of the possible role of stomata openings. Here we hypothesize that stomata openings contribute substantially to the internalization of ENMs into leaves. The objective of this study was to assess the sorption of Ag NPs by leaves using abscisic acid (ABA)-responsive ecotypes and ABA-insensitive mutants of *Arabidopsis thaliana*.

The three objectives are addressed in the following three chapters in this dissertation. Objective 1 is addressed in Chapter II, Objective 2 in Chapter III, and Objective 3 in Chapter IV. The dissertation concludes with Chapter V that summarizes the findings and suggests future research directions.

CHAPTER II

PHOTOCATALYTIC DEGRADATION OF CEPHALEXIN BY ZnO NANOWIRES UNDER SIMULATED SUNLIGHT

Abstract

Increasing concentrations of anthropogenic antibiotics and their metabolites in aqueous environments have caused growing concerns over the proliferation of antibiotic resistance and potential adverse impacts to agro-environmental quality and human health. Photocatalysis using novel engineered nanomaterials such as ZnO nanowires may be promising for removing antibiotics from water. However, much remains to be learned about the efficiency and mechanism for photocatalytic degradation of antibiotics by ZnO nanowires. This study systematically investigated photodegradation of cephalexin using ZnO nanowires under simulated sunlight. Degradation efficiency of cephalexin was substantially increased in the presence of ZnO nanowires especially at pH of 7.2–9.2. Photodegradation followed the first-order kinetics with degradation rate constants (k) ranging between 1.19×10^{-1}–2.52×10^{-1} min^{-1} at 20–80 mg L^{-1} ZnO nanowires. Radical trapping experiments demonstrated that hydroxyl radicals (•OH) and superoxide radicals ($•O_2^-$) predominantly contributed to the photodegradation of cephalexin. With the addition of HCO_3^- (1–5 mM) or Suwannee River natural organic matter (SRNOM, 2–10 mg L^{-1}), the k values were substantially decreased by a factor of 1.8–70 to 1.69×10^{-3}–6.67×10^{-2} min^{-1}, probably due to the screening effect of HCO_3^- or SRNOM sorbed on ZnO nanowires and scavenging of free radicals by free HCO_3^- or SRNOM in solution. Based on mass spectrometry and molecular computation, the pathways for photodegradation of cephalexin included hydroxylation, demethylation, decarboxylation, and dealkylation. Overall, these novel ZnO nanowires have the potential to be used for removing antibiotics from contaminated water.

Introduction

Antibiotics are widely used to treat or prevent bacterial infections. Cephalexin, in particular, is a semisynthetic cephalosporin drug that has been extensively produced and used in human healthcare and animal agriculture. Approximate 10%–90% of antibiotics administered to animals and humans are excreted as either parent compounds or biotransformed metabolites [8, 83], and are subsequently discharged to the environment. As a result, a plethora of antibiotics have been detected in wastewater, surface water, and seawater at ng L^{-1} to μg L^{-1} levels [15, 21, 23]. The elevated environmental concentrations of antibiotics have raised public concern over their potential adverse impact to agro-environmental quality, human health, livestock, and ecosystems [24, 84, 85]. For example, when assessing risk quotients (RQ) of antibiotics at environmental concentrations, antibiotics in the Hai River in China had high ecotoxicological risk to algae (ΣRQ = 1.832), invertebrates (ΣRQ = 3.568), fish (ΣRQ = 0.094), and plants (ΣRQ = 5.008) [23]. There is also a general consensus that antibiotics in the environment facilitate the development and proliferation of antibiotic resistant bacteria and antibiotic resistance genes [20, 86], even at concentrations much lower than minimum inhibitory concentrations [87]. In addition, treated wastewaters and biosolids containing antibiotics are widely used in agricultural production, resulting in accumulation and transformation of antibiotics in crop plants [25-27, 88]. Thus, sensitive and susceptible human populations may be disproportionally impacted by exposure to antibiotics and their metabolites through dietary intake of contaminated food crops [29, 88]. Therefore, it is becoming increasingly important to develop effective methods for removing antibiotics from contaminated waters.

Removal of antibiotics by wastewater treatment plants (WWTPs) is highly variable, depending on wastewater characteristics, treatment processes, operational conditions of WWTPs, and properties of the individual antibiotics [17, 18]. For example, cephalexin concentrations can be up

to 64 μg L^{-1} in WWTP influents [16] and 5 μg L^{-1} in WWTP effluents [89]. The removal efficiency of cephalexin in conventional WWTPs varies between 9%–96% [16, 19]. Advanced tertiary treatment methods may be used for removing antibiotics at WWTPs, such as activated carbon adsorption, ozonation, nanofiltration, and reverse osmosis [17]. Enhanced removal, albeit not for all compounds nor for all WWTPs, has been observed with the advanced treatment methods [17]. In comparison, photocatalysis has recently received tremendous research attention for removing antibiotics from water due to its low cost and high efficiency [30-33].

One of the most critical aspects in photocatalysis is the generation of electron–hole pairs (e^-/h^+) when catalysts are irradiated with photons at an energy level greater or at least equal to their band gap energy. Notably, zinc oxide (ZnO) nanomaterials can be excited by a broad solar spectrum [90]. They also have excellent quantum efficiency [91] and environmental friendliness [92]. Thus, ZnO nanomaterials have been studied for photocatalytic degradation of organic dyes (e.g., methylene blue and rhodamine 6G), phenolic compounds (e.g., chlorophenol and fluorophenol), and pharmaceuticals (e.g., ampicillin, caffeine, cloxacillin, resazurin, and tetracycline) [33, 91, 93-98]. Photodegradation efficiency of organic contaminants by ZnO nanomaterials depends on a number of factors including the dosage, structure, and morphology of ZnO nanomaterials, initial contaminant concentration, light wavelength, irradiation intensity, solution pH, temperature, inorganic species, and natural organic matter (NOM) [91, 98]. Specifically, ZnO nanomaterials have various structures and morphologies such as nanospheres, nanobelts, nanosheets, nanorods, nanowires, nanodumbbells, nanoflowers, and nanotetrapods [91, 97], resulting in various photocatalytic efficiencies due to the difference in specific surface area, surface-to-volume ratio, and external mass transfer rate [91, 93, 95, 99]. In particular, ZnO nanowires may have enhanced catalytic properties due to their high surface-to-volume ratio, and strong defect emission [95, 97, 99].

ZnO nanowires may be promising as large-scale, cost-effective, and highly efficient photocatalysts and can be more easily separated and recovered especially when embedded on substrates [95, 100-102]. Nonetheless, only a limited number of studies have investigated the photodegradation of organic contaminants by ZnO nanowires [95, 102] and to our best knowledge, no study has examined the photodegradation of cephalexin by ZnO nanowires. Therefore, more work is needed to develop better ZnO nanowire-based treatment systems for degradation of cephalexin and other antibiotics from contaminated water.

As mentioned above water chemistry such as solution pH, anions (e.g., HCO_3^-, Cl^-, and NO_3^-), and NOM may substantially influence the photodegradation of cephalexin. Solution pH may inhibit or enhance photodegradation by influencing dissociation and charge speciation of ionizable contaminants and contaminant sorption onto catalyst surfaces [91, 98, 103]. Similarly, NOM and anions (e.g., HCO_3^-) could compete for sorption sites on photocatalyst surfaces and/or scavenge reactive species, thus decreasing photodegradation efficiency [104-108]. However, it was also reported that the presence of HCO_3^- actually enhanced the photodegradation of sulfamethoxazole [32, 36]. Hence, the effect of water chemistry on the photodegradation of cephalexin warrants further investigation.

Therefore, this study aimed to investigate the photodegradation of cephalexin by ZnO nanowires under simulated sunlight at a range of water chemistries. The tested ZnO nanowires were synthesized via a hydrothermal method and characterized using transmission electron microscopy (TEM), scanning electron microscopy (SEM) with energy-dispersive X-ray spectroscopy (EDS), X-ray diffraction (XRD), and a Zetasizer. Photodegradation efficiency and kinetics, and the effects of water chemistries (i.e., solution pH, HCO_3^-, and NOM) were systematically examined, and underlying photodegradation mechanisms (including pathways)

were identified using both molecular computation and mass spectrometry. This study could provide useful information for improved understanding on the photodegradation of cephalexin by ZnO nanowires and for future development of novel treatment systems that incorporate ZnO nanowires.

Materials and Methods

Chemicals

Cephalexin (99.7%, analytical grade), potassium dichromate (99.5%), zinc acetate dihydrate (99.9%), *tert*-butanol (99.5%), p-benzoquinone (98%), and methanol (HPLC grade) were purchased from Sigma-Aldrich (St. Louis, MO). Sodium bicarbonate, sodium chloride, sodium hydroxide and ethylenediaminetetraacetic acid disodium salt (EDTA-2Na) were of analytical grade and obtained from J.T. Baker (Philipsburg, NJ). Acetonitrile (HPLC grade) and hydrochloric acid (37%) were purchased from EMD Chemicals (Gibbstown, NJ). Ethanol (100%) was purchased from Fisher Scientific Inc. (Hampton, NH). Chemical structure and species distribution of cephalexin are shown in Supplementary Figure A1 of Appendix A. Suwannee River natural organic matter (SRNOM, 2R101N) was acquired from the International Humic Substances Society and contains 50.70% C, 3.97% H, 41.41% O, 1.27% N and 1.78% P. Reagents were used without further purification. All solutions were prepared in Milli-Q water (18 MΩ cm at 25 °C, Millipore, United States Filter Corporation, CA) and then adjusted to the desired pH using 0.1 M HCl or 0.1 M NaOH. To prepare the stock solution of SRNOM, 0.2 g of SRNOM was first dissolved in 100 mL of Milli-Q water and stirred overnight. The SRNOM solution was adjusted to pH 7.2 before filtering through a 0.45-μm cellulose acetate membrane to remove any insoluble materials. Total organic carbon (mg C L^{-1}) of the SRNOM stock solution was quantified using an Aurora 1030 TOC analyzer (OI Analytical, Xylem, UK).

Synthesis and Characterization of ZnO Nanowires

ZnO nanowires were synthesized using a modified hydrothermal method as previously described [109, 110]. Briefly, a ZnO seed solution was prepared by adding 0.1 M $Zn(CH_3COO)_2 \bullet 2H_2O$ in ethanol and stirring at 58 °C for 2 h. The ZnO seed solution was then mixed with 0.5 M NaOH solution at a 1:2 volume ratio and transferred to a Teflon-lined autoclave, followed by heating at 150 °C for 24 h. Afterwards, the mixture was centrifuged at 10,000 rpm for 10 min at room temperature. The pellets were thoroughly rinsed with deionized (DI) water and dried in an oven at 60 °C for 12 h.

The prepared ZnO nanowires were imaged by TEM (JEOL 2200FS, Tokyo, Japan) and SEM (JEOL 7500F, Tokyo, Japan) equipped with an Oxford EDS at an accelerating voltage of 5.0 kV. The XRD pattern of the ZnO nanowires was obtained on a Bruker D8 DaVinci diffractometer (Bruker Corporation, Billerica, MA) equipped with Cu X-ray radiation operating at 40 kV and 40 mA. The ZnO nanowires were placed in a PVMA sample holder and rotated at 5º/min. Peak intensities were obtained by counting with the Lynxeye detector every 0.02º/0.5 s. A Zetasizer (Nano ZS, Malvern, UK) was used to measure zeta potential and hydrodynamic diameter of the ZnO nanowires under all investigated experimental conditions (pH = 5.0−9.2, $[HCO_3^-]$ = 1−5 mM, and [SRNOM] = 2−10 mg L^{-1}). Measurements were repeated 3 times for at least two separate samples at 25 °C. To measure ZnO nanowire dissolution, aliquots of ZnO nanowire suspensions were filtered using Amicon Ultra 3k ultrafiltration units (Millipore, Burlington, MA). The filtrates were measured for Zn^{2+} ion concentration using atomic absorption spectroscopy (AAnalyst 400, PerkinElmer, Waltham, MA).

Photodegradation Experiments

A series of photodegradation experiments were carried out in a SUNTEST XLS+ Solar simulator (Atlas Material Testing Technology LLC, Mount Prospect, IL) equipped with an air-cooled 1700 W xenon lamp. A daylight filter with a cutoff wavelength < 290 nm was used to simulate sunlight, and the temperature was maintained at 25 ºC using a SunCool unit. The irradiation intensity was set to 700 ± 5 W m^{-2}, similar to that used in other studies [111, 112]. All photodegradation experiments were conducted in triplicate.

To assess the effect of catalyst dose on photodegradation efficiency, ZnO nanowires were added to 50 mL of a 100 µg L^{-1} cephalexin solution at 20, 40, or 80 mg L^{-1}. Background solution ionic strength was 5 mM NaCl and the initial solution pH was 7.2. The initial cephalexin concentration of 100 µg L^{-1} was slightly higher than average environmental cephalexin concentrations (ng L^{-1} to µg L^{-1}), and somewhat above the reported maximum concentration of 64 µg L^{-1} in influent at a WWTP [16, 19, 89]. However, the level was far lower than the cephalexin concentrations (10–50 mg L^{-1}) typically used in previous studies [30, 113-115]. With increasing contaminant concentrations, the photodegradation efficiency would be expected to increase until reaching the optimal contaminant concentration, and then decrease at higher contaminant concentrations [91, 98]. Therefore, we selected the low initial concentration to better assess the photodegradation efficiency at environmentally-relevant concentrations. Prior to exposure to simulated sunlight, the suspension was placed in the dark for 30 min to reach the adsorption-desorption equilibrium. After initiating the photodegradation experiments, aliquots (0.5 mL) of the suspensions were withdrawn at various time intervals (5, 10, 25, or 30 min) and then immediately quenched with methanol. The samples were centrifuged at 13,000 rpm for 15 min, and the supernatant was collected and stored at 4 °C in amber glass vials before analysis. At each sampling

point the suspension was shaken vigorously by hand to minimize sedimentation during the photodegradation experiments. No visible sedimentation was observed, likely due to the stabilization of ZnO nanowire aggregates after initial aggregation and the short sampling intervals (5–30 min). To evaluate the performance of ZnO nanowires for cephalexin degradation in environmentally-relevant conditions, a wide range of water chemistries was examined. Various solution pH (5.0–9.2), and HCO_3^- (1–5 mM) or SRNOM (2–10 mg C L^{-1}) concentrations were adjusted in the suspensions containing 20 mg L^{-1} ZnO nanowires and 100 μg L^{-1} cephalexin. Parallel control experiments were also conducted under identical conditions without ZnO nanowires or with Zn^{2+} ions (~10 mg L^{-1}, assuming the maximum dissolution) in place of ZnO nanowires.

Additional experiments using recycled ZnO nanowires were performed to evaluate the reusability and stability of ZnO nanowires using experimental conditions and procedures identical to those of the kinetic experiments. At the end of each cycle (90 min irradiation time per cycle), the cephalexin concentration in the solution was measured and then replenished to 100 μg L^{-1}, followed by the next light irradiation. Degradation efficiency was calculated by dividing the difference between the initial and final concentration with the initial concentration in each cycle.

The photodegradation kinetics of cephalexin were fitted using a first-order kinetic model:

$$\ln (C_t/C_0) = -kt$$

where C_0 and C_t represent the cephalexin concentrations at time 0 (i.e., after reaching the adsorption-desorption equilibrium in dark) and the sampling time *t*, respectively, and *k* is the first-order degradation rate constant (min^{-1}). One-way ANOVA analysis was performed to test the statistical significance in mean values of *k* using the least significant difference (LSD) test with SPSS 22.0 software for Windows (IBM Corp., Armonk, NY) at $p < 0.05$.

Trapping Experiments

To identify reactive radicals responsible for cephalexin degradation, trapping experiments were performed under experimental conditions identical to those in the photodegradation experiments, except that specific scavengers were added to the suspensions before exposure to simulated sunlight. Ethylenediaminetetraacetic acid disodium (EDTA-2Na, 0.1 mM) was used as a scavenger for the photo-induced holes (h^+) [32], *tert*-butanol (10 mM) for hydroxyl radicals (•OH) [116], potassium dichromate ($K_2Cr_2O_7$, 50 μM) for the photo-induced electrons (e^-) [117], and p-benzoquinone (1 mM) for superoxide radicals ($•O_2^-$) [118].

Analytical Methods

Cephalexin concentrations in the samples were determined using a Shimadzu prominence high-performance liquid chromatography system (Shimadzu, Columbia, MD) coupled with an AB Sciex 4500 QTrap triple quadrupole mass spectrometer (SCIEX, Foster City, CA) (LC-QTrap-MS/MS). An Agilent Eclipse Plus C18 column (50 mm × 2.1 mm, 5 μm, Agilent, Santa Clara, CA) was used for chromatographic separation prior to mass spectrometry analysis. The binary mobile phase consisted of water (phase A) and acetonitrile (phase B) with 0.1% (v/v) formic acid. The degradation products were identified using LC-QTrap-MS/MS under positive ionization mode, in combination with an enhanced mass scan as a survey scan, information dependent acquisition criteria, and an enhanced product ion scan to obtain the MS/MS fragment patterns. The full approach for identifying cephalexin oxidation products can be found in Chuang et al. [119]. Details on analytical method and product identification procedures are given in Supplementary Text A1 of Appendix A.

Theoretical Calculation

To help identify the reactive sites for free radical attack and possible photodegradation pathways, molecular orbital calculation of cephalexin with the optimal conformation (Supplemental Figure A2) was performed at B3LYP/6−311 + G* level in Gaussian 09 program [34]. The frontier electron densities (FED) of the highest occupied molecular orbital (HOMO) and the lowest unoccupied molecular orbital (LUMO) of each atom in cephalexin were calculated to theoretically predict locations of reactive sites for free radical attack. The positions with higher values of $2FED_{HOMO}^2$ are more susceptible to electron extraction, whereas those with higher values of $FED_{HOMO}^2 + FED_{LUMO}^2$ are more likely to be attacked by free radicals [34].

Results and Discussion

Characterization of ZnO Nanowires

Representative SEM, TEM, and XRD pattern of ZnO nanowires are shown in Figure 2.1. The average diameter of ZnO nanowires was 39 ± 10 nm and their length varied between 56–1,454 nm with a mean value of 328 nm measured from randomly selected ~100 ZnO nanowires using ImageJ 1.52a software (Figure 2.1a and b). The sharp diffraction peaks in Figure 2.1c confirmed good crystallinity of the ZnO nanowires, and the intense peaks that originated from (100), (002), (101), (102), (110), (103), (200), (112), and (201) can be well indexed to the hexagonal wurtzite ZnO structure in accordance with the standard JCPDS card (no. 36-145). The strong intensity of (002) peak indicated the preferable growth of ZnO nanowires along the c-axis orientation. Additionally, no diffraction patterns of any other impurities were detected, and no other elements except Zn and O were found on the EDS spectra (Supplemental Figure A3), confirming that the synthesized ZnO nanowires were primarily pure ZnO hexagon that is favored as a photocatalyst [120].

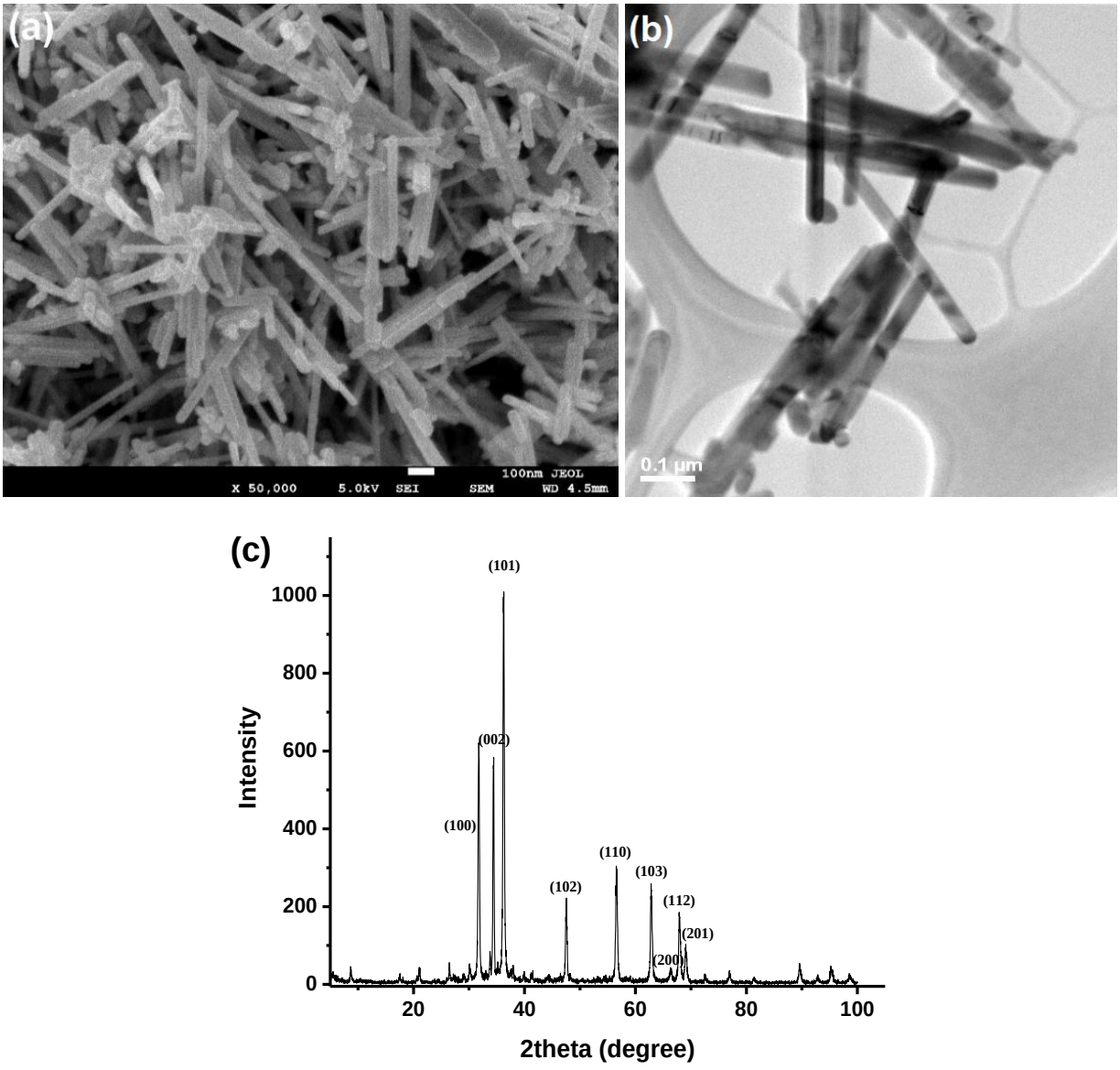

Figure 2.1. Representative (a) scanning electron microscopy, (b) transmission electron microscopy images, and (c) X-ray diffraction pattern of ZnO nanowires.

Table 2.1 shows the zeta potentials and hydrodynamic diameters of ZnO nanowires in suspensions of varying water chemistries. As solution pH increased, the zeta potentials became more negative. The surface charge of ZnO nanowires reversed from positive to negative at pH 6.8 which is defined as the point of zero charge (pH_{pzc}) for ZnO nanowires (Supplemental Figure A4). Accordingly, prior to charge reversal, the hydrodynamic diameters of ZnO nanowires increased with increasing pH, due to decreasing electrostatic repulsion between positively charged ZnO nanowires. After the solution pH increased beyond pH_{pzc} of 6.8, the hydrodynamic diameters of ZnO nanowires decreased, resulting from increasing electrostatic repulsion between negatively charged ZnO nanowires (Table 2.1). The largest hydrodynamic diameter (5192 ± 481 nm) was observed near pH_{pzc}, indicating the absence of any repulsive electrostatic interaction [121]. The addition of HCO_3^- (1–5 mM) had a minor influence on the zeta potentials and hydrodynamic diameters of ZnO nanowires. However, the presence of SRNOM (2–10 mg L^{-1}) decreased the surface charge of ZnO nanowires sharply (Table 2.1), leading to a decrease in hydrodynamic diameter compared to the SRNOM-free suspensions of ZnO nanowires. This can be attributed to both increased electrostatic and steric repulsion by the adsorbed SRNOM on the surface of ZnO nanowires. Our tests showed that the SRNOM solution at 2–10 mg L^{-1} did not produce size measurements met the analysis quality criteria of the Zetasizer. Therefore, the measured size should have been primarily contributed by ZnO nanowires, and not by SRNOM. We did not attempt to distinguish the contribution of the adsorbed SRNOM layer to the aggregate size of ZnO nanowires, which was beyond the scope of this study.

Table 2.1. Zeta potentials and hydrodynamic diameters of ZnO nanowires under various experimental conditions.

ZnO nanowires (mg L^{-1})	pH	HCO_3^- (mM)	SRNOM (mg L^{-1})	Zeta Potentials (mV)	Hydrodynamic Diameters (nm)
20	5.0	–	–	11.3 ± 2.8	600 ± 84
20	6.2	–	–	5.52 ± 2.13	922 ± 120
20	7.2	–	–	−4.18 ± 1.19	5192 ± 481
20	8.3	–	–	−8.20 ± 0.66	3111 ± 400
20	9.2	–	–	−18.0 ± 2.11	2372 ± 89
20	7.2	1	–	−3.73 ± 1.14	6668 ± 257
20	7.2	2	–	−3.65 ± 0.46	7639 ± 656
20	7.2	5	–	−3.65 ± 0.78	7738 ± 379
20	7.2	–	2	−38.9 ± 1.8	1505 ± 218
20	7.2	–	5	−36.2 ± 2.4	1404 ± 270
20	7.2	–	10	−35.7 ± 3.2	1608 ± 168
–	7.2	–	10	−32.3 ± 3.6	1073 ± 180[a]

[a] This measurement did not meet the quality criteria using dynamic light scattering.

Photodegradation Efficiency and Reusability

Figure 2.2 shows the photocatalytic degradation kinetics of cephalexin in the absence and presence of ZnO nanowires under simulated sunlight at pH 7.2. A negligible amount of cephalexin was degraded by hydrolysis and photolysis, as well as by the presence of Zn^{2+} ions (10 mg L^{-1}) over 180 min under simulated sunlight. However, the addition of ZnO nanowires (i.e., 20, 40, or 80 mg L^{-1}) significantly enhanced the photodegradation of cephalexin ($p < 0.05$, Table 2.2), with over 96% of the cephalexin degraded within 25 min and complete decay within 45 min in the presence of 20 mg L^{-1} ZnO nanowires. Liu et al. [30] investigated the photocatalytic activity of CdSe quantum dots (500 mg L^{-1}) on cephalexin (15 mg L^{-1}) under UV irradiation, and only observed a degradation efficiency of 70.34% after 60 min. However, comparing the photodegradation efficiency of different catalysts is often very challenging due to differences in experimental conditions such as catalyst-to-contaminant ratios ranging between 30–500 in previous studies (Supplemental Table A1) [114, 122-126]. Additionally, turnover number and turnover frequency are difficult to estimate because determining the number of surface-active sites is a challenge [127]. Nonetheless, this study revealed that ZnO nanowires could effectively degrade cephalexin at trace-level concentrations (< 100 µg L^{-1}) that are about two orders of magnitude lower than commonly tested cephalexin concentrations (10–50 mg L^{-1}) in previous studies [30, 113-115]. Thus, ZnO nanowires could be well suited to degrade cephalexin from environmental water.

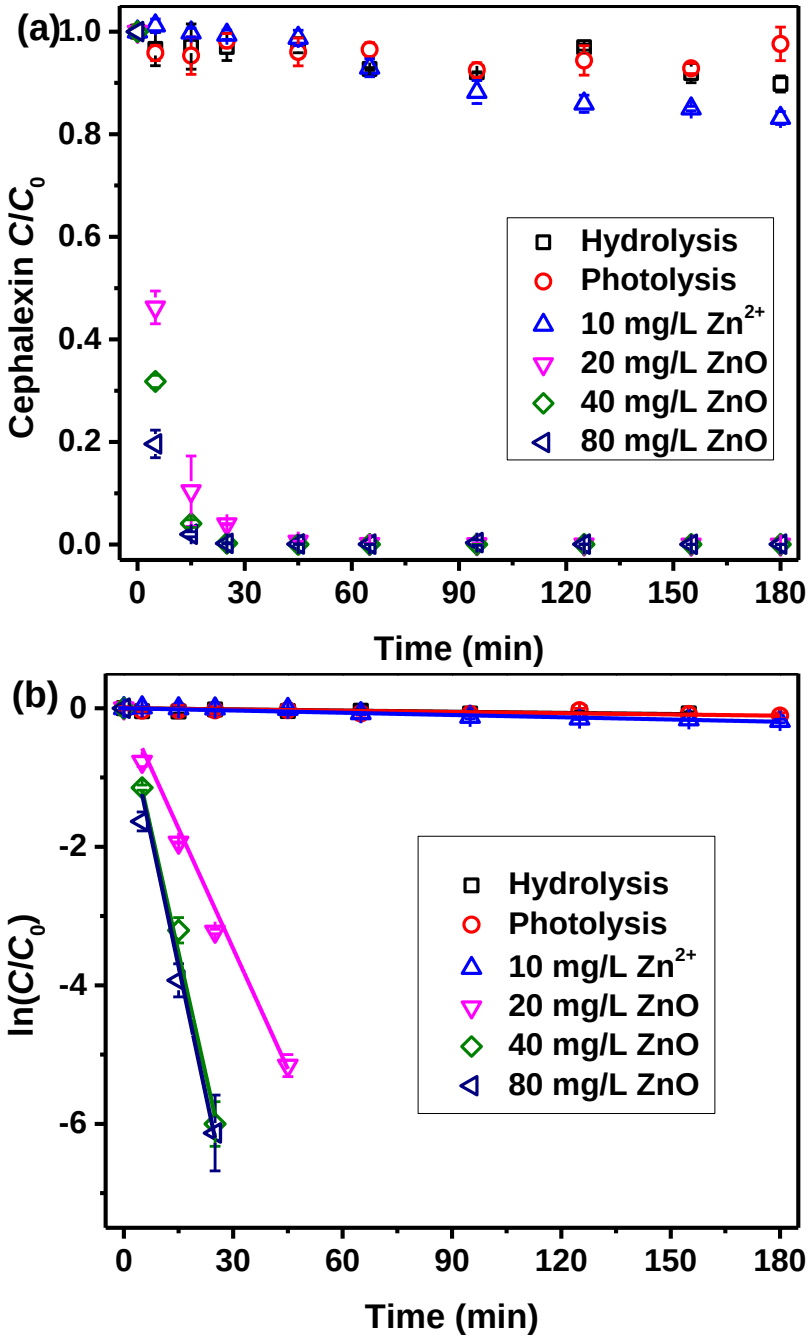

Figure 2.2. Observed (a) and fitted (b) photodegradation kinetics of cephalexin by ZnO nanowires (20, 40, and 80 mg L^{-1}) at pH 7.2 under simulated sunlight. Error bars represent the standard deviations (n = 3). Solid lines were fitted to initial parts of kinetics that followed the first-order degradation.

Cephalexin degradation followed the first-order kinetic model (Figure 2.2b) and the fitted *k* values are summarized in Table 2.2. The *k* values for cephalexin degradation remarkably increased from 6.00×10^{-4} min^{-1} for hydrolysis and 4.00×10^{-4} min^{-1} for photolysis to 1.19×10^{-1}–2.52×10^{-1} min^{-1} in the presence of ZnO nanowire (20, 40, or 80 mg L^{-1}). This observation is congruent with other studies [32, 33]. For example, the photodegradation rate of sulfamethoxazole was 2.04×10^{-4} min^{-1} by photolysis and increased to 0.023 min^{-1} by photocatalysis using g-C_3N_4 [32]. Additionally, in comparison the *k* values for cloxacillin (0.029 min^{-1}), amoxicillin (0.018 min^{-1}), and ampicillin (0.015 min^{-1}) using a UV/ZnO system [33] were 10 times lower than the observed *k* values in this study. Thus, our ZnO nanowires had a high photodegradation efficiency.

The reusability test results are shown in Supplemental Figure A5. The ZnO nanowires were capable of completely degrading cephalexin (100 μg L^{-1}) within 90 min in the first two use cycles, with > 94% degradation efficiency achieved in the fifth cycle. The slight decrease in efficiency was likely due to the dissolution of ZnO nanowires, as evidenced by the detected Zn^{2+} concentration of 2.79 mg L^{-1} after 5 cycles (Table 2.3). Interestingly, there were no visible morphological changes in the ZnO nanowires after 180 min irradiation as shown by the TEM images (Supplementary Figure A6). Therefore, these results suggest that the ZnO nanowires possess satisfactory stability for cephalexin degradation over at least 5 cycles under simulated sunlight.

Table 2.2. Fitted parameters for degradation kinetics of cephalexin in all experiments.

Experimental Sets	Degradation rate constant (k) (min^{-1})	R^2
Hydrolysis*	6.00 (0.00) × 10^{-4} d	0.83
Photolysis**	4.00 (1.73) × 10^{-4} d	0.83
10 mg L^{-1} Zn^{2+}	1.07 (0.05) × 10^{-3} d	0.98
20 mg L^{-1} ZnO nanowires	1.19 (0.02) × 10^{-1} a	0.99
40 mg L^{-1} ZnO nanowires	2.33 (0.12) × 10^{-1} b	0.99
80 mg L^{-1} ZnO nanowires	2.52 (0.18) × 10^{-1} c	0.99
No scavenger	1.19 (0.02) × 10^{-1} a	0.99
0.1 mM EDTA-2Na	3.13 (1.00) × 10^{-4} c	0.65
10 mM *tert*-butanol	3.59 (0.42) × 10^{-3} d	0.98
50 μM $K_2Cr_2O_7$	5.55 (0.20) × 10^{-2} b	0.98
1 mM p-benzoquinone	6.56 (1.00) × 10^{-3} d	0.70
pH = 5.0	8.33 (2.08) × 10^{-4} b	0.95
pH = 6.2	4.13 (0.59) × 10^{-3} b	0.96
pH = 7.2	1.19 (0.02) × 10^{-1} a	0.99
pH = 8.3	2.15 (0.11) × 10^{-1} c	0.97
pH = 9.2	3.03 (0.08) × 10^{-1} d	0.99
0 mM HCO_3^-	1.19 (0.02) × 10^{-1} a	0.99
1 mM HCO_3^-	6.67 (0.35) × 10^{-2} b	0.98
2 mM HCO_3^-	5.45 (0.18) × 10^{-2} c	0.99
5 mM HCO_3^-	1.69 (0.26) × 10^{-3} d	0.82
0 mg L^{-1} SRNOM	1.19 (0.02) × 10^{-1} a	0.99
2 mg L^{-1} SRNOM	4.64 (0.39) × 10^{-2} b	0.99
5 mg L^{-1} SRNOM	3.07 (0.40) × 10^{-3} c	0.99
10 mg L^{-1} SRNOM	2.60 (0.35) × 10^{-3} c	0.96

*The degradation experiments were performed in the dark without ZnO nanowires. **The degradation experiments were performed under simulated sunlight without ZnO nanowires. Numbers in parentheses are standard deviations from three replicates. In each treatment group (e.g., ZnO nanowire dosage, different scavengers, varying solution pH, bicarbonate concentration, and NOM concentration) different letters indicate the significant difference in means of degradation rate constants by the LSD post-hoc comparison test at $p < 0.05$.

Table 2.3. Dissolution of ZnO nanowires (20 mg L^{-1}) after 3-hrs experiment under different solution pH.

pH	Dissolved Zn^{2+} concentration (mg L^{-1})
5.0	9.61 ± 0.18
6.2	7.61 ± 0.08
7.2	1.44 ± 0.05
8.2	0.74 ± 0.04
9.1	0.10 ± 0.01
pH 7.2, after 5 cycles	2.79 ± 0.04

Reactive Species in Photodegradation

In photocatalysis several reactive species (e.g., h^+, •OH, e^-, and O_2•$^-$) may be produced and react with cephalexin [32, 116, 117]. The photodegradation rates of cephalexin were significantly reduced by adding a h^+ scavenger (0.1 mM EDTA-2Na), •OH scavenger (10 mM *tert*-butanol), and O_2•$^-$ scavenger (1 mM p-benzoquinone), respectively ($p < 0.05$, Table 2.2 and Figure 2.3). Further comparison showed that the inhibitory effect of *tert*-butanol was lower than that of EDTA-2Na. Knowing that the combination of h^+ with OH^- leads to the production of •OH, these observations indicate that •OH and O_2•$^-$ are the main reactive species contributing to the photocatalytic degradation of cephalexin. Addition of the e^- scavenger (50 μM $K_2Cr_2O_7$) remarkably suppressed the photodegradation of cephalexin but with a lower inhibition effect than other three scavengers ($p < 0.05$, Table 2.2 and Figure 2.3). Thus, photo-induced electrons (e^-) had a smaller contribution to the photodegradation of cephalexin.

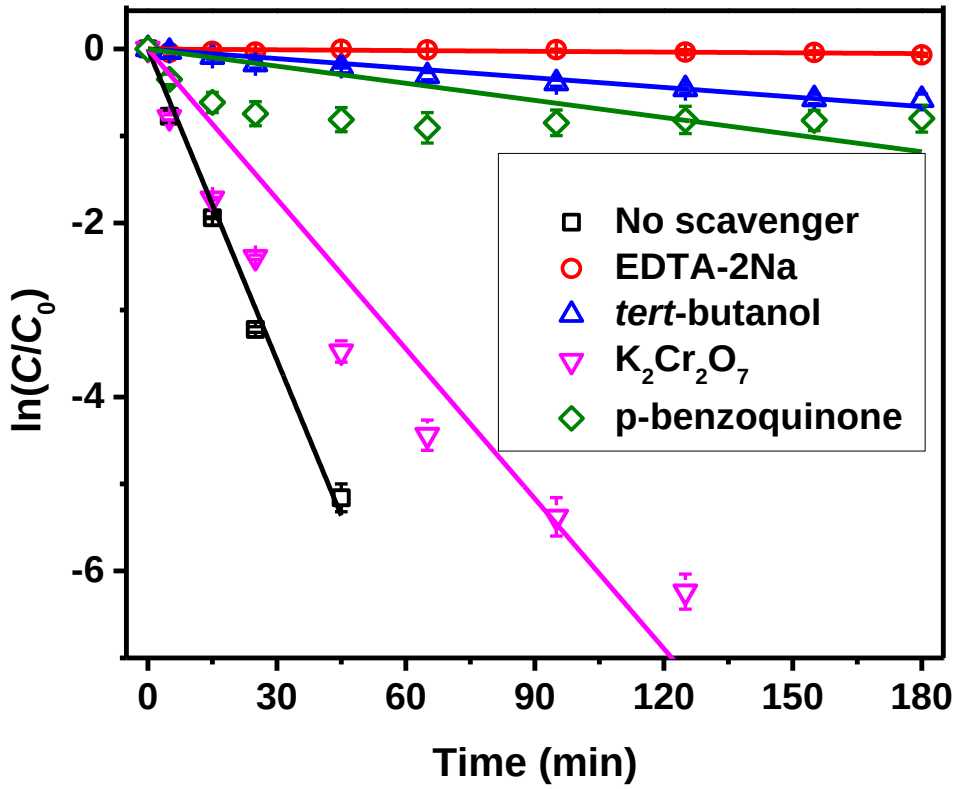

Figure 2.3. Effect of various free radical scavengers on the photodegradation of cephalexin by ZnO nanowires (20 mg L^{-1}) at solution pH of 7.2 under simulated sunlight. Error bars represent the standard deviations (n = 3). Solid lines were fitted to the first-order kinetic equation.

Effect of Solution pH

As shown in Figure 2.4a and Table 2.2, the photodegradation rate of cephalexin was significantly accelerated and the *k* value increased from 8.33×10^{-4} min^{-1} to 3.03×10^{-1} min^{-1} as the pH increased from 5.0 to 9.2 ($p < 0.05$). A similar trend was observed for the degradation of amoxicillin, ampicillin, and cloxacillin by ZnO under UV irradiation [33], which was thought to be collectively controlled by the attractive and repulsive forces between catalyst surfaces and antibiotics. Along this line of thought, at a solution pH less than the pH_{pzc} of 6.8, the attraction between positively charged ZnO nanowires (Table 2.1 and Supplementary Figure A4) and the zwitterionic and/or anionic species of cephalexin (Supplemental Figure A1b) would have enhanced the photodegradation of cephalexin. At a solution pH greater than pH_{pzc}, the repulsion between anionic cephalexin and negatively charged ZnO nanowires would have limited photocatalytic degradation. Surprisingly, the opposite trends were observed in this study, suggesting that electrostatic interaction had little effect on the photodegradation of cephalexin by ZnO nanowires. A previous study showed that solution pH can affect the generation of radical species [103]. At a lower pH the h^+ holes were the major oxidation species, whereas at a neutral or higher pH, hydroxyl radicals (•OH) are mostly responsible for the oxidation. Under alkaline conditions, the increased OH^- concentration was beneficial for the production of •OH species by reacting with h^+ [32, 33, 103]. As hydroxyl radicals (•OH) were shown to play a dominant role in the photodegradation of cephalexin with ZnO nanowires (Table 2.2 and Figure 2.3), enhanced •OH production at higher pH contributed to greater cephalexin degradation. Additionally, the dissolution of ZnO nanowires was more pronounced at a low pH range (5.0–6.2) (Table 2.3) [121], which could partly explain the negligible cephalexin degradation at pH 5.0 and 6.2 in addition to limited generation of •OH.

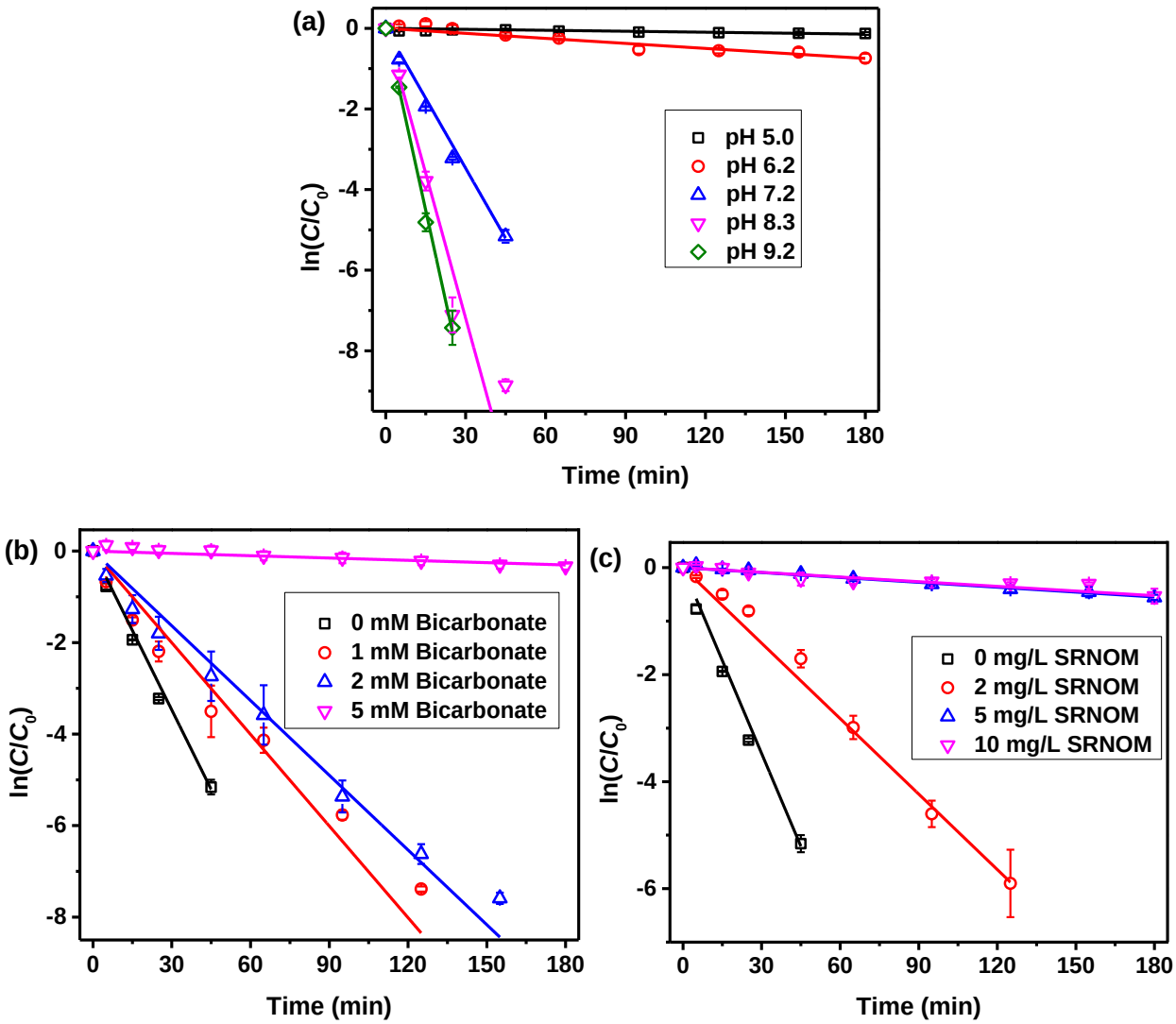

Figure 2.4. Effects of initial solution pH (a), bicarbonate (b) and Suwannee River natural organic matter (SRNOM) (c) on the photodegradation of cephalexin by ZnO nanowires (20 mg L^{-1}) under simulated sunlight. Error bars represent the standard deviations (n = 3). Solid lines were fitted to the first-order kinetic equation.

Effect of Bicarbonate

Cephalexin degradation decreased with increasing bicarbonate concentration (1, 2, and 5 mM) at pH 7.2 as shown in Figure 2.4b. The *k* value decreased from 1.19×10^{-1} min^{-1} at 0 mM bicarbonate to 6.67×10^{-2}–1.69×10^{-3} min^{-1} at 1–5 mM bicarbonate ($p < 0.05$, Table 2.2). Based on speciation calculations using the p*K*a values (i.e., pKa_1 = 6.3 and pKa_2 = 10.3) for a $H_2CO_3/HCO_3^-/CO_3^{2-}$ system [128], at pH 7.2 the predominant species are HCO_3^- (88.8%) and H_2CO_3 (11.2%). HCO_3^- generally acts as a scavenger of •OH by converting •OH to a selective carbonate radical ($•CO_3^-$) [107], which would considerably decrease the photocatalytic efficiency of ZnO nanowires due to the lower reactive activity of $•CO_3^-$ [106]. Additionally, inorganic ions including HCO_3^- can be adsorbed on the surface of TiO_2 in the order of $HPO_4^{2-} > HCO_3^- > SO_4^{2-} > NO_3^- > Cl^-$, even when TiO_2 is negatively charged [129]. Therefore, the inhibition effect of co-existing HCO_3^- on cephalexin degradation might be partly explained by the formation of a HCO_3^- layer on the surface of the ZnO nanowires which further impairs the approach of cephalexin to the ZnO nanowires [130]. Similarly, Torki and Faghihian [31] revealed that HCO_3^- inhibited the photodegradation of cephalexin when using synthesized Fe_3O_4@PPY–NiO, Fe_3O_4@PPY–NiS, and Fe_3O_4@PPY–NiO–NiS as catalysts under visible light. In contrast, several researchers found that HCO_3^- had a negligible or even enhanced effect on photocatalytic degradation of antibiotics. Hu et al. [36] and Song et al. [32] both showed that the addition of bicarbonate (HCO_3^-) enhanced the photocatalysis of sulfamethoxazole by TiO_2 and g-C_3N_4, respectively. These observations may be due to the high selective reactivity of $•CO_3^-$ with the aniline group of sulfamethoxazole ($k = 6 \times 10^8$ M^{-1} s^{-1}). Likewise, a very recent paper by Qian et al. [115] speculated that the generated $•CO_3^-$ radicals can selectively react with the electron-rich groups of cephalexin, such as the primary amine (Supplemental Figure A1a), which would significantly increase the oxidation of cephalexin

by thermally-activated persulfate. Conversely, a negligible effect of HCO_3^- on the photodegradation of sulfadiazine and sulfamerazine by g-C_3N_4 was also observed by Song et al. [32]. Clearly, whether bicarbonate plays an inhibitory or enhancing role in the degradation of antibiotics is dependent on the type of dominant radical species and the chemical properties of the antibiotic. In addition to bicarbonate (HCO_3^-), other inorganic anions such as Cl^- and NO_3^- are also ubiquitous in water. Similarly, it is hypothesized that Cl^- and NO_3^- may inhibit the photodegradation of cephalexin by preferential adsorption on the photocatalyst surface, competitive reaction with holes (h^+), and consuming produced •OH, as reported in the literature [98, 131]. Nonetheless, this hypothesis needs to be confirmed in future studies.

Effect of SRNOM

Figure 2.4c presents the effect of SRNOM on the degradation efficiency of cephalexin by ZnO nanowires under simulated sunlight. As expected, the *k* value decreased from 1.19×10^{-1} min^{-1} in the absence of SRNOM to 4.64×10^{-2}–2.60×10^{-3} min^{-1} with the presence of 2–10 mg L^{-1} SRNOM ($p < 0.05$, Table 2.2), which is consistent with previous studies [32, 104, 105]. As SRNOM concentration increased from 0 to 10 mg L^{-1}, the degradation efficiency dramatically decreased from near 100% to 40.9%. This could be attributed to the quenching effect of SRNOM on the major reactive species (i.e., •OH and O_2•$^-$) [106]. NOM is a well-known scavenger of reactive radicals especially at high concentrations [104]. Additionally, NOM is capable of attenuating light and consuming most of photons [104, 108]. SRNOM sorbed on the ZnO nanowire surface occupied the reactive sites as evidenced by the more negative zeta potentials for the ZnO nanowires (Table 2.1), which further inhibited the approach of cephalexin molecules onto the surface of the ZnO nanowires [105]. It should be noted that NOM can also act as a photosensitizer to enhance photolysis. NOM was observed to promote indirect photolysis of caffeine, sulfamethoxazole, and diuron [132].

Dissolved organic matter (DOM) was excited to triplet states (^{3}DOM*) that are highly reactive with organic pollutants [133]. For example, ^{3}DOM* effectively facilitated the photo-transformation of 17β-estradiol [134] and 2,4-dihydroxybenzophenone [135].

Identification of Intermediates and Transformation Pathways

FED calculations were used to predict the positions of free radical attack, which were corroborated by the fact that •OH radicals selectively attack positions within a molecule (i.e., intramolecular selectivity) [136]. As given in the Supplemental Table A2, C23 had the highest value of $2FED_{HOMO}^2$, followed by C18 and C17, and then C19, N24, and C20. Thus, these positions would be prone to electron extraction. The $FED_{HOMO}^2 + FED_{LUMO}^2$ values decreased in the order of C23 > C7 ≈ C18 > C17 > C8 > C2 ≈ C3, which may be easily attacked by free radicals [34]. Thus, these results could provide a theoretical basis for predicting the chemical structures of intermediates and photocatalytic degradation pathways in combination with LC-QTrap-MS/MS spectra (Supplemental Figure A7, P1–P7).

Photodegradation products of cephalexin were analyzed by LC-MS full scan and enhanced product ion scan. Their structures were obtained in the ChemSpider database or constructed by ChemDraw software (ChemOffice programs, PerkinElmer, Waltham, MA) following molecular formula calculation based on the MS spectra and m/z values. The proposed structures of products and degradation pathways are depicted in Figure 2.5. According to the FED theory and identified products, the photocatalytic pathway of cephalexin by ZnO nanowires mainly included hydroxylation, demethylation, decarboxylation, and dealkylation. Photocatalytic product 1 (P1, m/z = 386.67) was produced by •OH/•O_2^- attack, leading to β-lactam ring opening through hydroxylation and demethylation via substitution of methyl with hydroxyl addition. Previous studies have reported similar degradation pathways for amoxicillin and cephalosporins [137, 138].

Despite the highest values of $2FED_{HOMO}^2$ and/or $FED_{HOMO}^2 + FED_{LUMO}^2$ at C23 and C18 of the phenyl ring, an earlier study by Hsu et al. [138] demonstrated that the phenyl group (–R2) of cephalexin is unlikely to be oxidized before the core structure (Supplemental Figure A1a). Moreover, the substituent (–R1) at C3 may sterically hinder and block the reactive sites in the core structure. Thus, demethylation at C3 with hydroxyl addition was more likely, similar to the degradation of sulfamethoxazole [139]. Intermediate P2 (m/z = 370.72) was generated by losing one O atom at the C9 position. Decarboxylation and dealkylation led to the formation of P3 (m/z = 327.88), which has been documented in degradation of cephalexin and other pharmaceuticals [30, 137, 140]. Subsequently, the oxidation product P4 (m/z = 192.72) and small fragment P7 (m/z = 139.93) were produced as a result of C–N cleavage in P3. Hsu et al. [138] also reported that L–phenylglycine, the precursor of P7, was released as a byproduct after 3 h of cephalexin oxidation by MnO_2. Furthermore, dehydration with the loss of H_2O and oxygen can form the intermediates P5 (m/z = 174.74) and P6 (m/z = 158.72), respectively. In this study seven products were tentatively proposed based on the MS spectra and m/z values in the photocatalytic degradation pathways, which were justified by calculated theoretical FED and reported pathways in the literature. Due to the lack of authentic standards, these intermediates were not confirmed and the transformation pathway was thus speculative. Nonetheless, this approach has been widely used in other studies [30, 115, 138]. Furthermore, cephalexin and its transformation products could be oxidized into smaller molecules by attack from free radicals, which should be explored in future studies. As the transformation products may be also bioactive against microorganisms, future work should examine the bioactivity of photodegradation intermediates.

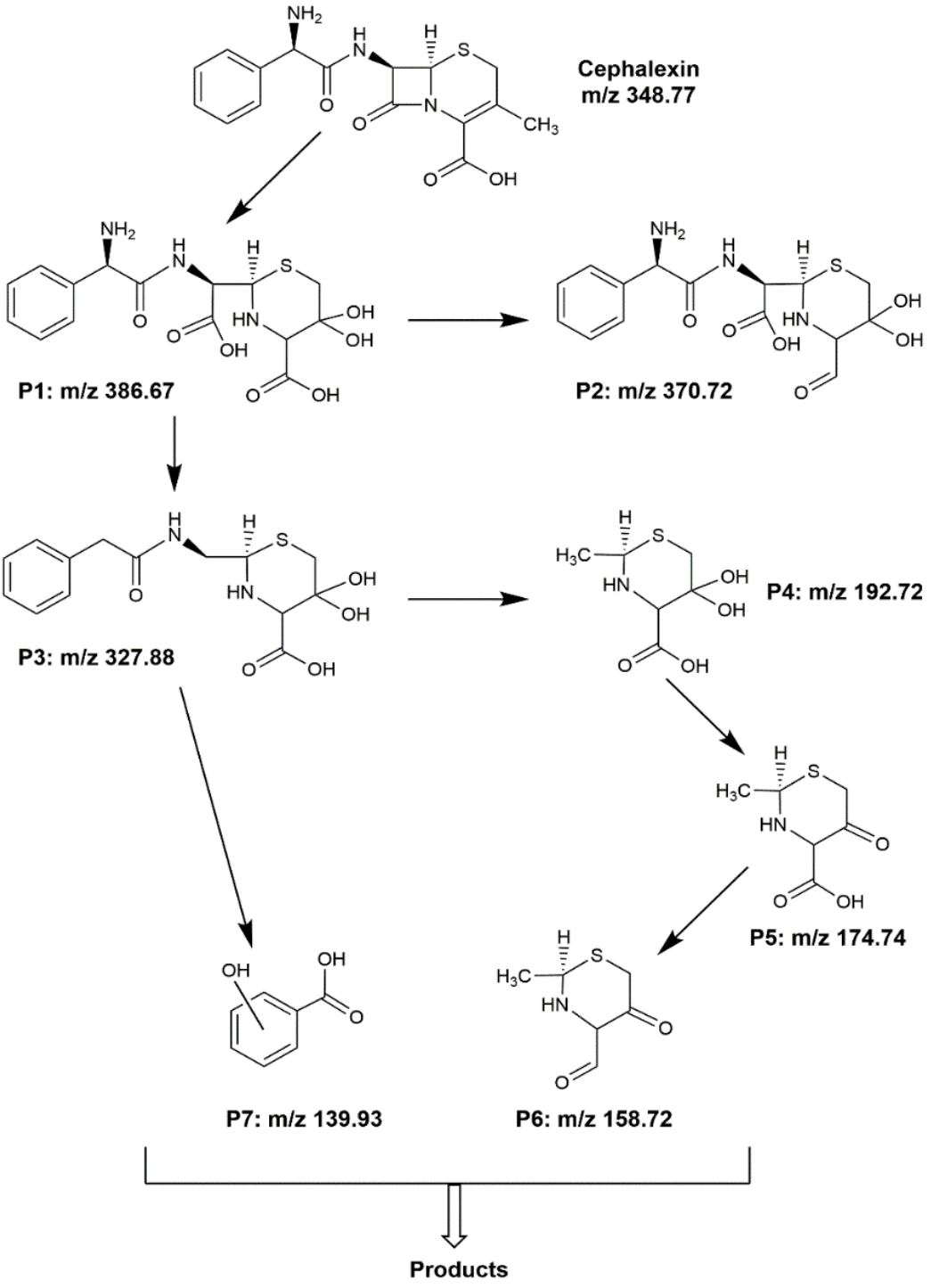

Figure 2.5. Proposed photocatalytic degradation pathways of cephalexin by ZnO nanowires under simulated sunlight irradiation.

Conclusion

In this study, laboratory-scale photocatalytic degradation of cephalexin under simulated sunlight using ZnO nanowires was investigated for efficiency, water chemistry effect, and degradation pathways. Degradation efficiency of cephalexin substantially increased with increasing solution pH (particularly at alkaline condition) in the presence of ZnO nanowires, indicating ZnO nanowires have excellent photocatalytic activity for cephalexin. Photodegradation of cephalexin decreased with increasing HCO_3^- and NOM concentrations, due to scavenging of the active radical species (•OH and $•O_2^-$) that are largely responsible for the degradation of cephalexin. Therefore, effective strategies will need to be designed when using ZnO nanowires in water and wastewater treatment at elevated levels of HCO_3^- and/or NOM. For example, ZnO nanowires may be embedded into membrane reactors that can be used for advanced water and wastewater treatments. Future research should focus on developing feasible engineering designs that incorporate ZnO nanowires for the removal of contaminants from both water and wastewater as well as assessing the bioactivity of transformation products during photodegradation.

Author Contribution: Jianzhou He and Wei Zhang conceived and designed the research experiments; Jianzhou He conducted the experiments, analyzed the data and wrote the manuscript; Yaozhong Zhang and Junghoon Yeom provided the ZnO nanowires and the SEM characterization; Yang Guo performed the theoretical calculation; Geoff Rhodes provided assistance on the LC-MS/MS method; Junghoon Yeom, Hui Li, and Wei Zhang reviewed and edited the manuscript.

CHAPTER III

BIOCHAR AMENDMENT CHANGES SOIL-BOUND FRACTIONS OF SILVER NANOPARTICLES AND IONS BUT NOT THEIR UPTAKE BY RADISH AT AN ENVIRONMENTALY RELEVANT CONCENTRTAION

Abstract

Plant uptake of silver nanoparticles (Ag NPs) and ions (Ag^+) largely depends on their exchangeable and soil-bound fractions, which may be influenced by biochar amendment. This study investigated the effects of biochar amendment (0.1% and 1.0%) on soil sorption of Ag NPs and Ag^+, their soil-bound fractions, and their uptake and translocation by radish grown in a loamy sand soil spiked with 1 mg kg^{-1} Ag NPs or Ag^+. Sorption of Ag^+ to the soils was much greater than that of Ag NPs, mainly because negatively charged soil particles attract Ag^+ ions but repel negatively charged Ag NPs. Biochar amendment at 1.0% (by weight) significantly decreased the reducible fraction of Ag^+ ions in soils with and without radish plants and increased the oxidisable fraction of Ag NPs in soils with radish plants. Biochar amendment had no significant effect on Ag uptake by radish plants ($p > 0.05$), probably due to low exchangeable Ag fractions in all experimental treatments. In this short-term experiment (35 days), the addition of 1 mg kg^{-1} Ag NPs or Ag^+ did not substantially elevate the level of Ag in radish roots (0.05 ± 0.02–1.06 ± 0.98 mg kg^{-1}) and shoots (0.01 ± 0.00–0.03 ± 0.01 mg kg^{-1}), compared to the blank control ($p > 0.05$). Radish uptake of Ag NPs and Ag^+ at the environmentally-relevant concentration was low with root concentration factors between 0.03 ± 0.03 to 0.29 ± 0.21 and root-to-shoot translocation factors between 0.08 ± 0.10 to 0.89 ± 1.21, which may partially explain the non-significant effect of biochar amendment on Ag uptake.

Introduction

Silver (Ag) nanoparticles (NPs) are one type of the most widely used engineered nanomaterials and are increasingly incorporated into industrial and commercial products [5, 141]. It is generally believed that the production, use, and disposal of Ag NPs will lead to their dissemination into agricultural soils [42, 43, 47]. Soils are thus considered a major sink or reservoir for Ag NPs [46], and the predicted concentrations of Ag NPs in soils were 0.02 μg kg^{-1} and 0.1 μg kg^{-1} in realistic and high emission scenarios, respectively [47]. Also the annual increase of Ag NPs in soils was estimated at 22.7 ng/kg in Europe and 8.3 ng kg^{-1} in the US, with a more rapid increase in sludge-treated soils (1.58 μg kg^{-1} in Europe and 0.66 μg kg^{-1} in the US). This is of particular concern because the concentrations of Ag NPs in sewage sludge can be as high as 1.68 mg/kg in Europe and 1.55 mg kg^{-1} in the US [46]. More importantly, if the released Ag NPs in soils accumulate in food crops and enter the human food chain, dietary exposure to Ag may threaten human health.

A number of studies have found that Ag in either particulate or ionic form can be taken up by plants [50-57]. For example, when duckweed (*Landoltia punctata*) was exposed to 10 mg L^{-1} of total Ag concentration in the form of either Ag NPs, Ag_2S NPs, or $AgNO_3$ for 24 h in a hydroponic system, Ag was detected on and in the roots of duckweed [142]. Using single-particle inductively coupled plasma mass spectrometry and transmission electron microscopy energy-dispersive spectroscopy, Li et al. [143] detected Ag-containing NPs in the leaves of soybean and rice after exposure to Ag NPs (30 mg L^{-1} for soybean and 1 mg L^{-1} for rice) and Ag^+ ions (0.5 mg L^{-1}) in hydroponic systems. Similarly, Ag NPs were taken up by the roots and subsequently translocated in the shoots of *Arabidopsis thaliana* cultivated in ¼ Hoagland's solution containing 2 mg L^{-1} Ag NPs [54]. When exposed to 70 mg kg^{-1} of Ag NPs or Ag^+ ions spiked into a Templeton silt loam, silverbeet (*Beta vulgaris L. ssp. maritima (L.) Arcang.*) and spinach (*Spinacia oleracea L.*) could

accumulate 5–9 mg Ag kg^{-1} in the edible parts, which may pose human health risks [144]. Dimkpa, et al. [145] also found Ag NPs in the shoots of wheat (*Triticum aestivum* L.) after root exposure to 2.5 mg kg^{-1} Ag NPs or Ag^+ ions in a sand growth matrix, suggesting root uptake and translocation of Ag in wheat. Nonetheless, the relative contribution of Ag NPs and Ag^+ ions to Ag plant uptake has not yet been determined. Cvjetko et al. [51] found that equal amounts of Ag NPs or Ag^+ accumulated in the roots and leaves of tobacco (*Nicotiana tabacum*), consistent with another study on nine vegetables [144]. In contrast, several studies have documented higher Ag contents in the roots after exposure to Ag NPs than to Ag^+ ions in hydroponics at total Ag concentrations of 50 μg L^{-1}–10 mg L^{-1} [53, 146-148]. Furthermore, the ionic Ag form tends to have higher translocation efficiency from roots to shoots than the nanoparticle form [149]. However, Yang et al. [146] reported that the translocation factor for ^{109}Ag in ^{109}Ag NPs was remarkably higher than that for ^{107}Ag in $^{107}AgNO_3$ in hydroponic Hewitt solutions. Given these aforementioned conflicting results, more research is needed on the relative significance of Ag NPs and Ag^+ ions uptake by plants.

In general, the negatively charged plant cell membrane attracts Ag^+ ions, thus facilitating their entry into plant cells through ion channels or by passive diffusion. Ag NPs could be potentially taken up by plant roots via the apoplastic or symplastic pathways and translocated to shoots through the vascular system as constrained by size exclusion limit (40–50 nm) of aqueous pores, and plasmodesmata [62-66]. Nonetheless, the size exclusion of plant roots may be overcome by endocytosis [62, 68, 69], and additional entry points due to physical and disease damage to roots and emergence of new secondary roots [64, 66]. Overall, plant uptake of Ag NPs largely depends on the bioavailability of Ag in soils [144, 150, 151]. The enhanced aggregation and/or interaction with soil moieties, e.g., iron oxides or organic matters (OM), could decrease the bioavailability of Ag NPs in soils. For example, the presence of soil OM increased the amount of Ag retained in the solid

phase and decreased the dissolved Ag levels [152]. Natural OM decreased the accumulation of Ag in wheat by strongly binding to dissolved Ag^+ [150]. Of particular importance is, therefore, to determine the fractions and bioavailability of Ag NPs associated with soils. Indeed, a well-established three-step sequential extraction method (known as the BCR method) has been widely used to determine the fractions and bioavailability of heavy metals in soils and sediments [153, 154]. It was suggested that the exchangeable fraction, the Fe/Mn oxides-bound fraction, and the OM-bound fraction are potentially bioavailable to plants at varying degrees [151, 155, 156]. Recently, Zhang, Musante, White, Schwab, Wang, Ebbs and Ma [151] successfully applied the BCR method to estimate the soil fractions of cerium oxide nanoparticles in two soil types to assess their bioavailability to radish (*Raphanus sativus* L). However, to our best knowledge little has been done to examine the soil-bound fractions of Ag NPs so as to inform their bioavailability to plants [151, 155, 157].

Reducing the mobility and bioavailability of Ag NPs in soils is critical to minimizing their migration from soils to plants. Soil amendments with biochar may be an effective strategy to minimize the entry of nanoparticles into the human food chain [71-74], and are being promoted as a sustainable agricultural practice. For example, uptake and phytotoxicity of Ag NPs (100–1,000 mg L^{-1}) in rice (*Oryza sativa* L.) grown hydroponically were significantly suppressed by 2% (w/v) biochar, due to decreased bioavailability of Ag NPs [71]. Similarly, the addition of rice husk-derived biochar to a hydroponic system (3% wt) lowered the Cu content in the roots and shoots of wheat (*Triticum aestivum* L.) by 3.3–4.9 and 3.7–7.8 fold, respectively, due to significant sorption of Cu^{2+} to biochar and blockage of Cu access to plant roots [74]. Nonetheless, most previous studies exposed plants to unrealistically high concentrations of Ag NPs in hydroponic (up to 1,000 mg L^{-1}) or soil systems (up to 10,000 mg kg^{-1} in soils) [51, 71, 144, 158], and their results may not be applicable in realistic scenarios. This knowledge gap may limit our ability to assess the risks of

Ag NPs via human dietary exposure and the feasibility of biochar amendment as a mitigation strategy.

Therefore, this study aimed to examine the effect of biochar amendment on the sorption of Ag NPs and Ag^+ ions to soils and their soil-bound fractions, and further investigate the uptake and accumulation of Ag NPs and Ag^+ ions at an environmentally-relevant Ag level in soils, as characterized by total Ag concentrations in plant roots and shoots, as well as the root concentration factor (RCF) and root-to-shoot translocation factor (TF). The spiked concentration of Ag NPs or Ag^+ ions (1 mg kg^{-1}) was close to environmentally-relevant levels [159, 160]. Although much greater than the predicted concentrations of Ag NPs in soils, it was comparable to that in sewage sludge [46]. This Ag level was also needed for accurate measurement in the soil, root and shoot samples. Additionally, the BCR sequential extraction method and soil pore water extraction were used to gain more insight into the bioavailability of spiked Ag NPs and Ag^+ in radish-growing and radish-free soils.

Materials and Methods

Chemicals, Biochar and Soil

Polyvinylpyrrolidone (0.6%) stabilized Ag NPs (1000 mg L^{-1}) were obtained from the US Research Nanomaterials, Inc. (Texas, US). Silver nitrate ($AgNO_3$) was purchased from Fisher Scientific Inc. (Hampton, US). The morphology of Ag NPs was characterized by transmission electron microscopy (TEM, JEOL 2200FS, Japan). The size and surface charge were measured by dynamic light scattering using a Zetasizer (Nano-ZS, Malvern Instruments, UK). TEM imaging confirmed that the Ag NPs were spherical (Supplementary Figure B1a in Appendix B) with a mean diameter of 20.9 nm. The Ag NPs solution had a pH of 6.2, a zeta potential of −11.2 mV, and an average hydrodynamic diameter of 63.7 nm with a polydispersity index of 0.15. Aggregation

kinetics indicated that the Ag NPs were stable (Figure B1b) mainly due to steric repulsion induced by polyvinylpyrrolidone coated on the surface of Ag NPs [161]. Acetic acid, hydroxylammonium chloride, hydrogen peroxide, ammonium acetate, and nitric acid of analytical reagent grade were used.

The biochar was produced by Biogenic Reagents LLC. (Michigan, US) from pinewood via pyrolysis at 650 °C for about 30 min in a rotary reactor. As per the proximate analysis, the fixed carbon, ash, and volatile matter contents (by weight) were 90%, 5% and 4%, respectively. The elemental content of biochar was 76.9% C, 0.2% N, and 1.2% H by weight. The specific surface area and pore volume were determined to be 543.6 m^2 g^{-1} and 0.3 cm^3 g^{-1}, respectively [162]. Its morphology was examined using scanning electron microscopy (SEM, JEOL 7500F, Japan) and exhibited a highly porous structure and rough surface (Supplementary Figure B2).

The tested soil was collected at a depth of 0–15 cm, air-dried, and passed through a 2-mm sieve before use. The soil was classified as a loamy sand containing 74.6% sand, 24.6% silt, and 0.78% clay as determined by a laser particle size analyzer (Malvern Mastersizer 2000E, UK). It had a pH of 7.8, OM of 2.3%, and cation exchange capacity (CEC) of 7.9 meq/100g. Biochar amendment (0.1% and 1.0%) had an insignificant influence on the soil pH (Supplementary Figure B3), OM, and CEC [162]. The background Ag concentration in soil was measured at 0.26 mg kg^{-1}.

Radish Growth Experiment

Radish plants were grown in soil pots spiked with Ag (Ag NPs or $AgNO_3$) and fifteen selected pharmaceuticals (acetaminophen, caffeine, carbadox, carbamazepine, estrone, lamotrigine, lincomycin, monensin, oxytetracycline, sulfadiazine, sulfamethoxazole, triclosan, trimethoprim, tylosin, and 17 β-estradiol) to mimic the co-contamination with pharmaceuticals, engineered nanoparticles, and/or heavy metals [163]. This paper only reports the study on Ag, with

the work involving pharmaceuticals reported in a companion paper [162]. The addition of pharmaceuticals did not change the biomass or Ag uptake of radish plants. The experimental design is summarized in Table 3.1. To evenly distribute Ag in the soil, about 1 kg of soil was first spiked with Ag NPs or Ag^+ along with the fifteen pharmaceuticals in acetone and then thoroughly mixed in a fume hood [162, 164]. After solvent evaporating, the spiked soil portion and a predetermined amount of biochar were mixed with a predetermined amount of clean soil in a clean motorized concrete mixer to homogenize the spiked Ag and pharmaceuticals into the soil. The resultant soil samples had 1 mg kg^{-1} of added Ag (Ag NPs or Ag^+) with 0.1 or 1 mg kg^{-1} of each pharmaceutical and contained 0%, 0.1% or 1.0% of the biochar by weight. The biochar-free and biochar-amended soils in the absence of Ag and pharmaceuticals were used as the blank control.

Table 3.1. Radish growth in soils in the absence (blank) and presence of spiked $AgNO_3$ and Ag NPs without (0%) or with (0.1% and 1%) biochar amendment*.

Treatment	Biochar	Ag NPs	Ag^+	15 Pharmaceuticals	Radish growth pots	Radish-free pots
blank	0.0%	/	/	/	1	0
	0.1%	/	/	/	1	0
	1.0%	/	/	/	1	0
$AgNO_3$	0.0%	⁄	1 mg kg^{-1}	0.1 mg kg^{-1}	3	2
	0.1%	⁄	1 mg kg^{-1}	0.1 mg kg^{-1}	3	2
	1.0%	⁄	1 mg kg^{-1}	0.1 mg kg^{-1}	3	2
Ag NPs	0.0%	1 mg kg^{-1}	/	1 mg kg^{-1}	3	2
	0.1%	1 mg kg^{-1}	/	1 mg kg^{-1}	3	2
	1.0%	1 mg kg^{-1}	/	1 mg kg^{-1}	3	2

*Note: In total 33 pots included 21 pots with the radish plants and 12 pots without the radish plants. The radish-free pots were designed to sample soils for pore water extraction. The radish pots had 2 radish seedlings. High concentration (1 mg kg^{-1}) of each pharmaceutical was co-added with Ag NPs, whereas low (0.1 mg kg^{-1}) pharmaceutical concentration was added with $AgNO_3$.

The prepared soil samples were transferred to plastic pots (14.6 cm diameter × 10.8 cm height) at ~ 1 kg per pot. Five radish seeds (Burpee & Co., Warminster, PA) were directly sowed in each pot. After germination, plants were thinned to two seedlings per pot. Radish plants were grown in a climate-controlled greenhouse with natural sunlight at 25/21 °C day/night. Soil moisture level was maintained at 60% of the predetermined water-holding capacity by adding deionized (DI) water daily to compensate for evapotranspiration water loss. After 35 days, radish plants were sampled and washed with DI water to remove any attached soil particles. Two plants in each pot were divided into root and shoot samples, weighed, freeze-dried, and ground into fine powders. All plant samples were kept in a desiccator until further use. Meanwhile, the soil samples in the radish-growing and radish-free pots were collected, and soil pore water was extracted immediately using a centrifugation-filtration method described previously [162, 164]. Briefly, aliquots (25 g) of the soil sample were placed on a layer of glass wool in a 20-mL disposable plastic syringe. The syringe was inserted into a 50-mL polypropylene Corning tube, which was centrifuged at 4,000 × *g* for 40 min. The resulting pore water was stored at 4°C after passing through a 0.45-μm membrane filter, and the soil samples were freeze-dried for further Ag analysis.

Ag Sorption Experiment

Batch sorption experiments were conducted in duplicate to examine the sorption of Ag NPs and Ag^+ to the soils with different biochar amendment (0%, 0.1%, and 1.0%). Soil samples of 0.5 g were placed in 50-mL polypropylene Corning tubes, followed by adding 25 mL of 5 mM KNO_3 containing a series of Ag NPs concentrations (0, 1.1, 2.2., 5.6, 11.1, 22.2, 55.6, 111, and 222 mg L^{-1}) or $AgNO_3$ concentrations (0, 1, 2, 5, 10, 20, 50, 100, and 200 mg L^{-1}), respectively. The resultant mixtures were shaken for 24 h at room temperature in the dark, centrifuged at 2000 × *g*

for 5 min and filtered through 0.45-μm membrane filters (Millipore, US). All filtrates were kept at 4 °C prior to analysis.

BCR Sequential Extraction

To examine the effect of biochar amendment on soil-bound Ag fractions in the soil samples and to further link the extractable fractions with the uptake of Ag, the well-established BCR method was used to extract Ag from the soil samples collected from the radish-growing and radish-free pots on Day 35 according to Wang et al. [165]. First, to measure the exchangeable fraction (f1) 1 g of soil was mixed with 20 mL of 0.1 M acetic acid in a shaker at 30 ± 5 rpm and 25 °C for 16 h. The extract was centrifuged at 3000 × *g* for 20 min, and the supernatant was collected. The residue solid was washed by shaking for 15 min with 20 mL of DI water, followed by centrifugation. Afterward, the Fe/Mn oxide-bound reducible fraction (f2) was extracted by adding 20 mL of 0.5 M hydroxylammonium chloride to the residue solids from the first step, and then the mixture was shaken at 30 ± 5 rpm and 25 °C for 16 h. The extract was again separated and the residue was washed as in the previous step. It is noted that Ag (assuming 1 mg kg^{-1} in the soil completely dissolved into the aqueous phase) would not precipitate with 0.5 M hydroxylammonium chloride as confirmed by the MINTQ calculation (Supplementary Figure B4). Third, in order to measure the OM-bound oxidisable fraction (f3), 5 mL of 30% hydrogen peroxide was added to the residue from the second step to oxidize OM. The mixture was digested for 1 h at 25 °C and for another hour at 85 °C, with occasional shaking. Then a second 5 mL aliquot of H_2O_2 was added, followed by digestion for 1 h at 85 °C. Afterwards the residue was extracted with 25 mL of 1 M ammonium acetate solution (pH of 2.0 adjusted by HNO_3) by shaking at 30 ± 5 rpm and 25 °C for 16 h. The extract was collected and the residue was washed again. Finally, to measure the residual fraction (f4) the soil residue from the third step was digested with 10 mL of HNO_3

(70%). All extraction experiments were conducted in triplicate for each sample. Because Ag NPs are not stable in the BCR extraction reagents and background Ag in soils would be also extracted, this study could not differentiate the Ag sources and species in the extracts. All Ag forms were measured as total Ag concentration using an atomic absorption spectrometer (AAS) after acid digestion.

Analytical Methods

Before analysis, the filtrates from the sorption experiments, BCR extracts, soil pore water samples, and soil samples were digested with concentrated HNO_3 at 115 ºC [166]. The radish shoot and root samples were digested with HNO_3 and H_2O_2 (v:v = 4:1) at 115 ºC [143]. Afterwards, total Ag concentration in the digested samples was determined using a flame AAS (AAnalyst 400, PerkinElmer, Waltham, MA). Due to the low Ag levels in the soil pore water samples and the radish root and shoot samples, the total Ag concentration in these samples was measured by a graphite furnace AAS (PinAAcle 900T, PerkinElmer, Waltham, MA) after acid digestion.

Data Analysis

The sorbed Ag NPs or Ag^+ by the soil in the batch sorption experiments was calculated from the difference between the initial and final Ag concentrations using Eq. (3.1).

$$Q_s = (C_0 - C_e)\frac{V}{m} \quad (3.1)$$

where Q_s is the amount of Ag sorbed to the soils (mg g^{-1}), C_0 and C_e are the initial and final equilibrium Ag concentrations in solution (mg L^{-1}), respectively, V is the solution volume (L), and m is the mass of the soils (g).

The Ag sorption isotherms were fitted with the Langmuir model in Eq. (3.2), using the nonlinear fitting function in MATLAB R2017b software (The MathWorks Inc., Natick, MA).

$$Q_s = \frac{q_{max}k_L C_e}{1+k_L C_e} \quad (3.2)$$

where q_{max} is the maximum Ag sorption capacity (mg g^{-1}), and k_L is the Langmuir constant related to the affinity of binding sites (L mg^{-1}).

The RCF and TF values were calculated using Eqs. (3.3) and (3.4), respectively.

$$\text{RCF} = \frac{C_{root}}{C_{soil}} \quad (3.3)$$

$$\text{TF} = \frac{C_{shoot}}{C_{root}} \quad (3.4)$$

where C_{root}, C_{shoot}, and C_{soil} are the Ag concentrations in the radish root, shoot, and soil samples (mg kg^{-1}, dry weight), respectively. One-way ANOVA analysis was performed to test the statistical significance in means among experimental treatments using the least significant difference (LSD) test with SPSS 22.0 software for Windows (IBM Corp., Armonk, NY) at $p < 0.05$ level.

Results and Discussion

Radish Biomass

In all three treatments (i.e., blank, Ag NPs, and $AgNO_3$) the absence or presence of biochar (i.e., 0%, 0.1%, and 1.0%) had no significant effect on the root and shoot biomass of the radish plants in each pot (two plants) ($p > 0.05$, Figure 3.1). Intriguingly, the presence of 1 mg kg^{-1} Ag NPs and Ag^+ significantly increased the biomass of radish root by 68.3%–180.2% ($p < 0.05$), but had no significant effect on the radish shoots ($p > 0.05$). It is likely that the trace Ag levels in soil pore water (below the detection limit of the graphite furnace AAS, 0.5 μg L^{-1}, as discussed more in detail in Sections below) enhanced root growth, but were not high enough to translocate upward to influence shoot growth. Indeed, a very recent study also observed stimulation of the root biomass of rice (*Oryza sativa* L.) but no significant effect on shoot biomass when grown in a hydroponic system with 50 μg L^{-1} Ag NPs and Ag^+ for 14 days [146]. However, at higher exposure levels dose-dependent phytotoxicity of Ag NPs and Ag^+ has been observed to negatively influence

seed germination, root elongation, and/or biomass growth [71, 145, 147, 148, 158, 167]. To date no consensus has been reached regarding the phytotoxicity of Ag NPs and/or Ag^+, which is mainly attributed to the differences in exposure scenarios, physicochemical properties of nanoparticles, and plant species in various experimental settings. The increased root biomass was unlikely due to the presence of pharmaceuticals, as the level of pharmaceuticals differed by 10 fold between the Ag NPs (co-added with 1 mg kg^{-1} of each pharmaceutical) and $AgNO_3$ (co-added with 0.1 mg kg^{-1} of each pharmaceutical) treatments (Table 3.1), but there was no significant difference between the Ag NPs and $AgNO_3$ treatments for either the radish root or shoot biomass.

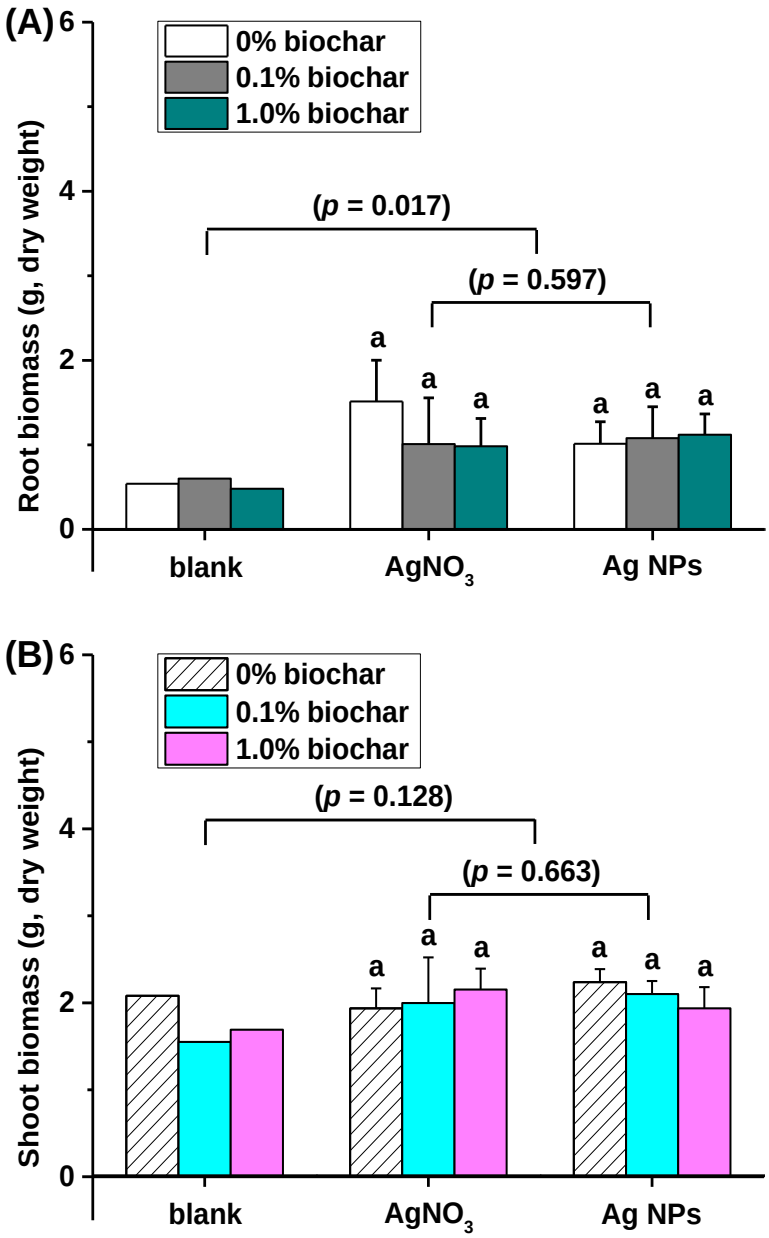

Figure 3.1. Dry biomass of radish roots (A) and shoots (B) harvested on Day 35 in each pot (two plants) in the absence (blank) and presence of spiked $AgNO_3$ and Ag NPs without (0%) or with (0.1% and 1%) biochar amendment. Error bars are the standard deviations (n = 3). Different letters indicate the significant difference in means at $p < 0.05$. Brackets indicate comparisons between the $AgNO_3$ and Ag NPs treatments as well as between the treatment groups with or without Ag addition, respectively.

Uptake of Ag by Radish

There were no significant differences in total Ag concentration in the radish roots and shoots for all treatments as a result of adding biochar, Ag NPs or $AgNO_3$ (Figure 3.2). Specifically, the biochar amendment (0.1% and 1.0%) had no significant effect on Ag uptake by the radish plants ($p > 0.05$). This result contradicts the study of Abbas et al. [71] who reported that biochar addition (2% w/v) decreased the uptake of Ag in rice (*Oryza sativa* L.) in a hydroponic system containing a Ag concentration of 100–1000 mg L^{-1}, which was at least 5 orders of magnitude greater than the Ag concentrations in the soil pore water (< 0.5 μg L^{-1} for the total Ag concentration of 1 mg kg^{-1} in the soil) in this study. Furthermore, the addition of 1 mg kg^{-1} Ag (Ag NPs or $AgNO_3$) did not substantially increase the uptake or accumulation of Ag in radish roots (0.05 ± 0.02 – 1.06 ± 0.98 mg kg^{-1}) and shoots (0.01 ± 0.00 – 0.03 ± 0.01 mg kg^{-1}), compared to the blank (0.03 ± 0.00 – 0.49 ± 0.05 mg kg^{-1} for the roots, and 0.01 ± 0.00 – 0.02 ± 0.01 mg kg^{-1} for the shoots at a background Ag of 0.26 mg kg^{-1}) ($p > 0.05$). As such, the insignificant effect of the various biochar amendment rates on Ag uptake likely resulted from the low level of Ag (1 mg kg^{-1}) in the soil, most of which was not readily bioavailable to the radish plants (discussed in more detail in Sections below). Since the Ag concentration of 1 mg kg^{-1} used in this study was similar to the measured background Ag concentration (0.26 mg kg^{-1}), but about 4 orders of magnitude greater than the predicted Ag concentration in soils due to the release of engineered Ag NPs [47], the Ag NPs released into soils are unlikely to result in a realistic increase of Ag in food crops, indicating a low food safety risk from the released Ag NPs.

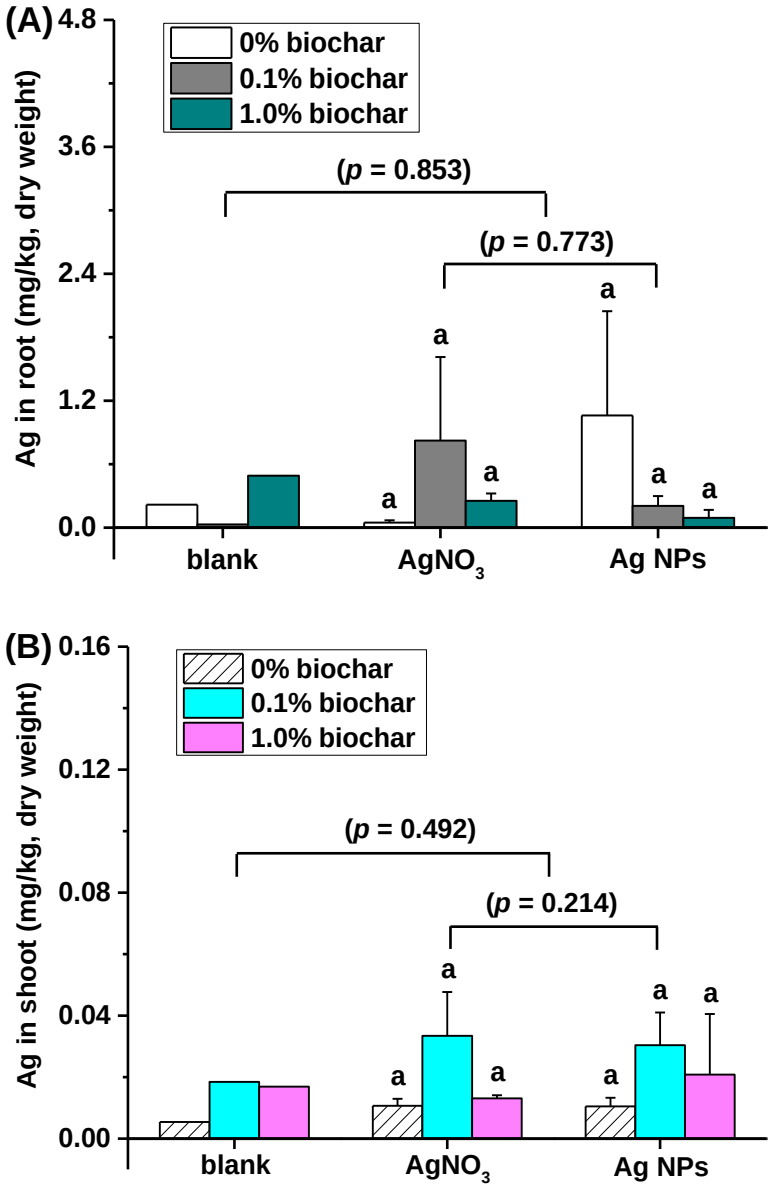

Figure 3.2. Total Ag concentrations in the roots (A) and shoots (B) of radish plants grown in soil pots in the absence (blank) and presence of spiked $AgNO_3$ and Ag NPs without (0%) or with (0.1% and 1%) biochar amendment. Error bars are the standard deviations (n = 3). Different letters indicate the significant difference in means at $p < 0.05$. Brackets indicate the comparisons between the $AgNO_3$ and Ag NPs treatments as well as between the treatment groups with or without silver addition, respectively.

Compared to the shoots, the radish roots had notably greater concentrations of Ag in all treatments (Figure 3.2). The calculated RCF values varied from 0.03 ± 0.03 to 0.29 ± 0.21, suggesting low root uptake of Ag NPs and Ag^+ ions. The calculated TF values ranged from 0.08 ± 0.10 to 0.89 ± 1.21 (Figure 3.3), suggesting low translocation of Ag NPs and Ag^+ ions from the radish roots to shoots. Similarly, Ag was predominantly retained in roots with minor or even no translocation to shoots in previous studies [51, 55]. No significant difference was observed in the RCF and TF values between the $AgNO_3$ and Ag NPs treatments at all biochar amendment rates (Figure 3.3). This is in agreement with previous studies on the uptake of Ag NPs and Ag^+ by tobacco (*Nicotiana tabacum*) [51] and by nine edible plants [144], i.e., the uptake and accumulation of Ag NPs and Ag^+ were equally efficient. However, Rawat et al. [168] reported that the TF value of Cu^{2+} was greater than that of CuO NPs in bell pepper plants, and Yang et al. [146] found that the TF value of Ag^+ was significantly lower than that of Ag NPs in rice plants. In this study, the similar RCF and TF values of Ag NPs and Ag^+ in the radish plants were likely due to their low and comparable concentrations in the soil pore water, limiting bioavailability to the radish plants.

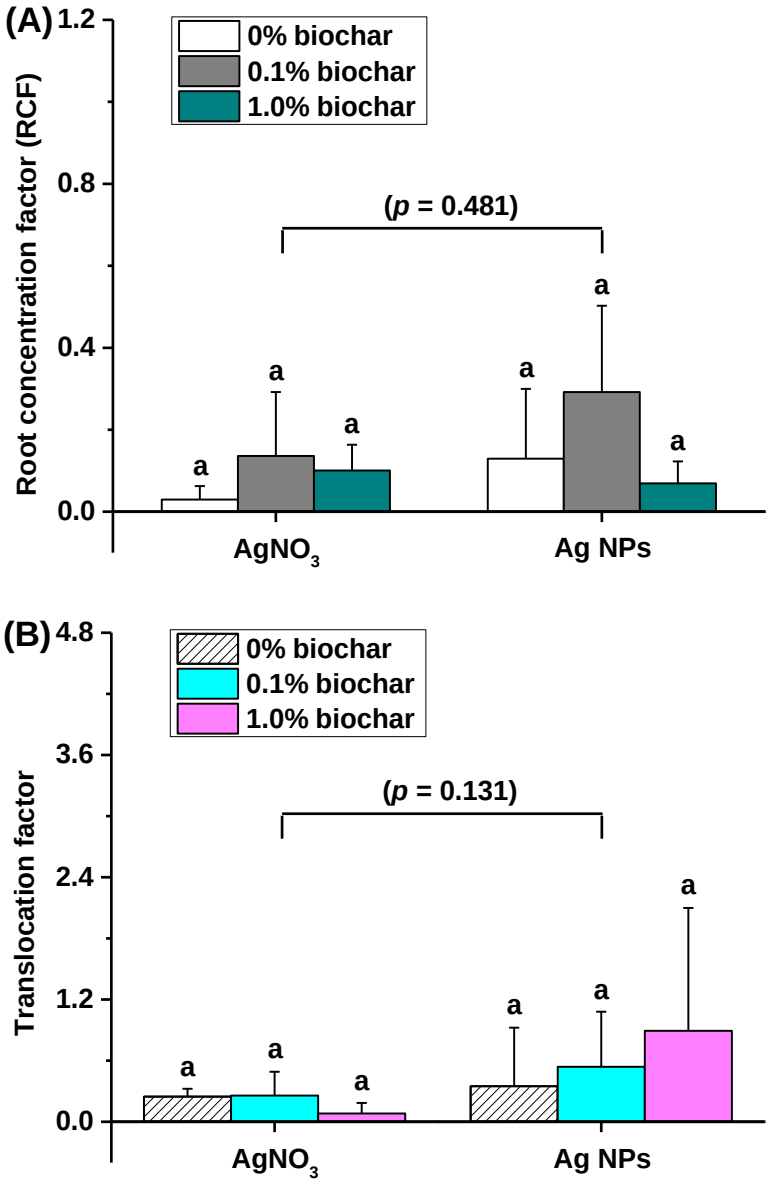

Figure 3.3. Root concentration factor (A) and translocation factor (B) of Ag in either $AgNO_3$ or Ag NPs in radish plants grown in soil pots without (0%) or with (0.1% and 1%) biochar amendment. Error bars are the standard deviations (n = 3). Different letters indicate the significant difference in means at $p < 0.05$. Brackets indicate comparisons between the $AgNO_3$ and Ag NPs treatments.

Ag Sorption to Soils

Figure 3.4 presents the sorption isotherms of Ag NPs and Ag^+ ions by the soil samples without (0%) and with (0.1% and 1.0%) biochar amendment. As summarized in Supplementary Table B1, the Langmuir model fitted the experimental data well with R^2 > 0.95. Biochar amendment (0.1% and 1.0%) had an insignificant influence on Ag sorption by the soils (Figure 3.4). The soil samples had notably higher sorption capacities for Ag^+ than for Ag NPs (Figure 3.4). Likewise, Wang et al. [169] found that the sorption of Ag^+ to ten soils was greater than that for Ag NPs. This is because negatively charged soil particles attract Ag^+ ions but repel negatively charged Ag NPs. Ag NPs in soils (pH of 7.8) would be more negatively charged than the measured zeta potential of −11.2 mV at pH 6.2, because the point of zero charge of Ag NPs is < 2.0 [49] and its surface charge becomes more negative with increasing pH. In fact, sorption of Ag^+ ions correlated with the content of negatively charged soil OM and clay, and sorption of Ag NPs with the level of positively charged iron/aluminum oxide at circumneutral pH [161, 169-172]. Interestingly, for soil with 1.0% biochar the q_{max} values were similar for Ag NPs and Ag^+, but the k_L value for Ag NPs was much lower than for Ag^+. Thus, in that soil sample Ag NPs were more likely to attach to the biochar surface via low-affinity interactions (such as weak attachment due to the second energy minima) [173]. Furthermore, it was reported that metal ions may be reduced after sorption to biochar [72, 174-177]. However, this study was unable to explore the transformation between Ag^+ and Ag^0, i.e., dissolution of Ag NPs to Ag^+ ions and reduction of Ag^+ to Ag^0 by electron-donating moieties (e.g., phenolic moieties) in biochar [175-177]. The Ag transformation should be explored in future studies by employing Fourier transformed infrared spectroscopy (FTIR), X-ray photoelectron spectroscopy (XPS), or X-ray absorption fine structure spectroscopy (XANES). Finally, despite the greater sorption capacity of Ag^+ than Ag NPs to soils with and without biochar, Ag^+ and Ag

NPs uptake was not significantly different (Figure 3.2 and Figure 3.3), which may be explained as follows. Ag sorption capacity is primarily dictated at the high end of Ag concentrations, whereas no substantial difference was observed at low Ag concentration range (Figure 3.4), which is more relevant to the spiked Ag concentration (1 mg kg^{-1}) in soils. In combination with the low Ag concentrations in soil pore water and the low exchangeable Ag fraction, no difference in the uptake of Ag^{+} and Ag NPs is therefore expected.

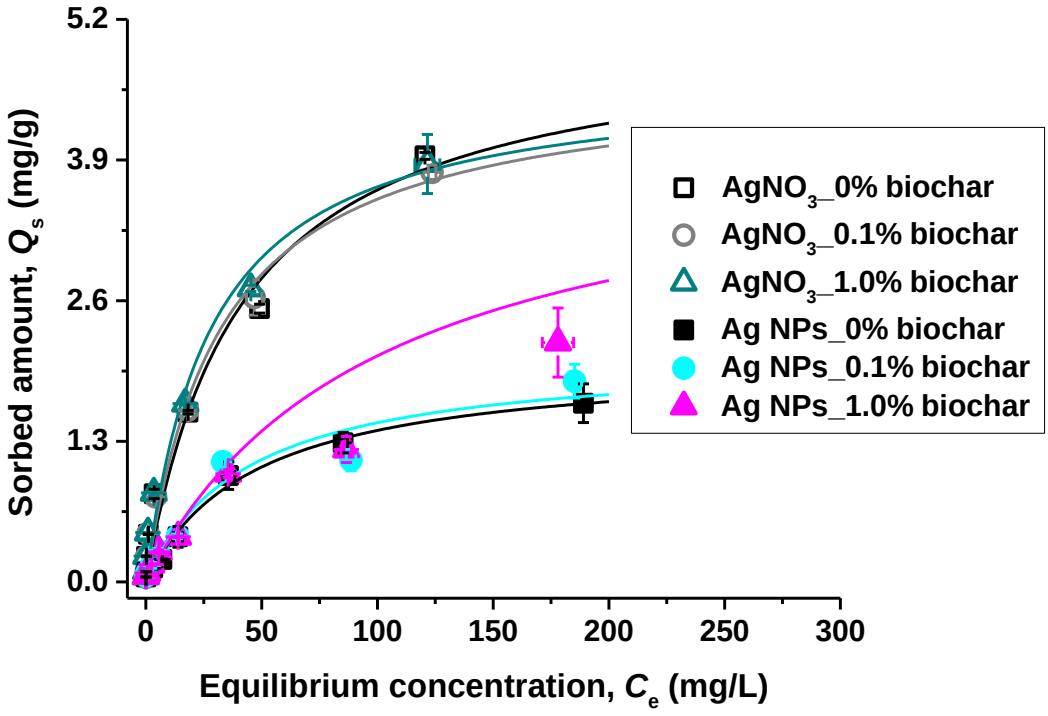

Figure 3.4. Measured (symbols) and fitted (lines) sorption isotherms of Ag in either $AgNO_3$ or Ag NPs by the soil samples without (0%) or with (0.1% and 1%) biochar amendment. Error bars are the standard deviations from two replicates.

Soil-bound Ag Fractions

As shown in Figure 3.5, Supplementary Table B2, and Table B3, the highest proportion of soil background Ag was in the residual fraction bound to silicate minerals (63.9%–76.5%), followed by the OM-bound oxidisable fraction (18.8%–29.5%), Fe/Mn oxide-bound reducible fraction (4.67%–6.45%), and exchangeable fraction (0.08%–0.22%). In comparison, the largest proportion of spiked Ag (> 61.9% for Ag NPs and > 58.3% for Ag^+ ions) was in the reducible fraction, followed by the residual fraction (13.2%–21.5%) ≈ oxidisable fraction (5.1%–23.8%) > exchangeable fraction (0–0.09%), except for radish-growing soil with 1.0% biochar spiked with $AgNO_3$ and the radish-free soil without biochar spiked with Ag NPs. In those two soil samples the residual fraction was the greatest for Ag^+ (45.6%) in the former, and similar to the residual fraction for Ag NPs (41.8%) in the latter. It is plausible that the spiked Ag^+ ions and Ag NPs were associated with the surface of soil Fe/Al oxides and clays [169, 170], which could be readily extracted by hydroxylammonium chloride at pH 2 as the reducible fraction. Our results agree with several earlier studies on other metallic ions and nanoparticles. For example, the majority of Pb was associated with Fe/Mn oxides in soils collected from Guizhou, China [178, 179]. Zhang et al. [151] found that the exchangeable fraction of cerium oxide nanoparticles was the lowest and the residual fraction was dominant in both loamy sand and silty loam soils. Nonetheless, Choleva et al. [157] showed that both Au NPs and ions were predominantly associated with soil OM (the oxidisable fraction) and the reducible fraction bound to metal oxides was minor (<10%).

Compared to the biochar-free treatment, biochar amendment (1.0%) significantly decreased the reducible fraction and increased the residual fraction of Ag^+ ions, but only increased the oxidisable fraction of Ag NPs ($p < 0.05$, Figure 3.5, and Supplementary Table B2) in soils with radish plants. Conversely, without radish plants biochar amendment (1.0%) decreased the

reducible fraction of Ag^+ and the residual fraction of Ag NPs (Figure 3.5 and Supplementary Table B3). It appears that radish plants modulated the changes in the soil-bound fractions of Ag^+ and Ag NPs induced by biochar amendment (1.0%). Biochar addition may increase negatively charged surface sites in soils and release dissolved OM into soil water [180-182], which may scavenge Ag^+ from Fe/Mn oxides and increase repulsion between Ag NPs and silicate minerals, leading to decreased reducible and residual fractions of Ag^+ and Ag NPs, respectively. Furthermore, radish root exudates (including organic acids, carbohydrates, and root mucilage) may also facilitate the release of Ag^+ from Fe/Mn oxides via complexation with Ag^+, or the release of Ag NPs from the residual fraction in the rhizosphere soil [145, 147].

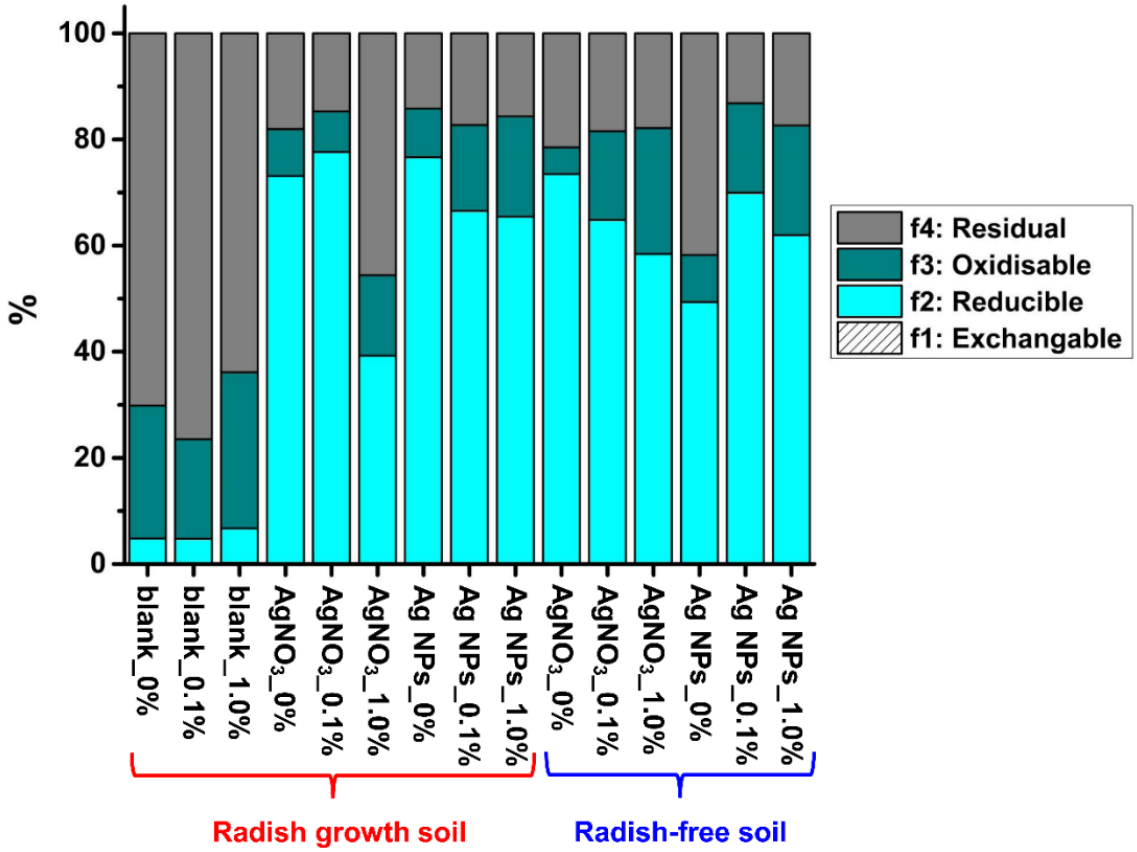

Figure 3.5. Soil-bound fractions of Ag in either $AgNO_3$ or Ag NPs in the soil samples without (0%) or with (0.1% and 1%) biochar amendment measured by the BCR extraction method.

Finally, the exchangeable fraction of Ag was very low for all treatments (Figure 3.5, Supplementary Table B2, and Table B3). The Ag concentration for all extracted pore water samples was below the AAS limit of detection (< 0.5 μg L^{-1}). This low Ag concentration in soil pore water was expected, as Ag NPs and Ag^+ ions can be transformed to Ag_2S [152], which has very lower solubility ($K_{sp} = 5.9 \times 10^{-51}$) in water. Ag was still detected in the radish plants, especially in the roots (Figure 3.2A), suggesting that the radish plants could take up the trace level of Ag in soil pore water. It is thought that fast exchange reactions may occur between the reactive (e.g., reducible and oxidisable) and available (i.e., exchangeable) pools [183], thus both the reactive and available fractions are potentially bioavailable to plants [151, 155, 156]. The combined reducible and oxidisable fractions accounted for 54.4%–86.7% of total Ag in the soil samples, which was potentially bioavailable to the radish plants over time. The release of plant root exudates might also slowly release Ag from the reducible and oxidisable fractions into the exchangeable fraction, and thus continuously supply a trace level of Ag in soil pore water for root uptake. Since the soil-bound fractions of Ag measured by the BCR method could only represent the maximum potential bioavailability, correlation of Ag uptake and accumulation with specific fractions may be difficult to achieve, especially at environmentally-relevant concentrations [184, 185].

Conclusion

This study has several important findings that are relevant to assessing the risks of Ag NPs to food safety, and the effect of biochar amendment on Ag fractions and plant uptake of Ag NPs and Ag^+ ions in soils. Biochar amendment significantly changed the soil-bound fractions of Ag NPs and Ag^+ ions, as modulated by the radish plants. In any case, the readily bioavailable fraction (i.e., the exchangeable fraction) was very low. Thus, plant uptake of Ag at environmentally relevant concentrations is predominantly controlled by low uptake from soil pore water and a

continuous supply of Ag from the reactive fractions. Additionally, at the low Ag level the biochar amendment primarily changed the reducible, oxidisable and residual fractions, suggesting a long-term effect on mass transfer between various soil-bound Ag fractions and subsequent uptake of Ag by plants, which may be different from results at high Ag levels. In contrast to previous studies using unrealistic high concentrations of Ag NPs [52, 54-57], this short-term study (35 days) showed that Ag uptake and accumulation in food crops will be low at environmentally-relevant concentrations. This study was limited in that only one Ag concentration (1 mg kg^{-1}), one crop (radish) and one soil type were used, and molecular Ag species were not differentiated. Future work should use other advanced analytical techniques (e.g., FTIR, XPS, XANES, and single particle inductively coupled plasma mass spectrometry) to speciate the bioavailable fractions of Ag NPs and Ag^{+} in diverse soil, water, and plant systems.

Author Contribution: Jianzhou He, Yuanbo Li, and Wei Zhang conceived and designed the research experiments; Jianzhou He, Yuanbo Li, and Haonan Qi conducted the experiments; Jianzhou He and Haonan Qi analyzed the samples for Ag; Jianzhou He analyzed the data and wrote the manuscript; Hui L and Wei Zhang reviewed and edited the manuscript.

CHAPTER IV

STOMATA FACILITATE FOLIAR SORPTION OF SILVER NANOPARTICLES BY *ARABIDOPSIS THALIANA*

Abstract

Application of nanopesticides may substantially increase the uptake and accumulation of engineered nanomaterials (ENMs) in food crops. However, mechanisms for internalization of ENMs into plant leaves are unclear. This study investigated the role of stomata in the internalization of silver nanoparticles (Ag NPs) using abscisic acid (ABA)-responsive ecotypes (Landsberg erecta [Ler] and Col-7) and ABA-insensitive mutants (*ost1-2* and *scord7*) of *Arabidopsis thaliana* in batch sorption experiments, in combination with microscopic visualization. Compared with those of the ABA-free control, stomatal apertures were significantly lower for the Ler and Col-7 ecotypes ($p < 0.05$) but remained unchanged for the *ost1-2* and *scord7* mutants, after exposure to 10-μM ABA for 1 h. Sorption kinetics showed that the maximum sorption of Ag NPs was achieved after 60 min of equilibration. The amount of Ag NPs sorbed by the leaves of Ler and Col-7 ecotypes treated with 10 μM ABA was much lower than that in the ABA-free control, mainly due to ABA-induced stomatal closure. In contrast there was no significant difference in foliar sorption of Ag NPs by the *ost1-2* and *scord7* mutants with and without ABA. Ag NPs were widely attached to the *Arabidopsis* leaf surface, and localized at the cell membrane, cytoplasm and plasmodesmata, as revealed by scanning electron microscopy and transmission electron microscopy, respectively. These results highlight the important role of stomata in the internationalization of ENMs in plants and may have broader implications in foliar application of nanopesticides and minimizing contamination of food crops by ENMs.

Introduction

Nanotechnology has been strongly advocated for improving agricultural productivity and sustainability through optimization of agrochemical applications (e.g., nanofertilizers, nanopesticides, and controlled release), delivery of genetic materials, and intelligent surveillance of plant disease [186-188]. Specifically, the development of nanopesticides has drawn immense attention from scientific communities and agrochemical companies. For example, due to its antimicrobial and insecticidal properties [189], silver nanoparticles (Ag NPs) have been used in > 100 pesticides registered in the last decade [75-77]. The rapidly growing use of nano-enabled products in agriculture will exacerbate the release of engineered nanomaterials (ENMs) into soil and water systems [42, 47, 190], which is estimated to be much higher than the combined release from all other sources [76]. Thus, there is an increasing concern over the risks of nanopesticides (such as Ag NPs) used on food crops. It is important to study the transfer and internalization of ENMs to food crops due to potential human exposure and food safety risks.

Crop plants are prone to elevated exposure of ENMs from plant protection and fertilizer products, crop irrigation with reclaimed water, biosolid application, and atmospheric deposition [48, 76], leading to the uptake and accumulation of ENMs in plants [48, 49, 65, 191, 192]. As a result, the human population may be exposed to ENMs via consumption of food crops [65, 192-194]. Root uptake of ENMs has been well studied [50, 52, 57, 64, 66, 67, 146, 148, 195, 196], with ENMs taken up via the apoplastic and symplastic pathways and transported to aerial portions through the vascular system [65]. Moreover, the size exclusion limit of the root membrane [62-66] may be overcome by endocytosis [62, 68, 69] and additional entry points coming from physical and disease damage to roots as well as emergence of new secondary roots [64, 66].

In contrast, studies on foliar uptake of ENMs have been limited [49, 82, 197, 198]. It is thought that ENMs may first attach to the leaf surface and then penetrate the waxy cuticle and/or stomata on the epidermis [66, 199]. However, most ENMs are not small enough to pass through the small pores (< 5 nm) in the cuticle [200]. Rather they may enter through stomata where the opening size is in micrometers [49, 199, 201-203]. Previous studies have speculated that plant stomata could serve as points of entry for ENMs [82, 197]. For example, Ce was detected in the leaf, flower, stem, and root of cucumber (*Cucumis sativus*) after foliar exposure to aerosol and aquasol of cerium dioxide nanoparticles (CeO_2 NPs), indicating uptake through the leaves and further translocation to other plant parts [204]. Larue et al. [49, 198] conjectured that Ag NPs and TiO_2 nanoparticles may be internalized into lettuce leaves via stomata after foliar exposure. However, Birbaum et al. [205] exposed maize leaves to CeO_2 NPs aerosol or aquasol, and found that the sorbed amount (50 μg Ce g^{-1} leave) was independent of stomatal opening or closure. Although previous researchers have hypothesized the potential uptake of ENMs through stomatal openings, no study has directly shown the differential internalization of ENMs by plant leaves when stomata are manipulated under otherwise similar experimental conditions.

For this purpose, regulation of stomatal closure by the plant hormone abscisic acid (ABA) and related signal transductions [206] may be harnessed to elucidate the role of stomata in the internalization of ENMs using ABA-responsive plant ecotypes and ABA-insensitive mutants. The ABA-insensitive plant mutants are best characterized in *Arabidopsis thaliana* [207, 208]. It was shown that the *ost1-2* and *scord7* mutants of *Arabidopsis* do not respond to ABA-induced stomatal closure and exhibit constitutively larger apertures [206, 209]. Also *Arabidopsis thaliana* was frequently chosen as the model plant in plant biology and nanotoxicity studies [65, 148, 206, 209-211] because findings from *Arabidopsis* are generally applicable to other plant species [68].

Therefore, this study aimed to investigate the role of stomata in the sorption (including surface attachment and internalization) of Ag NPs to plant leaves using the model plant *Arabidopsis thaliana*. The ABA-responsive ecotypes of *Arabidopsis thaliana* (i.e., Landsberg *erecta* [Ler] and Col-7) and their corresponding ABA-insensitive mutants (i.e., *ost1-2* and *scord7* for Ler and Col-7, respectively) were used to assess the role of stomata in the internalization of Ag NPs through batch sorption experiments combined with confocal laser scanning microscopy (CLSM), scanning electron microscopy (SEM) with energy dispersive spectrometer (EDS), and transmission electron microscopy (TEM). We hypothesized that the sorption of Ag NPs with ABA treatment would be lower than that without ABA for the Ler and Col-7 ecotypes, but similar for the *ost1-2* and *scord7* mutants. This study provided direct evidence on the internalization of Ag NPs through stomatal entry.

Materials and Methods

Plant Materials

Seeds of the Ler, Col-7, *ost1-2*, and *scord7* were sterilized in 70% ethanol for 10 min and in 50% bleach for 5 min, respectively, washed three times with autoclaved deionized (DI) water, and then dispersed into 0.2% agar before sowing. The seeds were directly sown in sterilized *Arabidopsis*-growth mix packed in nursery pots (equal parts of Suremix, medium vermiculate and perlite) [212], placed in a tray, and grown in a growth chamber that was well-maintained at 22 ºC with a 12/12 h photoperiod under a light intensity of 100 µE/m^2/s. The plants were watered three times a week with one-half strength Hoagland solution to maintain a water height of 1 cm above the bottom of the tray. Fully expanded leaves from 5-week-old plants were used for all experiments.

Ag NPs Suspension

A stock suspension of Ag NPs (1000 mg/L) stabilized with polyvinylpyrrolidone (PVP, 0.6% in solution) was purchased from the US Research Nanomaterials, Inc. (Texas, US). The stock solution was filtered with Amicon Ultra-10kDa filters (Millipore, US) to remove free PVP from the solution. The retained Ag NPs were then washed repeatedly and dispersed in DI water to obtain the working suspension (Supplementary Text C1 in Appendix C). The working suspension of Ag NPs was ultrasonicated (Fisher Scientific, FS20) for 5 min before use. The morphology and size of Ag NPs was characterized by transmission electron microscopy (TEM, JEOL 2200FS, Japan), and its size and zeta (ζ) potential by a Zetasizer Nano-ZS (Malvern Instruments, UK). Detailed information on sample preparation and characterization can be found in Supplementary Text C2.

Stomata Assays

Leaf discs (~ 3 mm × 3 mm) were cut from the leaves of the 5-week-old mature plants with a scalpel and immersed in lidded 6-well plates containing opening buffer (25 mM MES and 10 mM KCl, pH 6.15) without (the control treatment) or with 10 µM ABA (the 10 µM ABA treatment). To preserve the stomatal aperture status in *Arabidopsis* plants, the leaves were not further treated with any other stomatal opening buffer. The plates were cultured in the growth chamber for 1 h before observation with CLSM. CLSM images were taken at an excitation wavelength of 488 nm and emission wavelengths of 505-525 nm in a field of view of 318.2 µm. Briefly, the discs were placed on glass microscope slides, and then scanned to a depth of ~10 µm using an Olympus FluoView 1000 CLSM at three random locations to generate Z-scans. The Z-scans were stacked to produce images of the leaf surface for stomata analysis. Three discs from each treatment were used and three locations per disc were imaged by CLSM. The width of the stomatal aperture was measured using software ImageJ from 36–63 stomata in each treatment, and

the width-to-length ratio of the stomatal aperture was similarly measured on 36–84 stomata per treatment.

Sorption Experiments

Batch experiments were conducted to investigate the sorption of Ag NPs by whole *Arabidopsis thaliana* leaves treated with the opening buffer without (the control treatment) or with 10 μM ABA (the 10 μM ABA treatment). First, the kinetic sorption experiment was performed to estimate the time to reach sorption equilibration. Briefly, about 0.45 g of whole *scord7* leaves from the control treatment were immersed in an Ag NP suspension of 2 mg L^{-1} (pH 6.5) up to 120 min. For the equilibrium sorption experiments, about 0.45 g of whole leaves (i.e., Ler, Col-7, *ost1-2* and *scord7*) were placed in 60-mL glass jars each containing 25 mL of Ag NPs solution at three concentrations of 1, 5, and 10 mg L^{-1}. The blank experiment was performed using DI water without Ag NPs. The mixture of leaves and Ag NPs was equilibrated at room temperature in a horizontal shaker (160 rpm) for predetermined 60 min. Afterwards, the leaves were separated from the solution using a tweezer. The final concentration of Ag NPs in the remaining suspension was determined using an atomic absorption spectroscope (AAS, AAnalyst 400, PerkinElmer) after nitric acid digestion.

Data Analysis

The sorbed concentration of Ag NPs to the leaves was calculated by the difference between the initial and final concentrations of Ag NPs using Eq. (4.1):

$$Q_e = (C_o - C_e)\frac{V}{m} \quad (4.1)$$

where Q_e is the sorbed concentration of Ag NPs to the leaves (mg kg^{-1}), C_o and C_e are the initial and equilibrium concentrations of Ag NPs in the suspension (mg L^{-1}), respectively, V is the

volume of the suspension (mL), and m is the fresh weight of leaves (g). All sorption experiments were conducted in at least duplicate.

One-way ANOVA analysis was performed to identify statistically significant differences in measured parameters using the least significant difference (LSD) test. All statistical analyses were conducted using SPSS 22.0 software for Windows (IBM Corp., Armonk, NY), with the differences of means considered significant at $p < 0.05$.

Visualization of Sorbed Ag NPs

To determine the localization of Ag NPs in *Arabidopsis thaliana* leaves, Col-7 and *scord7* leaves were prepared for microscopic observation after exposure to 10 mg L^{-1} of Ag NPs. For SEM the leaves were freeze-dried (Electron Microscopy Sciences, Model EMS750X, Hatfield, PA) and mounted on aluminum stubs using High vacuum carbon tabs (SPI Supplies, West Chester, PA). The samples were coated with ~5 nm-thick osmium using an NEOC-AT osmium chemical vapor deposition coater (Meiwafosis Co., Ltd., Osaka, Japan) before examination with a JEOL 7500F SEM (JEOL Ltd., Tokyo, Japan) equipped with energy dispersive X-ray spectroscopy (Oxford Instruments, High Wycomb, Bucks, England).

TEM sample preparation followed a standard procedure as previously described [143, 146]. Briefly, the leaves were cut into small pieces, which were then prefixed in 2.5% glutaraldehyde and 2% paraformaldehyde for 24 h, washed three times (20 min/each) with 0.1 M cacodylate buffer (pH 7.4), and post-fixed in 1% osmium tetroxide for 2 h. After again rinsing three times (20 min/each) in 0.1 M cacodylate buffer (pH 7.4), the specimens were dehydrated in an acetone series (30%, 50%, 70%,80%, 90%, 95%, and 100%), with each step maintained for 30 min. Afterwards, specimens were sequentially infiltrated in different mixtures of acetone and Spurr resin (ratio = 3:1, 2:2, 1:3, and 0:1) and finally embedded in silicone molds. The polymerization was performed

at 60 °C for 48 h. The prepared specimens in Spurr resin were sectioned (70 nm thickness) using a PowerTome XL ultramicrotome (RMC Boeckeler, US) equipped with a diamond knife. The ultra-thin sections were placed on 200-mesh copper grids and then imaged with a JEOL 1400 TEM at an accelerating voltage of 100 kV. Our preliminary tests showed that sample staining with uranyl acetate and lead citrate introduced numerous black spots that interfered with the identification of Ag NPs. Therefore, the specimen was not stained.

Results and Discussion

Ag NPs Characterization

As shown in Figure 4.1, the primary particles of Ag NPs were near-spherical in shape with an average diameter of 20.9 nm. The Ag NP suspension had a negative ζ potential of –31.1 mV, a hydrodynamic diameter (D_h) of 36.1 nm for the Ag NP aggregates, and a polydispersity index of 0.24. The D_h value of the Ag NP aggregates was about twice that of the primary particle size measured by the TEM, probably due to slight aggregation of Ag NPs in suspension. The time-resolved D_h measurements indicated that Ag NPs were stable at pH 6.5 in DI water over 3 h.

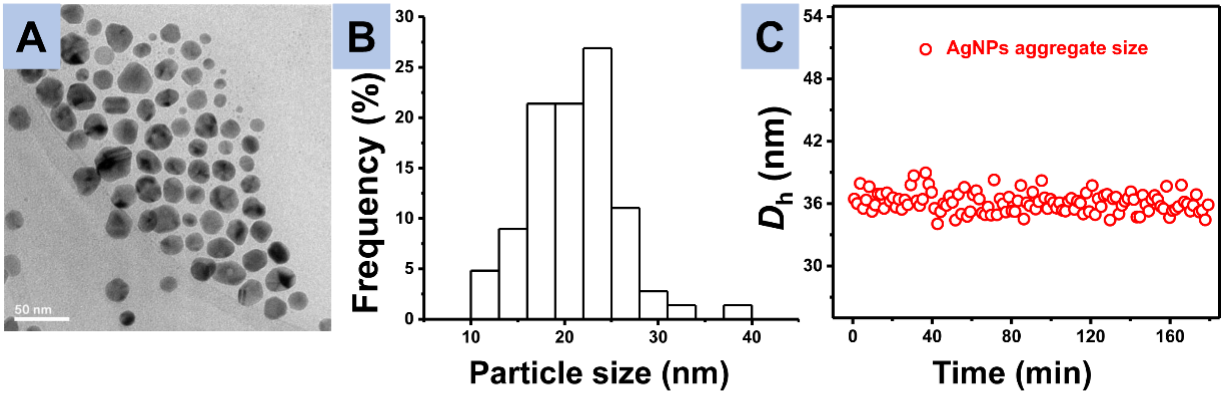

D

TEM size (nm)	D_h (nm)	Polydispersity index	ζ potential (mV)
20.9 ± 4.7	36.1 ± 1.0	0.24 ± 0.03	–31.1 ± 2.2

Figure 4.1. Representative TEM image of Ag NPs (A), particle size distribution of Ag NPs measured from the TEM images (B), aggregation kinetics of 10 mg L^{-1} Ag NPs suspension at pH 6.5 in DI water (C), and summarized TEM primary particle size, hydrodynamic diameter (D_h) and ζ-potential of Ag NPs (D).

Stomatal Aperture Assay

The stomatal apertures for the different genotypes of *Arabidopsis thaliana* are presented in Figure 4.2, Supplementary Table C1, Figure C1, and Figure C2. As shown in the CLSM images (Figure C1), ABA (10 µM) induced normal stomata closure for the Ler and Col-7 ecotypes, but the stomata for the ABA-insensitive mutants (*ost1-2* and *scord7*) failed to close. This observation was expected as the stomata of the ecotypes would respond to the regulation of ABA, but those of the mutants would be insensitive to ABA [209]. The width of the stomatal aperture measured using ImageJ decreased from 4.03 ± 0.72 µm and 4.45 ± 0.66 µm in the control treatment to 2.62 ± 0.89 µm and 2.58 ± 0.85 µm in the presence of 10 µM ABA for the Ler and Col-7 ecotypes, respectively ($p < 0.05$, Figure 4.2 and Table C1). However, the stomatal width of the *ost1-2* and *scord7* mutants remained statistically unchanged after ABA exposure. It is worth noting that the exposure to 10 µM ABA did not fully close the stomata of the Ler and Col-7 ecotypes (Figure 4.2, Supplementary Table C1, Figure C1, and Figure C2), which is consistent with previous observations on partial stomatal closure of Col-0 and Col-7 in response to ABA [206, 209]. The measured stomatal width-to-length ratios similarly demonstrated the lower stomatal aperture in the presence of 10 µM ABA than that without ABA for the Ler and Col-7 ecotypes, but the non-response of the *ost1-2* and *scord7* mutants to the ABA treatment (Supplementary Table C1 and Figure C2).

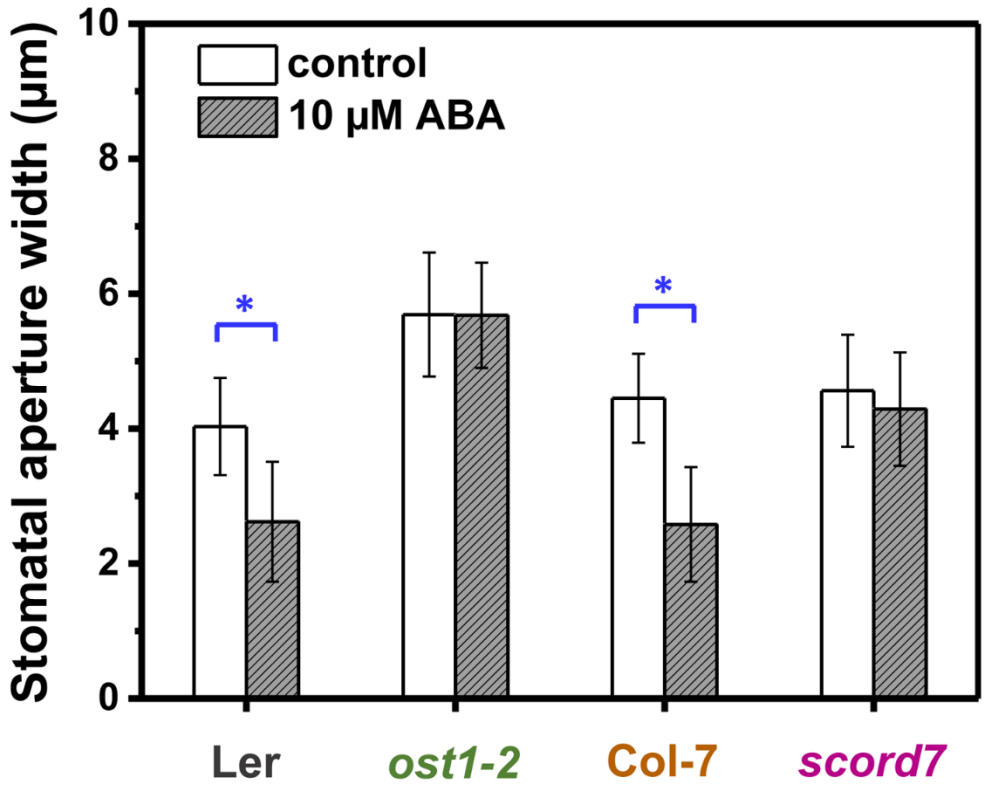

Figure 4.2. Stomatal aperture width of *Arabidopsis thaliana* treated with opening buffer in the absence (control) or presence of 10 µM abscisic acid (ABA). Ler and Col-7 are ecotypes, and *ost1-2* and *scord7* are corresponding ABA-insensitive mutants. Results are shown as mean ± standard deviation (n = 36–63 stomata). Symbol (*) indicates a statistically significant difference in means between the control and 10 µM ABA treatments ($p < 0.05$).

Kinetics and Equilibrium Sorption of Ag NPs

As shown in Supplementary Figure C3, sorption of Ag NPs to the *scord7* leaves increased rapidly at the beginning and then reached the maximum by about 60 min. This was much shorter than the equilibrium time (14 h) used in the previous sorption experiment of Ag NPs by the leaf discs (diameter of 4 mm) of ficus tree (*Ficus benjamina*) [213]. The equilibrium sorption amounts of Ag NPs to *Arabidopsis* leaves were shown in Figure 4.3. As expected, the treatment of 10 μM ABA for 1 h significantly decreased the sorbed amount of Ag NPs by the Ler and Col-7 ecotypes at all exposure concentrations ($p < 0.05$, Figure 4.3a and c) except for Col-7 at 10 mg L^{-1} of Ag NPs (Figure 4.3c), but did not change the sorption of Ag NPs by the *ost1-2* and *scord7* mutants (Figure 4.3b and d). Compared to the control treatments, the mean sorbed Ag NPs decreased by 85.8%, 23.0%, and 62.8% for the Ler and 14.2%, 21.3% and 16.9% (statistically non-significant) for the Col-7 at 1, 5, and 10 mg L^{-1} Ag NP in the presence of 10 μM ABA, respectively. This is mainly due to the different stomatal responses to ABA between the *Arabidopsis* ecotypes and mutants [207, 208]. The presence of ABA (10 μM) triggered stomatal closure in the Ler and Col-7 ecotypes and led to smaller stomatal apertures than those of the control treatments (Figure 4.2), resulting in decreased sorption of Ag NPs (Figure 4.3). In contrast, the stomata of *ost1-2* and *scord7* remained open in the presence of ABA (Figure 4.2) [206, 209], resulting in no difference in the amount of sorbed Ag NPs between treatments with and without ABA. It is unclear why the extent of decrease in the sorption of Ag NPs upon exposure to ABA was less for the Col-7 than for the Ler. Nonetheless, there was no statistical difference between the control and ABA treatments for the Col-7 at 10 mg L^{-1} Ag NPs (Figure 4.3c), which may need more replications to determine any statistical difference.

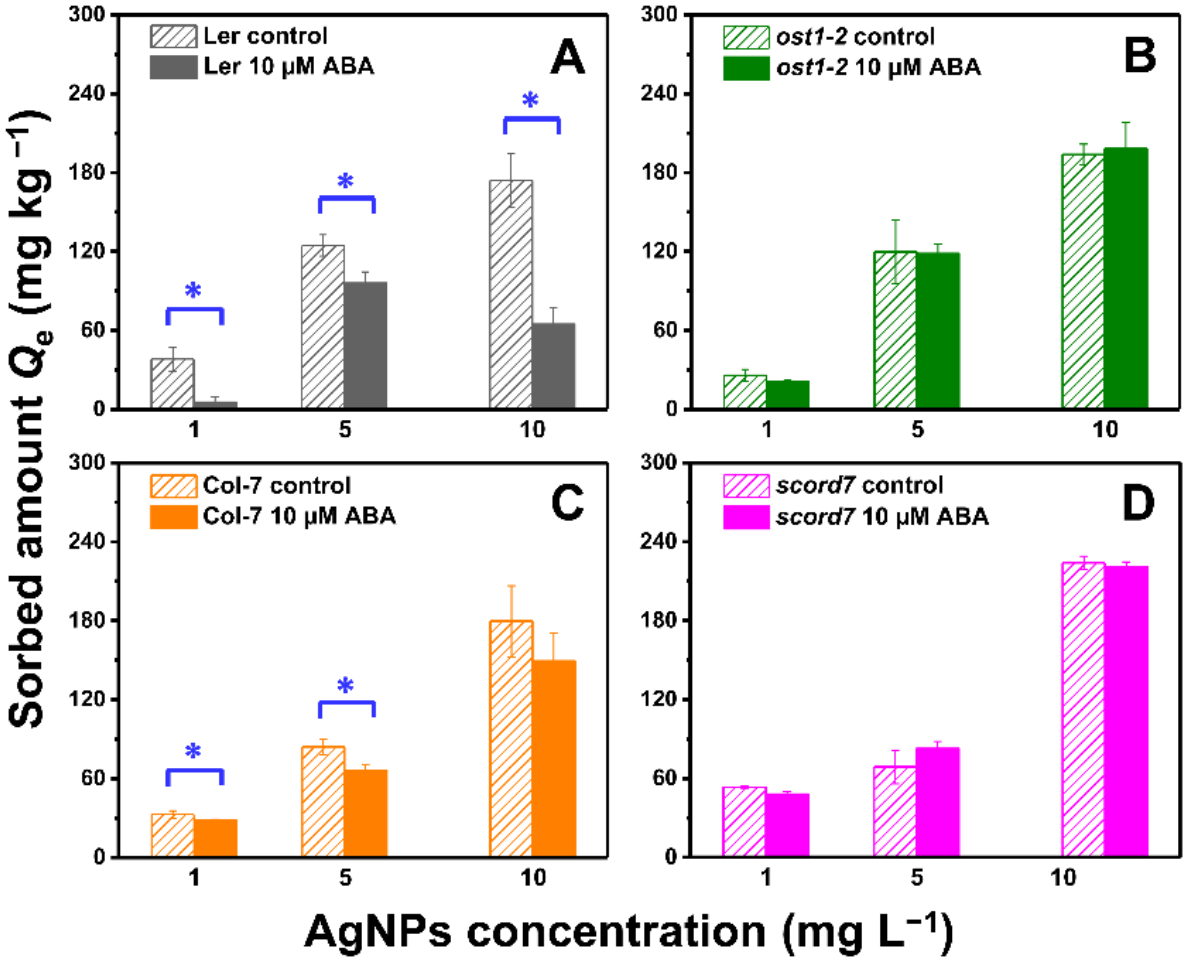

Figure 4.3. Sorbed amount of Ag NPs at various concentrations of 1, 5, and 10 mg L^{-1} by the leaves of *Arabidopsis thaliana* Ler (A), *ost1-2* (B), Col-7 (C), and *scord7* (D) treated in opening buffer without (control) or with abscisic acid (10 µM ABA) for 1 h. Error bars represent the standard deviations (n = 3). Symbol (*) indicates statistically significant difference in means between the control and 10 µM ABA treatment ($p < 0.05$).

The reduction of sorbed Ag NPs correlated with the change in stomatal aperture induced by the presence of 10 μM ABA (Figure 4.4). The data points were distributed along the 1:1 line, indicating that the decreased amount of Ag NPs sorbed by *Arabidopsis* leaves was directly due to the decreased stomatal aperture (Figure 4.2). Again, decreased Ag NPs sorption from stomata closure was more pronounced for the Ler than the Col-7 (Figure 4.4). By using the ABA-responsible *Arabidopsis* ecotypes and ABA-insensitive mutants this study provides compelling evidence that stomata facilitate the internalization of Ag NPs into plant leaves, which supports previous findings on Ag NPs and other ENMs (e.g., CeO_2, TiO_2, and Au) [49, 68, 143, 205, 214]. For example, a recent study examining the translocation of CeO_2 NPs applied to cucumber leaves suggested that small CeO_2 NPs can penetrate the leaf through hydathodes and stomata [204]. It is worth mentioning that after penetrating the wax cuticle and leaf epidermis, ENMs can easily access the downward phloem vascular system and be transported to other parts of the plant [66, 203, 215, 216]. Thus, stomata-facilitated internalization of ENMs could be an important route for plant uptake of ENMs.

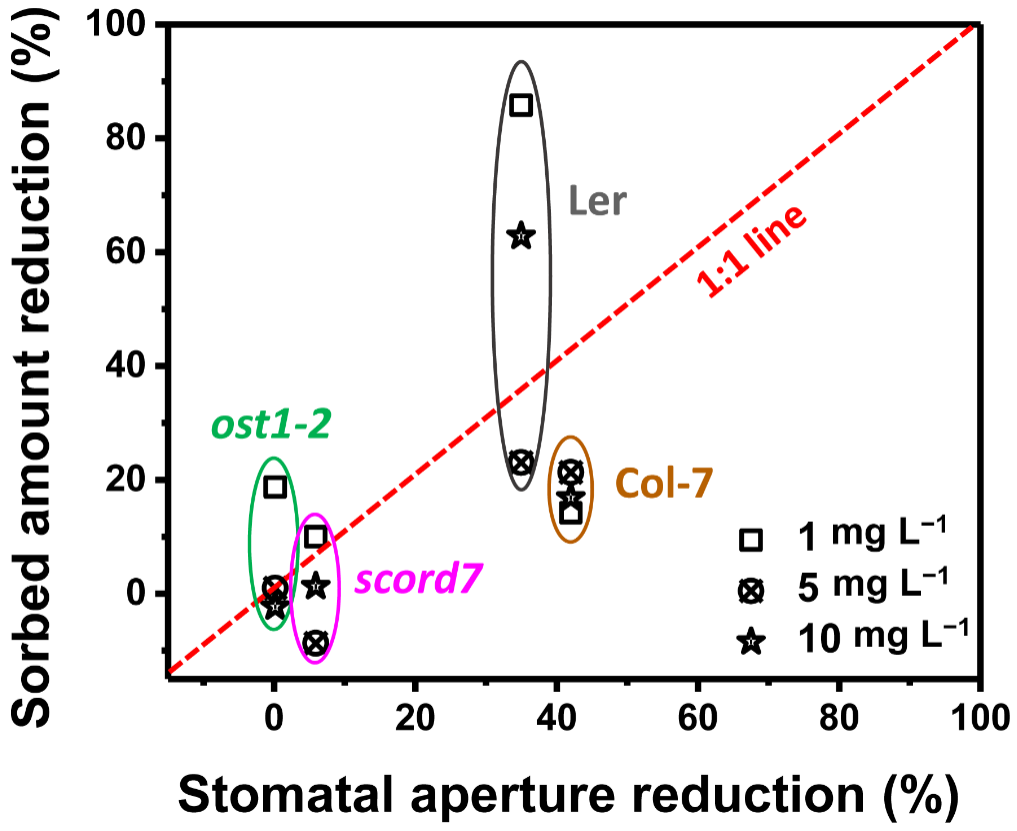

Figure 4.4. Relation between the reduction percentages of the sorbed Ag NPs and the change of stomatal aperture induced by the presence of 10 µM ABA. For each *Arabidopsis* genotype, the sorbed amount reduction (%) was calculated for 1, 5, and 10 mg L^{-1} of the Ag NPs exposure.

Visualization of Sorbed Ag NPs

Surface-attached and internalized Ag NPs were characterized for the leaves of *Arabidopsis* Col-7 ecotype and the *scord7* mutant by SEM-EDS and TEM, as shown in Figure 4.5, and Supplementary Figures C4, C5, and C6 in Appendix C. No silver was detected in the SEM (Figure C4a and d) for the blank (i.e., no Ag NPs exposure). However, bright dots were clearly observed on the surface of Col-7 leaves in the control and 10 µM ABA treatments (Supplementary Figure C4b and c), which was verified as elemental Ag by the EDS spectra (Supplementary Figure C4e and f). Ag was distributed randomly and widely on the Col-7 leaf surface (Supplementary Figure C5). It is interesting to note that more Ag NPs were found on the leaf surface in the presence of 10 µM ABA (Supplementary Figure C4c), likely because the closure of stomata decreased the internalization of Ag NPs and consequently increased the amount of Ag NPs available for surface attachment. It is reported that surface roughness facilitates the deposition of ENMs [217, 218]. However, since the SEM-imaged areas were near stomata and other surface structures were not well resolved, the distribution pattern of attached Ag NPs could not be discerned on certain structural features of the *Arabidopsis* leaves, such as grooves and veins with high roughness [219].

Ag NPs were localized subcellularly in the Col-7 and *scord7* leaves for the control and 10 µM ABA treatments (Figure 4.5, Supplementary Figure C6 and Figure C7). The TEM images of chloroplast appeared to have black spots (such as plastoglobuli) found in all treatments (Figure C6), which obscured any possible identification of Ag NPs. Thus, we focused on other subcellular locations. As shown in Figure 4.5, for the *scord7* leaves, Ag NPs internalized through the stomatal openings were found in the cytoplasm (Figure 4.5c, d and e), attached to the cell membrane (Figure 4.5f), and near or entrapped within the plasmodesma (Figure 4.5c). Similarly, Ag NPs were also found at the cell membrane, and near or within the plasmodesma in the Col-7 leaves in the control

treatment (Figure C7). Our observation is consistent with earlier studies documenting that Ag NPs were detected in the parenchyma cells of lettuce leaves [49] and associated with the cell walls in soybean and rice leaves [143] after foliar exposure. The role of plasmodesma as a conduit for inter-cellular transfer (Figure 4.5c and Figure C7c–e) has previously been reported. Indeed, gold nanoparticles (15 nm) and Ag NPs (20 nm) were accumulated in the plasmodesmata of the roots of woody poplar [220] and *Arabidopsis thaliana* [148], respectively. Clearly, plasmodesma is sufficiently large (20–50 nm) [221] to allow passage of Ag NPs measuring 20.9 nm in diameter from one cell to another, leading to entry into the symplastic pathway. In addition to these subcellular locations discussed above, polystyrene particles were found to accumulate in the guard cells of *Vicia faba* leaves [82]. Kurepa et al. [68] further revealed that TiO_2 Alizarin red S nanoconjugates were enclosed in the vacuoles of stomatal guard cells in *Arabidopsis thaliana*. Finally, the internalized Ag NPs existed as single particles or aggregate clusters in the *Arabidopsis* leaves (Figure 4.5 and Figure C7). Nonetheless, our work was conducted *in vitro* in a relatively short time frame (1 h sorption experiment) and could not reveal *in-situ* transformation of Ag NPs. *In vivo* studies over longer time showed that Ag NPs could be oxidized or dissolved, and Ag^+ ions could complex with glutathione [49], or be reduced to ^0Ag [143, 222].

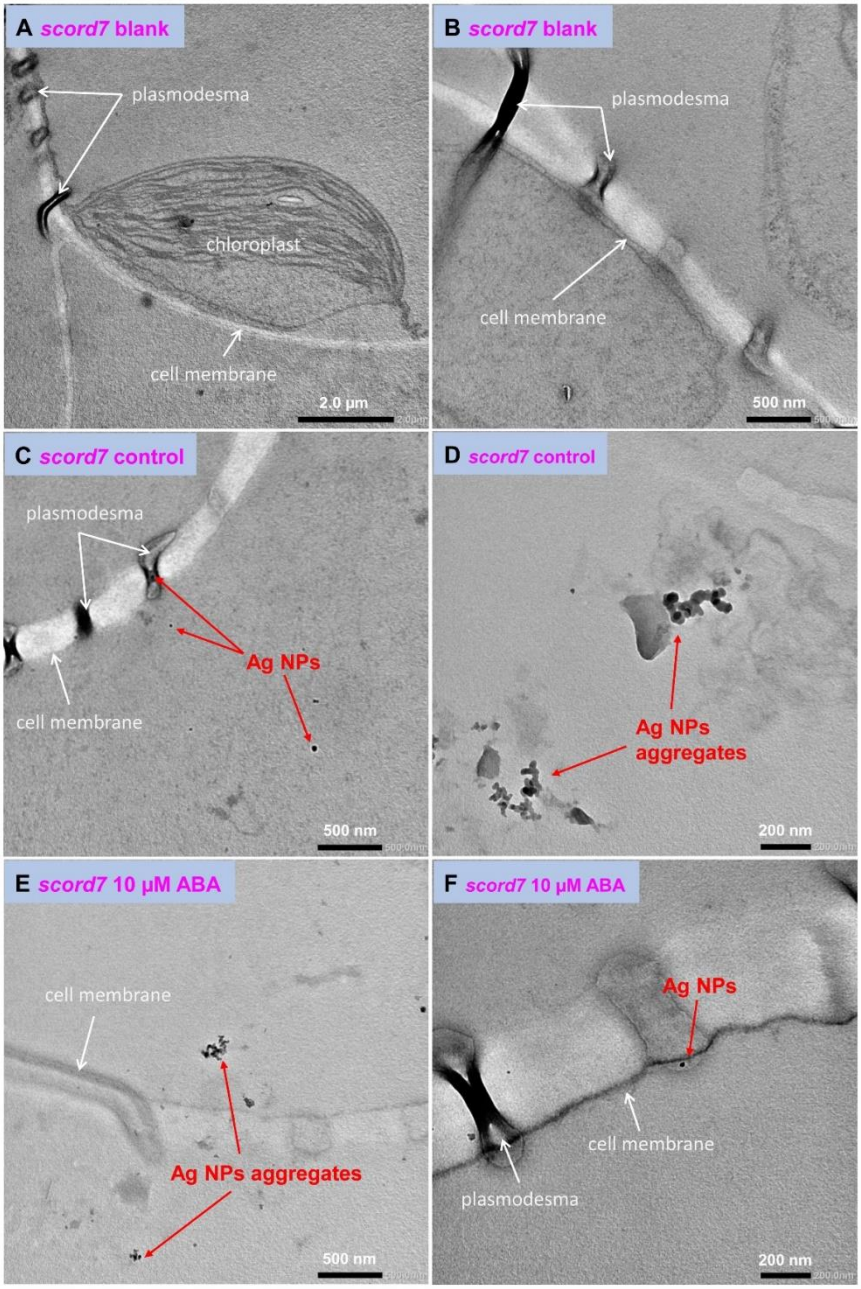

Figure 4.5. Representative TEM images of Ag NPs in the leaves of *Arabidopsis scord7* mutant after the sorption experiment (10 mg L^{-1} Ag NPs). Blank: no Ag NPs exposure; Control: opening buffer without abscisic acid (ABA) treatment for 1 h before 10 mg L^{-1} Ag NPs exposure; 10 µM ABA: opening buffer with 10 µM ABA treatment for 1 h before 10 mg L^{-1} Ag NPs exposure. Red arrows indicate the spots of Ag NPs at the subcellular locations.

Conclusion

The highlight of this study was the use of the ABA-responsive *Arabidopsis* ecotypes (i.e., Ler and Col-7) and the ABA-insensitive mutants (i.e., *ost1-2* and *scord7*) to investigate the role of stomata in the internalization of Ag NPs. The sorbed amount of Ag NPs by the leaves positively correlated with the stomatal aperture, that is, when ABA triggered stomatal closure in the Ler and Col-7 ecotypes, the amount of Ag NPs sorbed to the *Arabidopsis* leaves decreased. In contrast, no difference in Ag NPs sorption was observed for the *ost1-2* and *scord7* leaves with or without ABA due to similar stomata apertures. The internalized Ag NPs were associated with the cell membrane, cytoplasm and plasmodesmata of the leaves. Since internalized ENMs cannot be removed by washing, future studies are needed to investigate the risks associated with human consumption of ENMs-contaminated crop plants and fresh produce through foliar inputs. Furthermore, the important role of stomata in internalization of Ag NPs also has implications for the delivery of pesticides, nutrients, and other active ingredients by ENMs via the stomata pathway.

Author Contribution: Jianzhou He and Wei Zhang conceived and designed the research experiments; Jianzhou He conducted the experiments and performed sample analysis, analyzed the data, and wrote the manuscript; Li Zhang provided assistance on the *Arabidopsis* growth and the CLSM measurements; Sheng Yang He, Elliot Ryser, Hui Li, and Wei Zhang reviewed and edited the manuscript.

CHAPTER V

CONCLUSIONS AND FUTURE WORK

Conclusions

The promise of nanotechnology to enhance ecosystem and agricultural sustainability critically depends on science-based management of its benefits and risks. This dissertation research demonstrated the potential application of ENMs to treat contaminated water, as well as the uptake of ENMs by plants and underlying mechanisms. Its main findings are as follows:

1. The novel ZnO nanowires exhibited high photodegradation efficiency for cephalexin at circumneutral and alkaline pH with satisfactory reusability over at least five cycles. Cephalexin was degraded through hydroxylation, demethylation, decarboxylation, and dealkylation. Inorganic anions (HCO_3^-) and natural organic matter decreased the degradation rate due to the quenching of reactive species (•OH and $•O_2^-$).
2. Biochar amendment had no significant effect on the uptake of Ag by radish plants, which did not differ with or without Ag addition (1 mg/kg). The Ag concentration in soil exchangeable fractions and soil pore water exhibited low bioavailability of Ag at environmentally-relevant concentrations (e.g., 1 mg/kg), which may partially explain the non-significant effect of biochar amendment on Ag uptake. Therefore, the risk of Ag NPs and Ag^+ ions accumulating in vegetable crops at environmentally-relevant concentrations appear to be very low.
3. Stomata facilitated the internalization of Ag NPs, as revealed by the greater amount of Ag NPs sorbed to ABA-responsive Ler and Col-7 ecotype leaves in the ABA-free control than those treated with 10 μM ABA. However, Ag NPs sorption by the *ost1-2* and *scord7* mutant leaves was similar with and without ABA. The sorbed Ag NPs were widely attached to the leaf surface, localized near the cell membrane, and in the cytoplasm and plasmodesmata.

Future Work

This dissertation research points to several new research directions. Considering the high efficiency of ZnO nanowires and the inhibitory effect of HCO_3^- and NOM on the photodegradation of cephalexin, future work should be directed to develop effective engineering solutions for water enriched with HCO_3^- and NOM. To avoid the need of separating ZnO nanowires from treated water, ZnO nanowires may be embedded into membrane reactors for advanced water and wastewater treatments. The identified photodegradation pathways suggest that parent compound cephalexin is not completely removed but transformed into other product compounds. As these transformed products may be also bioactive, future work should test the bioactivity of transformed intermediates produced during photodegradation. It is also plausible that ZnO nanowires could be used as catalysts to photodegrade other organic contaminants (including antibiotics), which should be further investigated.

In soil-water-plant systems, uptake of Ag NPs by radish plants at environmentally-relevant concentrations appeared to be low, mainly due to low bioavailability of Ag in soil pore water. Future work should extend this type of study to more vegetable and soil types, assisted with advanced analytical techniques (e.g., FTIR, XPS, XANES, and single particle inductively coupled plasma mass spectrometry) to molecularly speciate Ag in diverse soil, water, and plant systems. Finally, recognizing that stomata facilitate the internalization of ENMs, future research could develop stomata manipulation strategies to enhance the internalization of beneficial ENMs and minimize the accumulation of harmful ENMs in plants so as to improve agricultural productivity, food safety, and the human health.

APPENDICES

APPENDIX A: Supplementary Materials to CHAPTER II

Text A1. LC-QTrap-MS/MS Method

Cephalexin was analyzed using a LC-QTrap-MS/MS system. The sample injection volume was 10 μL, and the flow rate was 0.35 mL min^{-1}. After a 2 min pre-equilibration with 100% phase A, the gradient program for phase B was as follows: the phase B increased to 40% from 0.01 to 1.0 min, then to 70% from 1.0 to 2.0 min, maintained at 70% from 2.0 to 3.2 min, then increased to 100% from 3.2 to 3.5 min, and finally maintained at 100% until 4.5 min. The mass spectrometer was set to positive polarity. The curtain gas pressure, ion spray voltage, temperature, and entrance potential were 20 psi, 5000 V, 700 °C, and 10 V, respectively. The multiple reaction monitoring (MRM) mode was used with the transitions of one precursor ion m/z 348.0 to three product ions of m/z 190.5, m/z 174.0, and m/z 158.0 for qualification and quantification. The retention time for cephalexin was 2.56 min. All the samples were quantified using matrix-matched standard curves.

The LC-QTrap-MS/MS was used to identify cephalexin degradation products under positive ionization mode, using the combination of an enhanced mass scan (EMS) as survey scan, information dependent acquisition (IDA) criteria, and an enhanced product ion (EPI) scan. The EMS scan for MS spectrum was performed at a scan rate of 10,000 Da/s from m/z 50 to 600. The declustering potential (DP), entrance potential (EP), and collision energy (CE) were respective 60 V, 10 V, and 10 V. The IDA threshold was selected at 1000 cps to trigger the EPI scan, following the same scanning rate, DP voltage, and EP voltage with those in the EMS scan, while the CE was set up at 35 V. The collision energy spread (CES) was selected at 15 V. Thus, the averaged MS/MS spectrum was acquired with CE at 20, 35 and 50 V.

The MasterView software in PeakView 2.2 package was utilized to process the obtained LC-QTrap-MS/MS data. The intensity of precursor ion > 3 (default threshold of the ratio of

precursor ion in cephalexin degradation sample to that in cephalexin-free control) was regarded as positive result. The MS spectra of precursors and their corresponding EPI-triggered MS/MS spectra were then linked to Formula Finder in MasterView to obtain related molecular formulas. The calculated formula was used to search candidate chemicals and their structures in ChemSpider database (http://www.chemspider.com/). Then possible structure was compared to parent cephalexin for similar moieties. If candidate structure could be assigned to the fragments of mass spectra, degradation product was considered to be tentatively identified. If no appropriate chemical structure was obtained from the ChemSpider database, ChemDraw software (ChemOffice programs, PerkinElmer, Waltham, MA) was used to construct the possible structures based on MS spectra, m/z value, theoretical frontier electron densities calculation, and literature report. It should be noted that the tentatively identified intermediates in our study were not further confirmed due to the lack of authentic standards.

Table A1. Experimental conditions in selected photocatalytic degradation studies using ZnO photocatalysts in literature.

Catalyst	Initial contaminant concentration	Catalyst-to-substrate ratio	Reference
[ZnO nanowires] = 0.02 g L^{-1}	[cephalexin] = 0.1 mg L^{-1}	200	This study
[ZnO] = 0.3 g L^{-1} coupled with g-C_3N_4	[cephalexin] = 10 mg L^{-1}	30	Ref. 114
[Mg/ZnO] = 1 g L^{-1}	[Alprazolam] = 9.26 mg L^{-1}	108	Ref. 124
[Sm/ZnO] = 1 g L^{-1} assisted with 0.7 g L^{-1} oxidants	[Phenazopyridine] = 10 mg L^{-1}	100	Ref. 123
[ZnO] = 2.5 g L^{-1}	[Phenol] = 5 mg L^{-1}	500	Ref. 126
[Ag/ZnO] = 0.5 g L^{-1}	[17α-ethinylestradiol] = 2.72 mg L^{-1}	184	Ref. 125
[Ag/ZnO] = 2 g L^{-1}	[4-Nitrophenol] = 10 mg L^{-1}	200	Ref. 122

Table A2. Frontier electron densities on atoms in cephalexin calculated by Gaussian 09 program at B3LYP/6-311 + G* level with a minimum energy.

Atom	FED_{HOMO}^2	FED_{LUMO}^2	$2FED_{HOMO}^2$	$FED_{HOMO}^2 + FED_{LUMO}^2$
1 N	0.004251866	0.485560852	0.008503732	0.489812718
2 C	0.163749548	1.228750884	0.327499096	**1.392500432**
3 C	0.08037574	1.141394638	0.16075148	**1.221770377**
4 C	0.113732447	0.244017191	0.227464893	0.357749638
5 S	0.001361835	0.741890991	0.002723671	0.743252826
6 C	0.376261972	0.552627218	0.752523943	0.92888919
7 C	0.243136328	4.212149049	0.486272656	**4.455285377**
8 C	0.343154656	1.877726761	0.686309312	**2.220881417**
9 C	0.02587449	0.114011265	0.05174898	0.139885755
10 O	0.000181535	0.074699571	0.000363071	0.074881107
11 O	6.89978E-05	0.029746121	0.000137996	0.029815119
12 O	0.000660392	0.052178361	0.001320783	0.052838753
13 C	0.003897018	0.087886766	0.007794036	0.091783784
14 N	0.004908516	0.075190573	0.009817032	0.080099089
15 C	0.089167018	0.119093666	0.178334036	0.208260684
16 O	0.002184652	0.001695121	0.004369303	0.003879773
17 C	3.01106679	0.087435504	**6.022133579**	**3.098502294**
18 C	3.390075783	0.82461508	**6.780151565**	**4.214690863**
19C	0.961790173	0.292928391	**1.923580346**	**1.254718564**
20 C	0.524839639	0.110022154	**1.049679278**	0.634861793
21 C	0.221848389	0.085530162	0.443696778	0.307378551
22 C	0.335262116	0.023804345	0.670524231	0.359066461
23 C	4.398273923	1.489053594	**8.796547846**	**5.887327517**
24 N	0.634257238	0.010682341	**1.268514475**	0.644939579

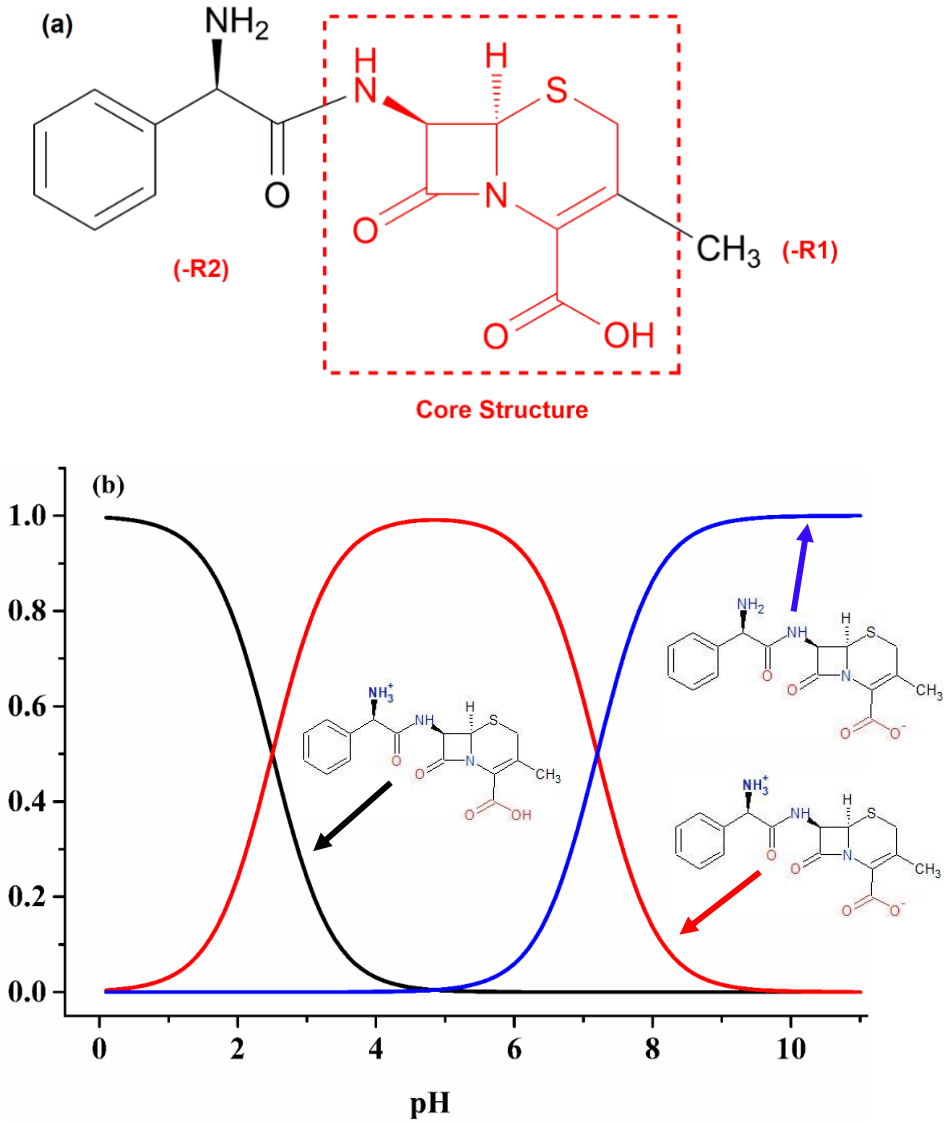

Figure A1. Chemical structure (a) of cephalexin and species distribution (b) as a function of solution pH (pKa$_1$ = 2.5 and pKa$_2$ = 7.2).

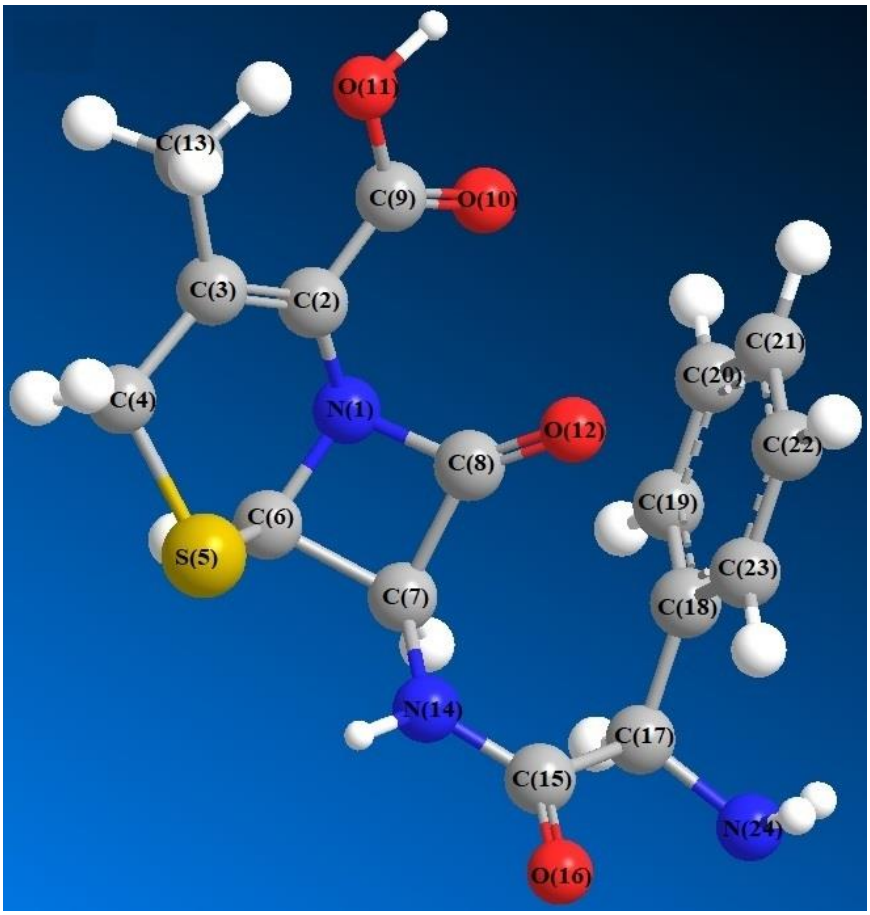

Figure A2. Structural formula of cephalexin optimized by Gaussian 09 program.

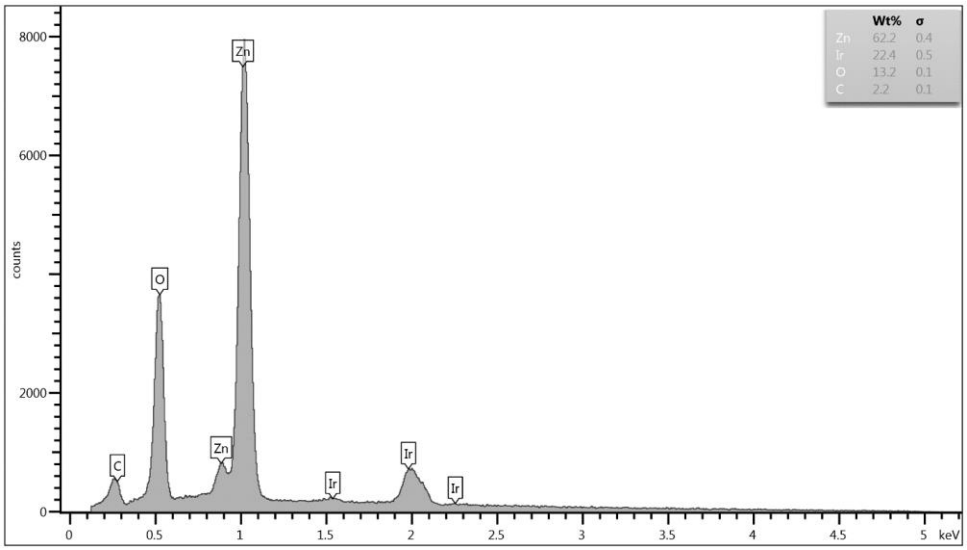

Figure A3. Energy dispersive X-ray spectroscopy for elemental analysis. Elements C and Ir are background, confirming that the powders are primarily ZnO.

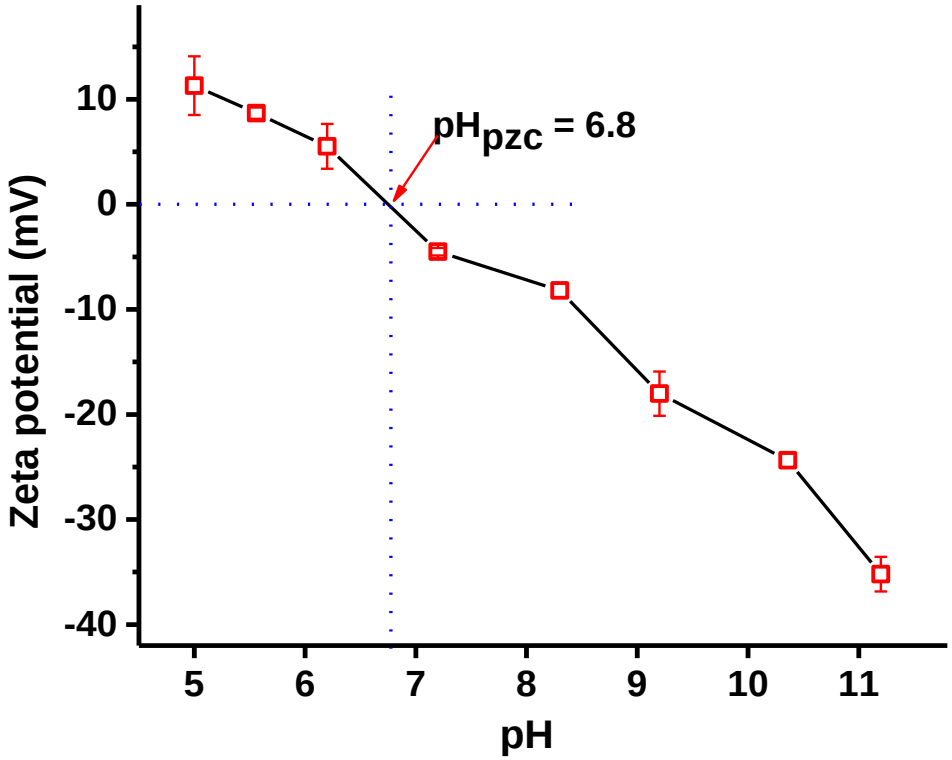

Figure A4. Zeta potential of ZnO nanowires (20 mg L^{-1}) suspended in background solution (5 mM NaCl) as a function of solution pH.

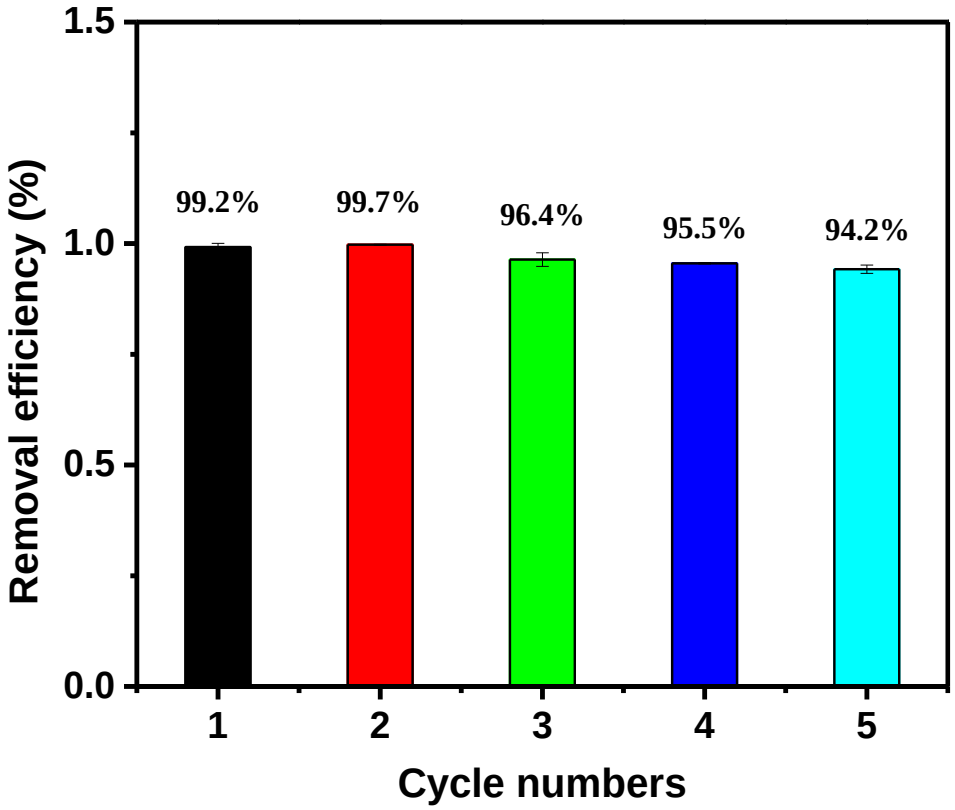

Figure A5. Removal efficiency of cephalexin by ZnO nanowires (20 mg L^{-1}) under simulated sunlight at pH 7.2 in 5 cycles (90 min reaction time each cycle).

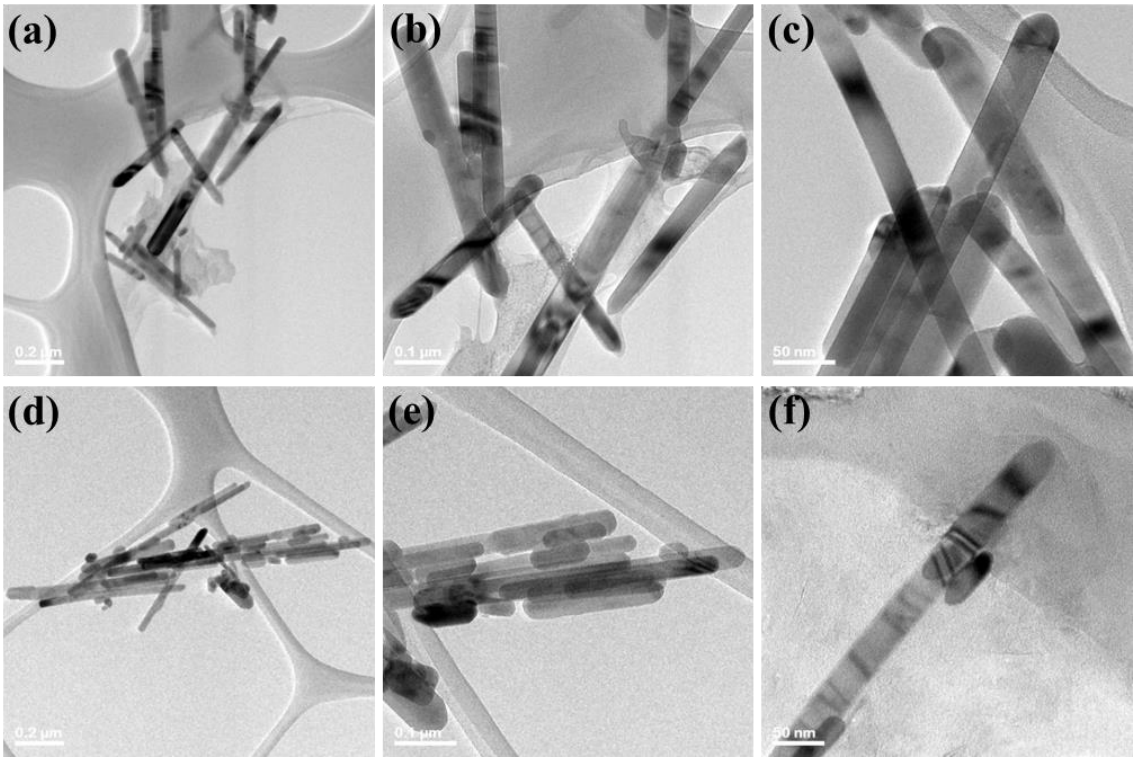

Figure A6. Representative TEM images for morphology comparison of ZnO nanowires before (a–c) and after (d–f) photoreaction (i.e., [ZnO nanowires] = 20 mg L^{-1}, [cephalexin] = 100 µg L^{-1}, [NaCl] = 5 mM, pH = 7.2, and irradiation time = 180 min).

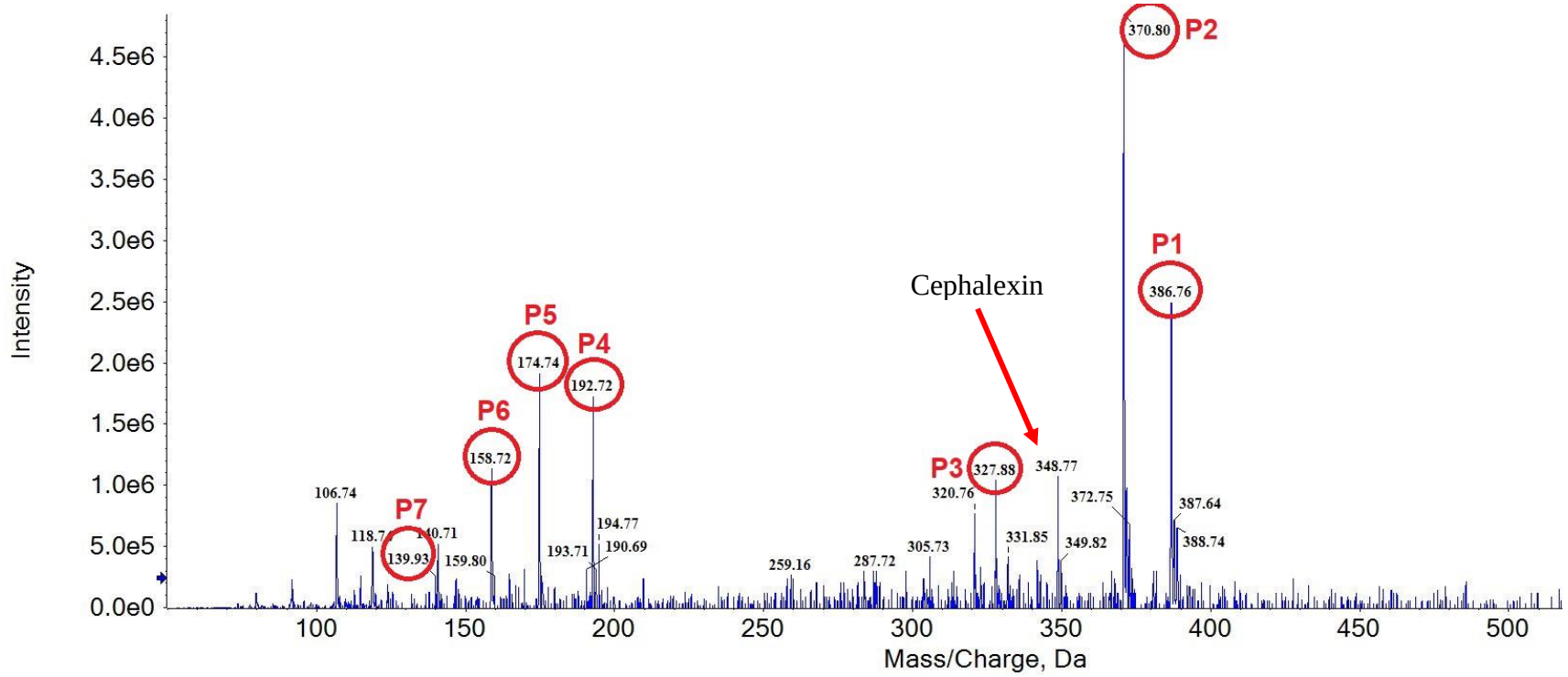

Figure A7. LC chromatograms and m/z of degradation products of cefalexin by ZnO nanowires under simulated sunlight.

Table A3. ***Photodegradation Kinetics Data***

Experiments	Replicates	Cephalexin concentration (μg L^{-1}) over time									
		Initial	5 min	15 min	25 min	45 min	65 min	95 min	125 min	155 min	180 min
Hydrolysis	1	138.60	130.72	138.88	137.08	133.48	128.76	127.49	134.92	125.56	125.97
	2	134.16	132.68	126.08	127.64	132.00	124.15	123.60	129.55	125.09	118.98
Photolysis	1	129.65	125.16	128.06	129.08	126.81	126.16	122.09	126.16	118.93	128.27
	2	133.41	125.56	122.09	131.27	123.96	126.60	122.48	122.17	124.12	125.24
	3	130.04	125.95	124.41	125.87	126.65	126.44	119.01	122.58	121.85	130.04
10 mg L^{-1} Zn^{2+}	1	104.27	106.78	105.07	104.32	104.68	96.70	93.61	91.42	89.01	85.56
	2	106.39	107.77	105.82	104.63	104.80	97.16	94.96	89.71	89.92	89.95
	3	105.07	104.90	104.22	104.83	102.37	99.59	90.00	90.19	89.44	87.10
20 mg L^{-1} ZnO nanowires	1	108.40	51.33	2.69	4.41	0.52	0.14	0.32	0.05	0.02	0.02
	2	112.13	54.66	16.01	4.53	0.73	0.17	0.04	0.04	0.04	0.03
	3	115.28	49.15	16.68	4.42	0.70	0.17	0.03	0.05	0.02	0.03
40 mg L^{-1} ZnO nanowires	1	95.92	29.19	4.57	0.26	0.04	0.05	0.02	0.03	0.03	0.02
	2	97.44	31.83	3.24	0.17	0.05	0.02	0.03	0.03	0.03	0.03
	3	99.77	32.20	4.20	0.32	0.02	0.02	0.03	0.03	0.05	0.03
80 mg L^{-1} ZnO nanowires	1	42.36	7.23	0.69	0.12	0.05	0.03	0.02	0.02	0.02	0.03
	2	35.93	8.05	0.93	0.11	0.05	0.03	0.03	0.04	0.01	0.03
	3	38.11	7.38	0.69	0.04	0.03	0.02	0.37	0.03	0.03	0.02
EDTA-2Na (h^+)	1	137.94	135.62	133.30	131.01	136.68	136.63	137.94	137.15	135.34	131.51
	2	143.73	132.23	139.81	137.63	143.73	141.41	141.96	134.76	135.55	134.02
	3	141.63	139.45	139.24	139.98	141.63	141.44	140.10	136.29	135.62	130.38
tert-butanol (•OH)	1	119.59	114.57	109.64	97.94	95.89	86.56	78.23	72.46	64.09	63.47
	2	113.09	117.18	106.17	99.91	93.18	86.77	79.43	74.88	67.46	68.09
	3	120.12	110.50	106.84	98.42	98.76	84.93	80.77	75.36	67.08	65.14

Table A3 (cont'd)

	1	137.54	63.21	24.81	12.60	4.61	1.88	0.78	0.33	0.27	0.20
$K_2Cr_2O_7$ (e^-)	2	129.81	60.60	23.45	11.56	4.26	1.61	0.62	0.24	0.17	0.10
	3	133.47	59.02	23.45	12.48	3.58	1.30	0.49	0.22	0.17	0.12
	1	216.83	152.61	125.58	105.27	103.86	98.61	98.92	103.08	101.94	106.86
p-benzoquinone	2	206.73	152.72	121.67	107.84	103.21	99.55	103.41	106.00	100.05	105.98
($\bullet O_2^-$)	3	196.29	150.99	122.68	115.37	103.25	94.60	97.71	104.84	99.35	106.54
	1	95.18	88.38	89.14	90.11	92.90	88.45	87.12	84.46	82.35	81.82
pH = 5.0	2	99.06	93.62	92.58	93.02	91.98	90.60	88.80	88.47	85.07	85.80
	3	96.40	91.08	92.19	96.98	94.79	92.28	88.50	88.02	89.68	88.08
	1	75.58	77.17	82.40	73.18	62.25	60.10	40.53	45.30	44.22	39.22
pH = 6.2	2	67.97	75.36	81.92	74.53	61.90	55.47	44.08	40.32	40.25	33.78
	3	76.68	80.11	81.75	70.91	61.56	56.60	44.86	40.81	37.85	32.30
	1	122.12	42.14	2.41	0.02	0.02	0.01	0.01	0.01	0.01	0.01
pH = 8.3	2	130.43	38.66	2.58	0.08	0.02	0.02	0.01	0.02	0.01	0.01
	3	122.74	38.45	3.63	0.14	0.02	0.01	0.01	0.01	0.01	0.01
	1	112.82	25.62	1.03	0.05	0.07	0.04	0.02	0.04	0.09	0.05
pH = 9.2	2	103.01	23.84	0.65	0.10	0.06	0.06	0.03	0.04	0.04	0.05
	3	103.42	24.55	0.97	0.05	0.01	0.02	0.02	0.02	0.03	0.12
	1	127.27	64.54	29.58	15.86	5.85	2.47	0.43	0.08	0.03	0.01
1 mM HCO_3^-	2	117.36	60.13	24.45	10.16	1.86	0.50	0.07	0.02	0.01	0.02
	3	119.81	61.97	27.03	15.39	4.47	1.58	0.35	0.07	0.03	0.02
	1	100.29	68.98	39.96	25.00	11.90	5.79	2.04	0.70	0.30	0.19
2 mM HCO_3^-	2	123.38	64.57	30.24	18.05	6.78	2.77	0.74	0.19	0.07	0.04
	3	109.46	61.39	24.85	13.64	4.59	1.82	0.40	0.12	0.05	0.04
	1	65.37	83.10	76.31	72.46	73.85	65.59	64.35	58.84	53.57	50.13
5 mM HCO_3^-	2	71.96	78.93	76.22	75.04	72.37	63.69	59.08	55.21	51.16	48.52
	3	75.85	79.66	79.25	69.61	69.59	62.71	60.04	57.92	53.29	53.31

Table A3 (cont'd)

2 mg L^{-1} SRNOM	1	122.87	100.97	68.59	51.00	19.37	5.06	1.09	0.20	0.14	0.09
	2	117.24	100.66	75.37	51.42	20.74	5.74	1.00	0.28	0.20	0.01
	3	116.21	99.37	72.80	56.15	25.26	7.39	1.55	0.63	0.51	0.12
5 mg L^{-1} SRNOM	1	92.25	98.43	89.23	87.18	79.84	50.69	67.27	58.27	52.07	50.53
	2	90.79	94.10	87.69	88.47	83.50	76.13	68.88	64.32	61.15	54.70
	3	92.65	97.29	91.13	87.02	82.00	73.07	66.35	61.74	62.11	53.12
10 mg L^{-1} SRNOM	1	94.94	94.88	88.99	85.06	83.65	71.71	70.48	52.60	72.14	61.22
	2	93.50	96.75	90.13	83.52	55.77	70.10	75.37	70.79	68.74	58.56
	3	87.89	92.58	95.88	82.85	65.19	71.29	67.34	64.55	63.47	44.03

APPENDIX B: Supplementary Materials to CHAPTER III

Table B1. Fitted parameters of the sorption isotherms using the Langmuir model*.

Sorbate	Sorbent	q_{max} (mg g^{-1})	k_L (L mg^{-1})	R^2
$AgNO_3$	soil + 0% biochar	5.1 (0.2) a	2.4 (0.2) × 10^{-2} a	0.97
	soil + 0.1% biochar	4.7 (0.0) a	3.1 (0.5) × 10^{-2} a	0.98
	soil + 1.0% biochar	4.7 (0.6) a	3.5 (0.8) × 10^{-2} a	0.98
Ag NPs	soil + 0% biochar	2.1 (0.1) A	2.1 (0.3) × 10^{-2} A	0.99
	soil + 0.1% biochar	2.1 (0.1) A	2.3 (0.2) × 10^{-2} A	0.95
	soil + 1.0% biochar	4.2 (2.3) A	9.2 (0.9) × 10^{-3} A	0.97

*Results with the same letter in a column are not significantly different among treatments by the LSD post-hoc comparison test at the 5% level. Numbers in parentheses are standard deviations from two replicates.

Table B2. Fractions of Ag^+ and Ag NPs in the soil samples collected from the radish-growing pots on Day 35*.

Treatment	Biochar	f1: exchangeable (%)	f2: reducible (%)	f3: oxidisable (%)	f4: residual (%)
blank	0%	0.10	4.72	25.1	70.1
	0.1%	0.08	4.67	18.8	76.5
	1.0%	0.22	6.45	29.5	63.9
$AgNO_3$	0%	0.01 ± 0.00 a	73.4 ± 14.9 a	8.9 ± 3.9 a	18.1 ± 18.8 a
	0.1%	0.03 ± 0.03 a	77.6 ± 11.2 a	7.6 ± 2.4 a	14.7 ± 8.8 a
	1.0%	0.00 ± 0.00 a	39.2 ± 6.4 b	15.1 ± 8.9 a	45.6 ± 3.7 b
Ag NPs	0%	0.02 ± 0.01 A	76.6 ± 4.6 A	9.2 ± 1.8 A	14.2 ± 2.8 A
	0.1%	0.05 ± 0.04 A	66.5 ± 6.3 A	16.2 ± 4.1 AB	17.3 ± 2.7 A
	1.0%	0.02 ± 0.01 A	65.4 ± 6.2 A	18.9 ± 5.8 BC	15.7 ± 3.6 A

*Results are expressed as means ± standard deviations (n = 3). The same letter in a column represents that means are not significantly different among different biochar amendments (0%, 0.1%, and 1.0%) by the LSD post-hoc comparison test at the 5% level.

Table B3. Fractions of Ag^+ and Ag NPs in the soil samples collected from the radish-free pots on Day 35*.

Treatment	Biochar	f1: exchangeable (%)	f2: reducible (%)	f3: oxidisable (%)	f4: residual (%)
$AgNO_3$	0%	0.03 ± 0.00 a	73.4 ± 1.8 a	5.1 ± 17.0 a	21.5 ± 0.0 a
	0.1%	0.07 ± 0.00 a	64.8 ± 4.5 ab	16.7 ± 1.7 a	18.4 ± 2.9 a
	1.0%	0.04 ± 0.01 a	58.3 ± 4.1 bc	23.8 ± 9.5 a	17.9 ± 13.7 a
Ag NPs	0%	0.01 ± 0.00 A	49.3 ± 8.8 A	8.8 ± 6.7 A	41.8 ± 2.3 A
	0.1%	0.09 ± 0.08 A	69.9 ± 17.5 A	16.9 ± 11.9 A	13.2 ± 5.6 B
	1.0%	0.03 ± 0.00 A	61.9 ± 16.9 A	20.7 ± 8.3 A	17.4 ± 8.6 B

* Results are expressed as means ± standard deviations (n = 2). The same letter in a column represents that means are not significantly different among different biochar amendments (0%, 0.1%, and 1.0%) by the LSD post-hoc comparison test at the 5% level.

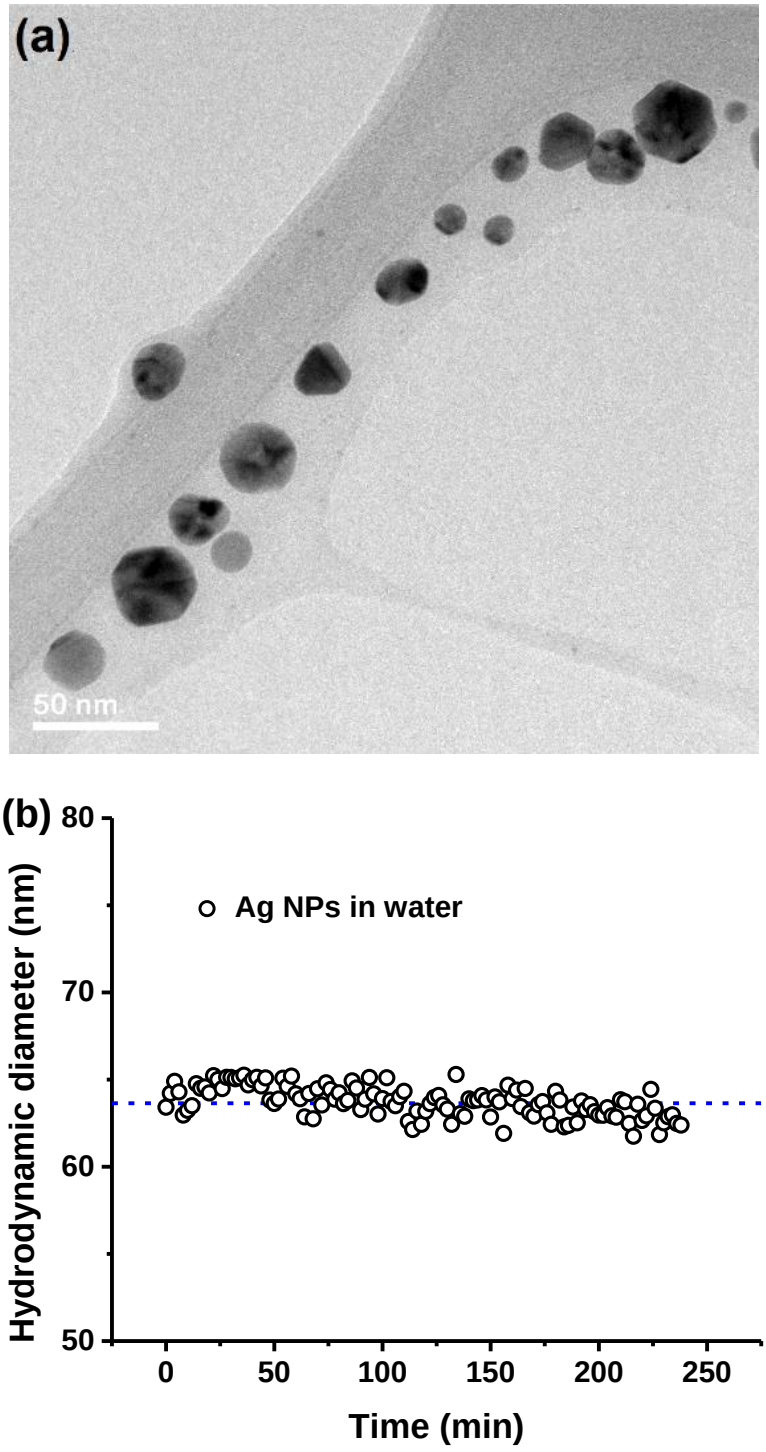

Figure B1. Representative transmission electron microscopy image (a) and aggregation kinetics (b) of Ag NPs (10 mg L^{-1}) dispersed in deionized water. The Ag NPs suspension was stable at a time frame of 4 h.

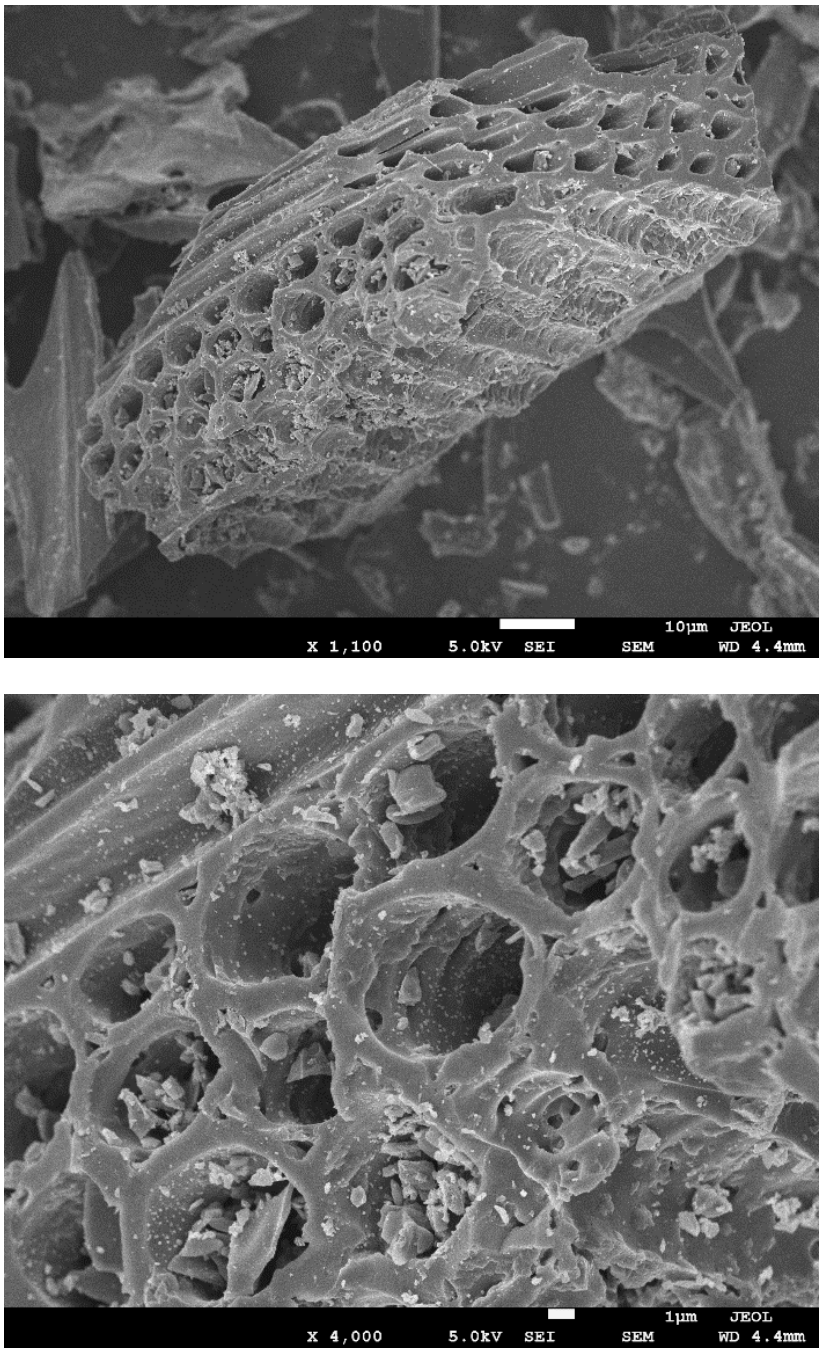

Figure B2. Representative scanning electron microscopy images of the biochar used in this study.

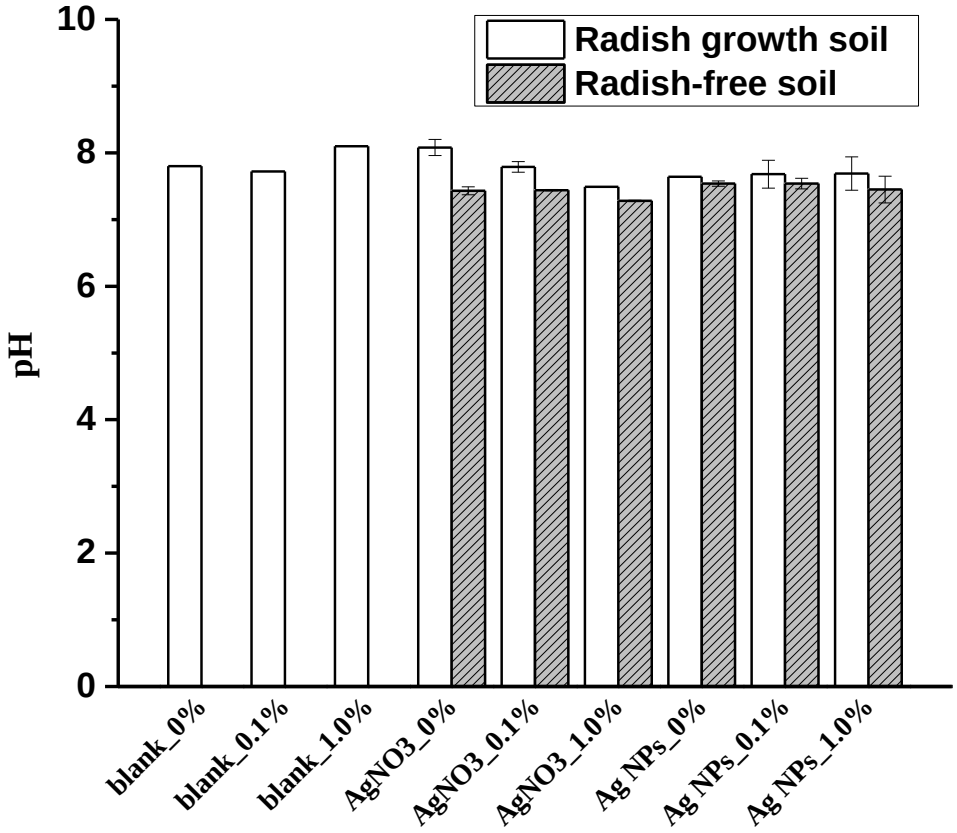

Figure B3. Measured pH values of soil samples collected from the radish-growing and radish-free pots on Day 35.

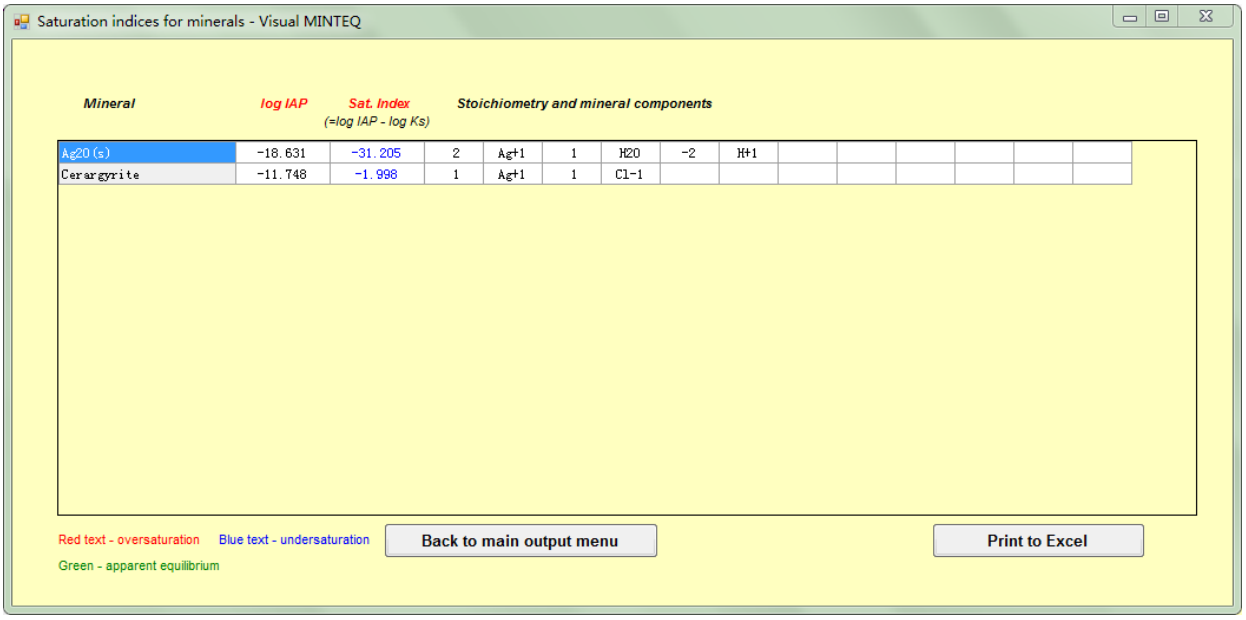

Figure B4. The MINTEQ calculation showed that no precipitation occurs (blue text indicates undersaturation) during hydroxylammonium chloride extraction. Simulation condition: $[Ag^{+}]$ = 0.05 mg L^{-1} (assuming maximum dissolution, 1 mg silver/kg soil × 1 g soil ÷ 20 ml = 0.05 mg L^{-1}); $[NH_2OH{\cdot}HCl]$ = 0.5 M; pH = 2; T = 25 °C.

Table B4. ***$AgNO_3$ Sorption Data***

$AgNO_3$									
Initial concentration (mg L^{-1})	0% biochar-Rep. 1			0% biochar-Rep. 2			0.1% biochar-Rep. 1		
	Soil (g)	C_e (mg L^{-1})	Q_s (mg g^{-1})	Soil (g)	C_e (mg L^{-1})	Q_s (mg g^{-1})	Soil (g)	C_e (mg L^{-1})	Q_s (mg g^{-1})
1	0.51	0.07	0.05	0.51	0.06	0.05	0.50	0.12	0.04
2	0.50	0.09	0.09	0.50	0.09	0.10	0.51	0.15	0.09
5	0.50	0.22	0.24	0.51	0.23	0.24	0.50	0.29	0.23
10	0.51	1.02	0.44	0.50	1.14	0.44	0.51	1.03	0.44
20	0.50	4.27	0.78	0.51	2.88	0.84	0.50	4.51	0.77
50	0.50	18.63	1.56	0.51	17.90	1.58	0.50	18.82	1.56
100	0.50	48.59	2.56	0.50	49.63	2.50	0.51	49.14	2.52
200	0.51	119.89	3.96	0.50	121.19	3.92	0.50	124.79	3.74
Initial concentration (mg L^{-1})	0.1% biochar-Rep. 2			1.0% biochar-Rep. 1			1.0% biochar-Rep. 2		
	Soil (g)	C_e (mg L^{-1})	Q_s (mg g^{-1})	Soil (g)	C_e (mg L^{-1})	Q_s (mg g^{-1})	Soil (g)	C_e (mg L^{-1})	Q_s (mg g^{-1})
1	0.51	0.12	0.04	0.50	-0.02	0.05	0.50	-0.02	0.05
2	0.50	0.14	0.09	0.50	0.02	0.10	0.50	0.01	0.10
5	0.50	0.32	0.23	0.51	0.12	0.24	0.50	0.17	0.24
10	0.51	0.87	0.45	0.50	0.89	0.46	0.50	0.83	0.45
20	0.50	3.83	0.80	0.51	3.70	0.81	0.50	3.11	0.84
50	0.51	17.20	1.61	0.50	16.84	1.65	0.50	17.02	1.64
100	0.51	44.45	2.74	0.51	45.28	2.69	0.50	45.28	2.73
200	0.51	122.49	3.83	0.51	125.37	3.67	0.51	117.77	4.06

Table B5. ***Ag NPs Sorption Data***

Ag NPs									
initial concentration (mg L^{-1})	0% biochar-Rep. 1			0% biochar-Rep. 2			0.1% biochar-Rep. 1		
	Soil (g)	C_e (mg L^{-1})	Q_s (mg g^{-1})	Soil (g)	C_e (mg L^{-1})	Q_s (mg g^{-1})	Soil (g)	C_e (mg L^{-1})	Q_s (mg g^{-1})
1.11	0.51	0.06	0.05	0.51	0.06	0.05	0.51	0.02	0.05
2.22	0.50	0.44	0.09	0.50	0.44	0.09	0.50	0.47	0.09
5.56	0.50	3.10	0.12	0.51	2.83	0.14	0.51	2.11	0.17
11.12	0.51	6.99	0.20	0.50	6.89	0.21	0.50	5.51	0.28
22.25	0.51	12.45	0.48	0.50	15.25	0.35	0.51	14.02	0.41
55.62	0.50	33.96	1.07	0.51	37.51	0.89	0.50	33.98	1.08
111.24	0.51	83.87	1.35	0.51	86.53	1.22	0.50	87.13	1.20
222.49	0.51	186.54	1.78	0.51	191.55	1.53	0.50	187.29	1.75
initial concentration (mg L^{-1})	0.1% biochar-Rep. 2			1.0% biochar-Rep. 1			1.0% biochar-Rep. 2		
	Soil (g)	C_e (mg L^{-1})	Q_s (mg g^{-1})	Soil (g)	C_e (mg L^{-1})	Q_s (mg g^{-1})	Soil (g)	C_e (mg L^{-1})	Q_s (mg g^{-1})
1.11	0.51	0.06	0.05	0.50	0.02	0.06	0.51	0.02	0.06
2.22	0.50	0.65	0.08	0.51	0.75	0.07	0.51	0.41	0.09
5.56	0.50	2.87	0.13	0.51	2.46	0.15	0.50	2.23	0.17
11.12	0.50	5.02	0.30	0.51	5.75	0.27	0.51	5.27	0.29
22.25	0.51	13.41	0.44	0.50	14.00	0.41	0.50	13.80	0.42
55.62	0.51	32.53	1.14	0.50	36.00	0.98	0.50	35.06	1.02
111.24	0.50	90.06	1.06	0.51	88.16	1.14	0.50	84.89	1.31
222.49	0.50	183.10	1.97	0.51	173.24	2.44	0.50	182.78	1.99

APPENDIX C: Supplementary Material to CHAPTER IV

Text C1. PVP Removal from Ag NPs Stock

Silver nanoparticles (Ag NPs) with PVP coating were purchased from the US Research Nanomaterials, Inc. (Texas, US). The measured PVP concentration in solution was 0.6%. Ultrafiltration (Amicon Ultra-10kD membrane filter, Millipore, US) was used to remove free PVP in the aqueous suspension. The filter device was centrifuged at 5,000 × g for 25 min to separate the Ag NPs from solution. The retained Ag NPs were rinsed with DI water, followed by centrifugation. The washing was repeated for 3 times, and the Ag NPs were recovered and re-suspended in DI water. The resultant concentration of Ag NP suspension was determined using atomic absorption spectroscopy (AAnalyst 400, PerkinElmer).

Text C2. Ag NPs Characterization

The size and morphology of Ag NPs (US Research Nanomaterials, Inc., Texas, US) were determined using transmission electron microscopy (TEM, JEOL 2200FS, Japan) at an accelerating voltage of 10 kV. One drop of Ag NPs sample was spotted onto a 100-mesh carbon film coated copper grid and dried in the air. The TEM size distribution was calculated using Image J by randomly selecting ~150 particles from 15 TEM micrographs.

Time-resolved dynamic light scattering (DLS) was used to characterize the aggregation kinetics of Ag NPs suspension at pH 6.5 in DI water by measuring hydrodynamic diameter of a 3-mL Ag NP suspension (10 mg L^{-1}) over 3 h using a Zetasizer (Nano-ZS, Malvern Instruments, UK). The scattered light intensity was detected at a scattering angle of 173º. The zeta (ζ) potential of Ag NPs suspension was measured with the Zetasizer. All measurements were conducted at least in triplicates using freshly prepared suspensions at room temperature.

Table C1. Measured stomatal aperture width and width-to-length ratio of *Arabidopsis thaliana* treated with opening buffer in the absence (control) or presence of 10 µM abscisic acid (ABA).

Plants	Stomatal aperture width (µm)	
	control	10 µM ABA
Ler	4.03 ± 0.72 (*n* = 42)	2.62 ± 0.89 (*n* = 45)
ost1-2	5.69 ± 0.92 (*n* = 54)	5.68 ± 0.78 (*n* = 54)
Col-7	4.45 ± 0.66 (*n* = 58)	2.58 ± 0.85 (*n* = 63)
scord7	4.56 ± 0.83 (*n* = 36)	4.29 ± 0.84 (*n* = 37)
Plants	Stomatal width-to-length ratio	
	control	10 µM ABA
Ler	0.40 ± 0.09 (*n* = 51)	0.29 ± 0.08 (*n* = 43)
ost1-2	0.45 ± 0.09 (*n* = 57)	0.48 ± 0.11 (*n* = 58)
Col-7	0.41 ± 0.09 (*n* = 84)	0.30 ± 0.08 (*n* = 84)
scord7	0.46 ± 0.05 (*n* = 36)	0.44 ± 0.06 (*n* = 36)

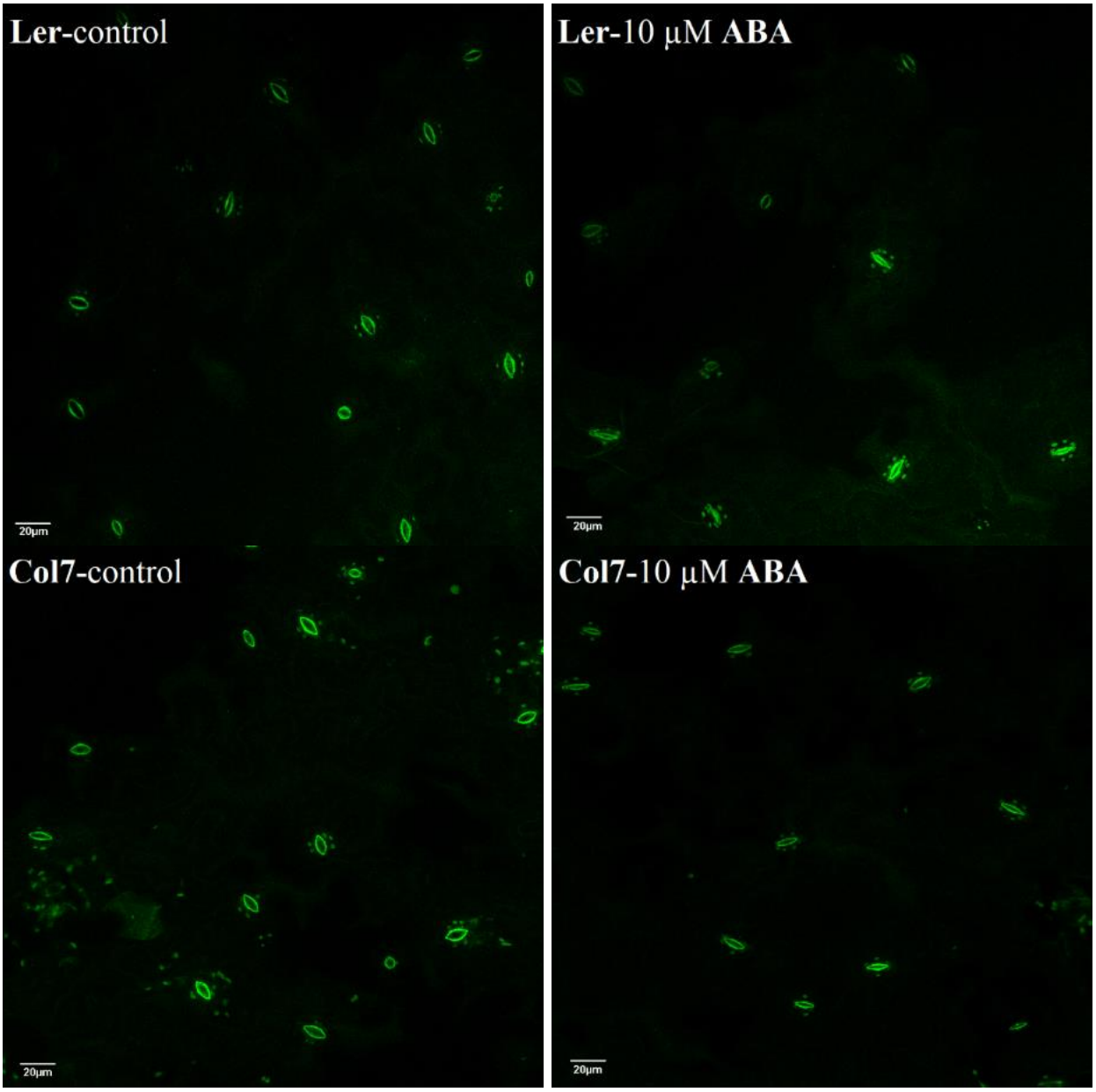

Figure C1. Representative confocal laser scanning microscopy images of *Arabidopsis thaliana* leaves. Images were obtained by scanning leaf discs (3 mm × 3 mm) of Ler, *ost1-2*, Col-7, and *scord7* treated with opening buffer without (control) or with 10 µM abscisic acid (10 µM ABA) solution for 1 h. Scale bar is 20 µm. As observed, the *ost1-2* and *scord7* mutants of *Arabidopsis* did not respond to ABA-induced stomatal closure and exhibited constitutively larger apertures, while the stomata of Ler and Col-7 ecotypes closed with 10 µM ABA treatment.

Figure C1 (Cont'd)

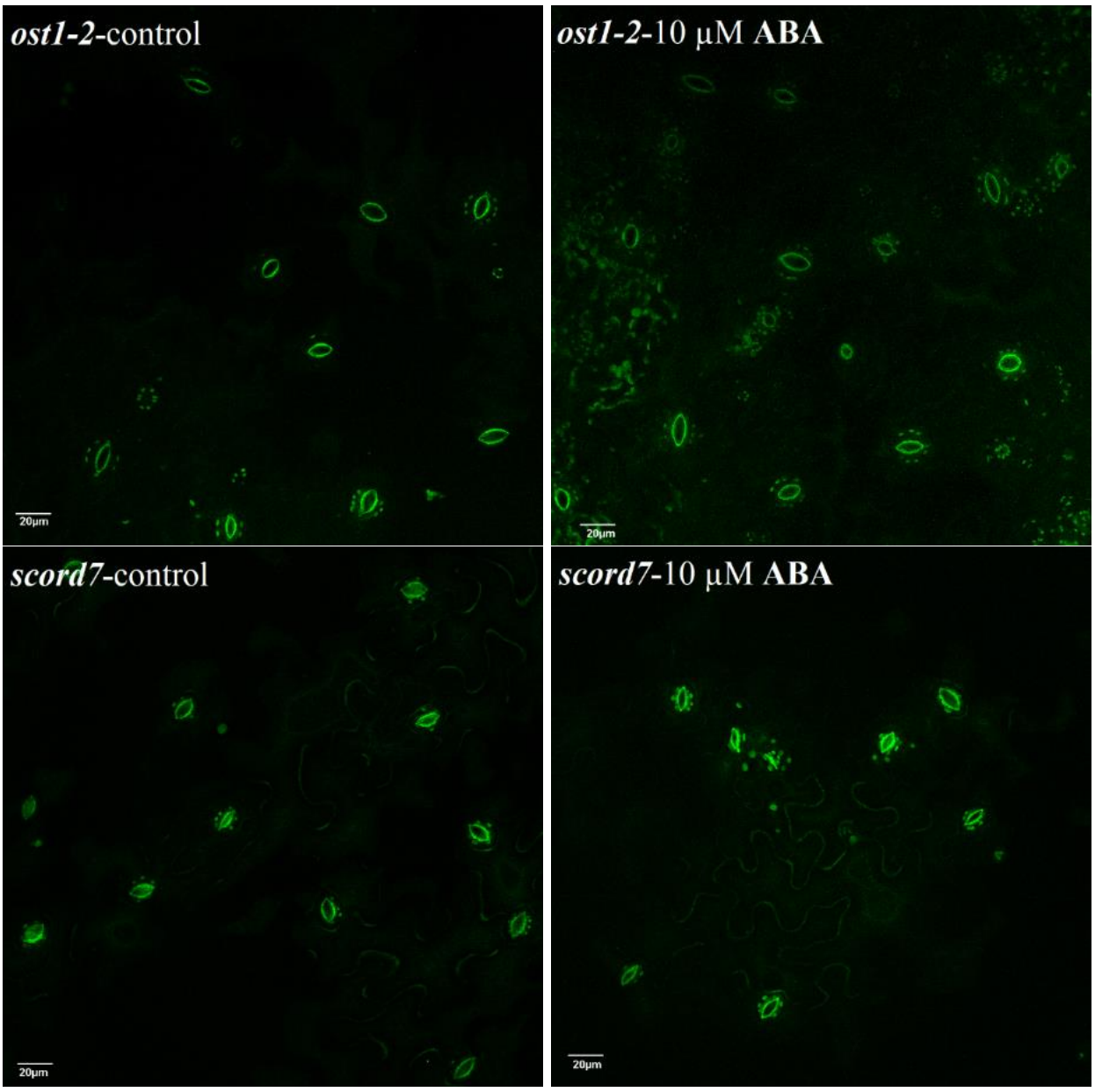

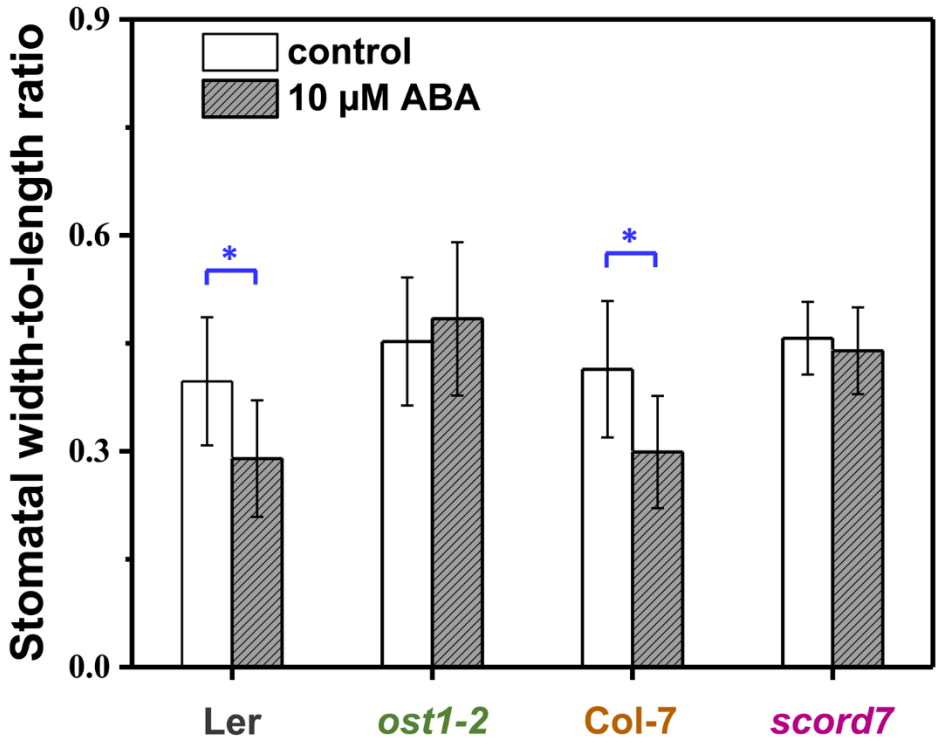

Figure C2. Stomatal width-to-length ratio of *Arabidopsis thaliana* treated with opening buffer in the absence (control) or presence of 10 µM abscisic acid (ABA). Results are shown as mean ± standard deviation (n = 36–84 stomata). Symbol (*) indicates a statistically significant difference in means between the control and 10 µM ABA treatments ($p < 0.05$).

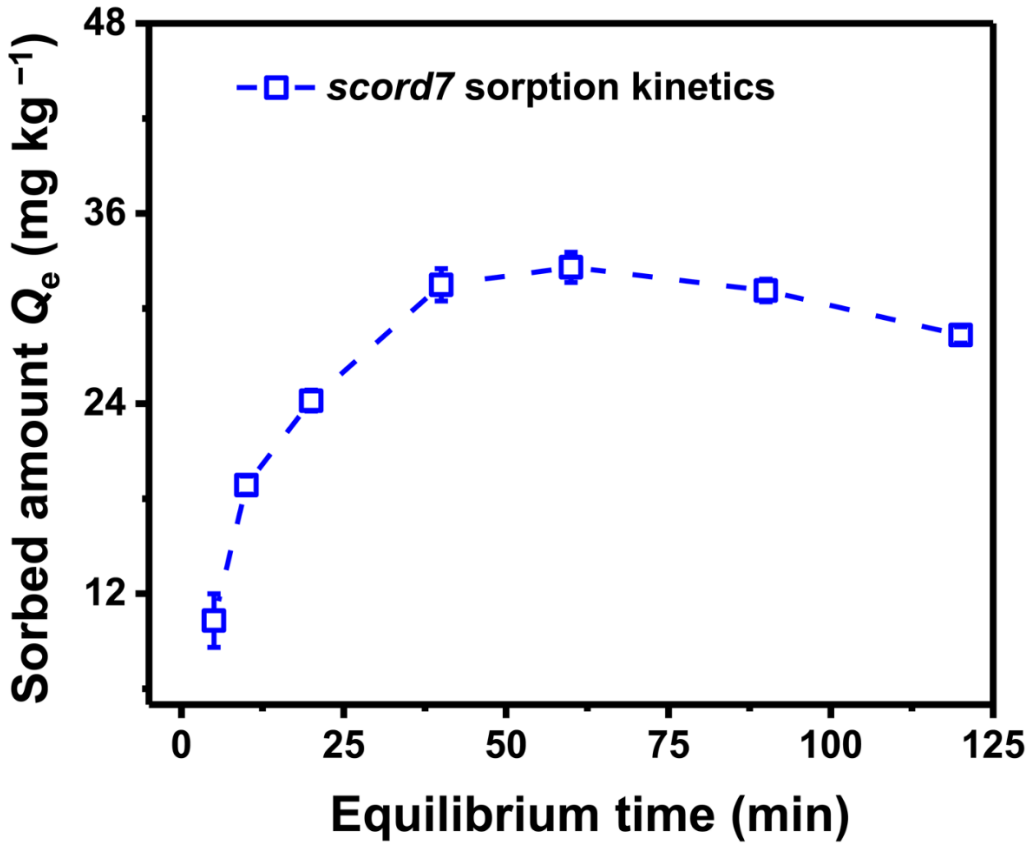

Figure C3. Sorption kinetics of 2 mg L^{-1} Ag NPs on the *scord7* leaves. Error bars represent the standard deviations (n = 2).

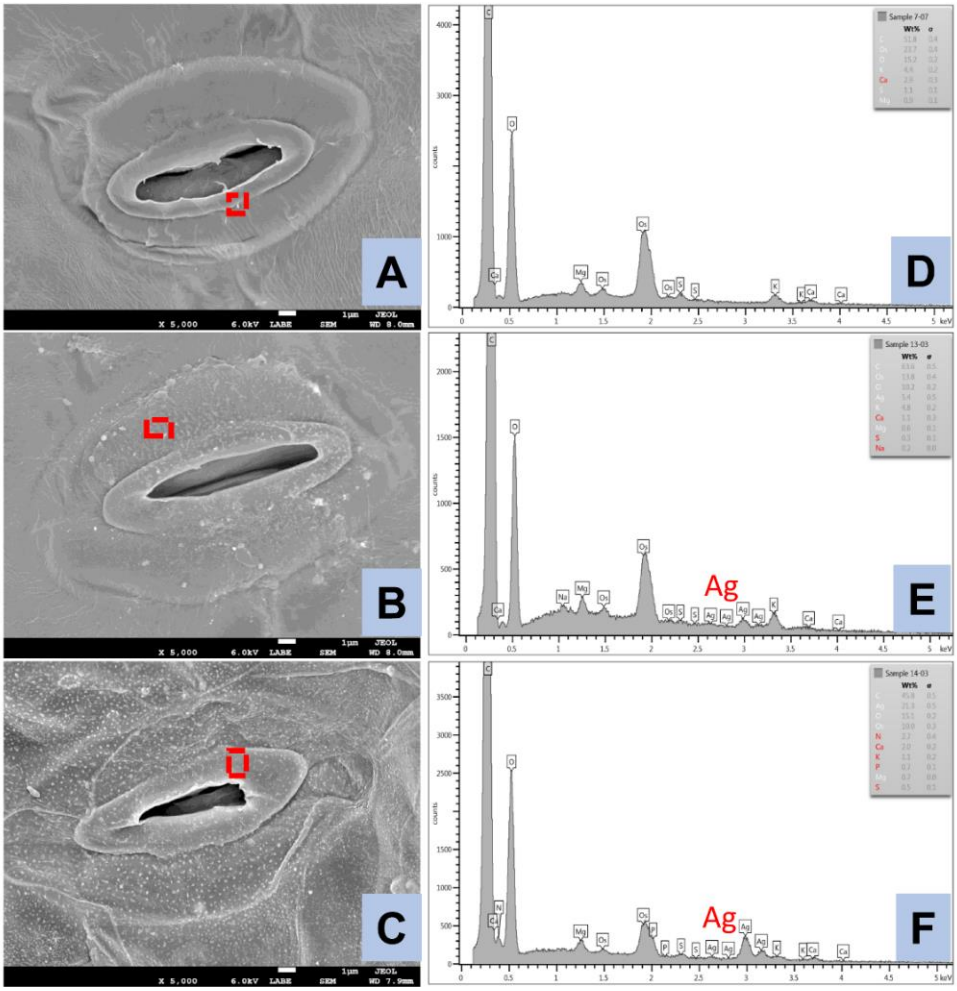

Figure C4. Surface distribution analysis of Ag NPs in the leaves of *Arabidopsis* Col-7 ecotype after the sorption experiment (10 mg L^{-1} Ag NPs exposure) characterized by SEM-EDS. A–C are SEM images; D–F are corresponding EDS spectra from squared areas in A–C. (A) no Ag NPs exposure, denoted as blank; (B) opening buffer treatment for 1 h before 10 mg L^{-1} Ag NPs exposure, denoted as control; (C) opening buffer with 10 µM ABA treatment for 1 h before 10 mg L^{-1} Ag NPs exposure, denoted as 10 µM ABA. Note that the stomata aperture in the SEM images could not represent the opening or closure status due to artifacts during the sample preparation (e.g., freeze-drying). More bright dots were found surrounding the stomatal opening of C than B plausibly due to the ABA induced stomatal closure minimizing the internalization of sorbed Ag NPs.

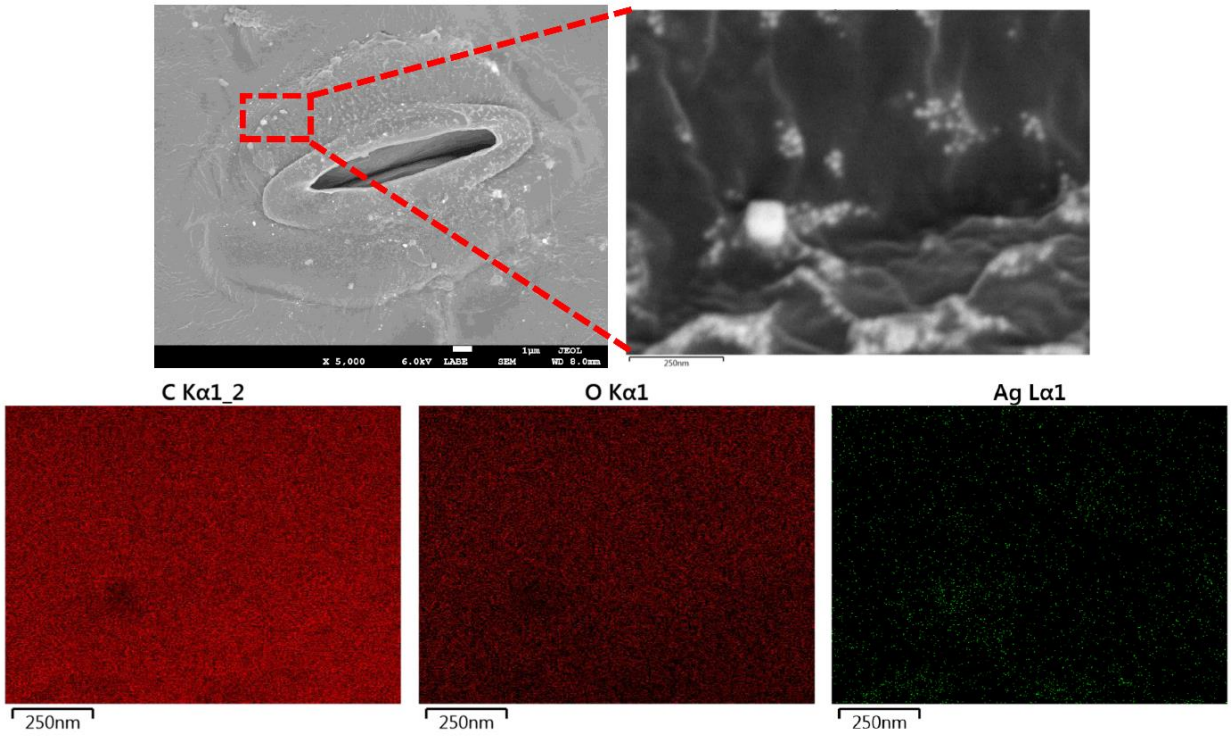

Figure C5. Distribution of Ag NPs in selected micro-area on Col-7 leave after the sorption experiment (10 mg L^{-1} Ag NPs). Upper: SEM images at different magnifications; Bottom: elemental mapping of carbon, oxygen and silver. Mapping images indicate the Ag is widely distributed in the selected micro-area.

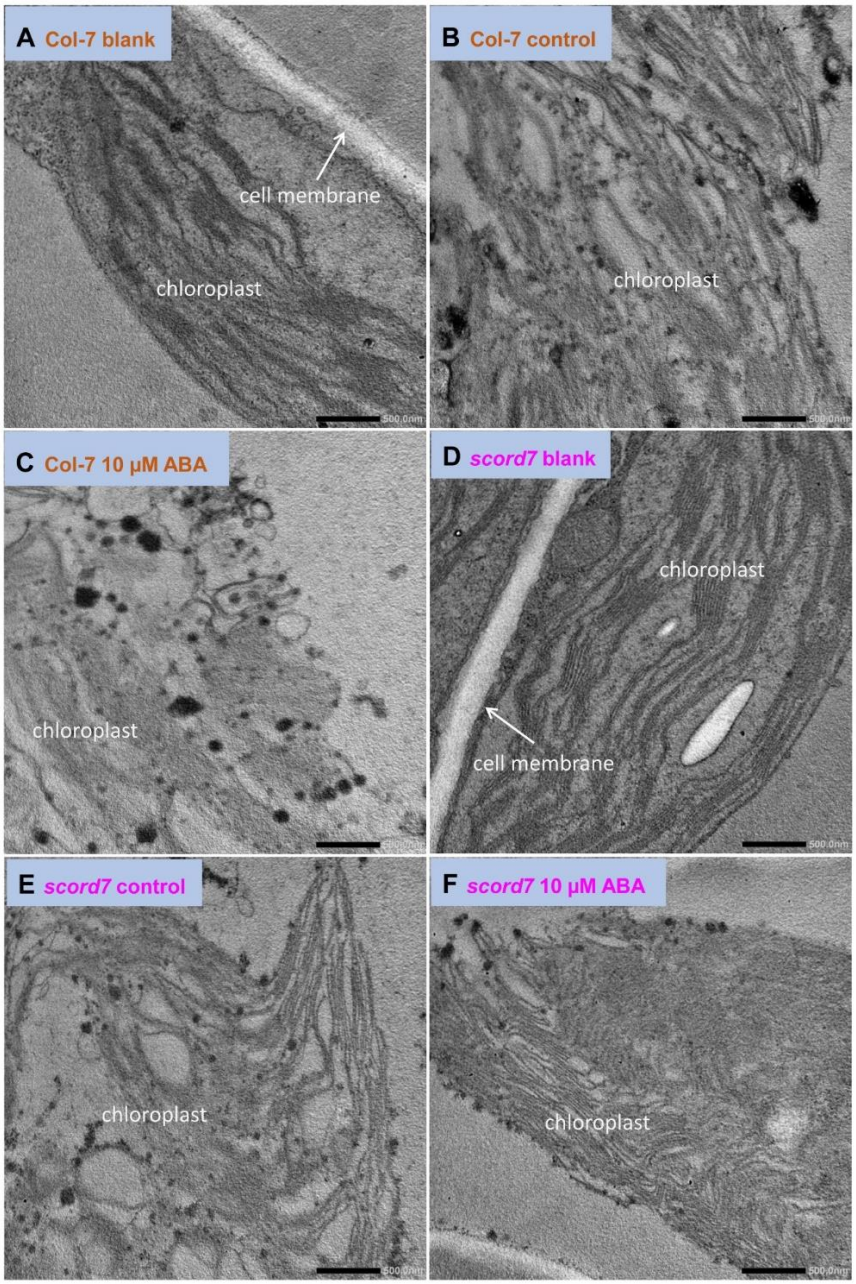

Figure C6. Subcellular TEM images of the leaves of *Arabidopsis* Col-7 ecotype (A–C) and *scord7* mutant (D–F) after the sorption experiment (10 mg L^{-1} Ag NPs). Blank: no Ag NPs exposure; Control: opening buffer without abscisic acid (ABA) treatment for 1 h before 10 mg L^{-1} Ag NPs exposure; 10 µM ABA: opening buffer with 10 µM ABA treatment for 1 h before 10 mg L^{-1} Ag NPs exposure. The scale bar is 500 nm. It is difficult to identify any possible Ag NPs in the chloroplasts because of noisy background.

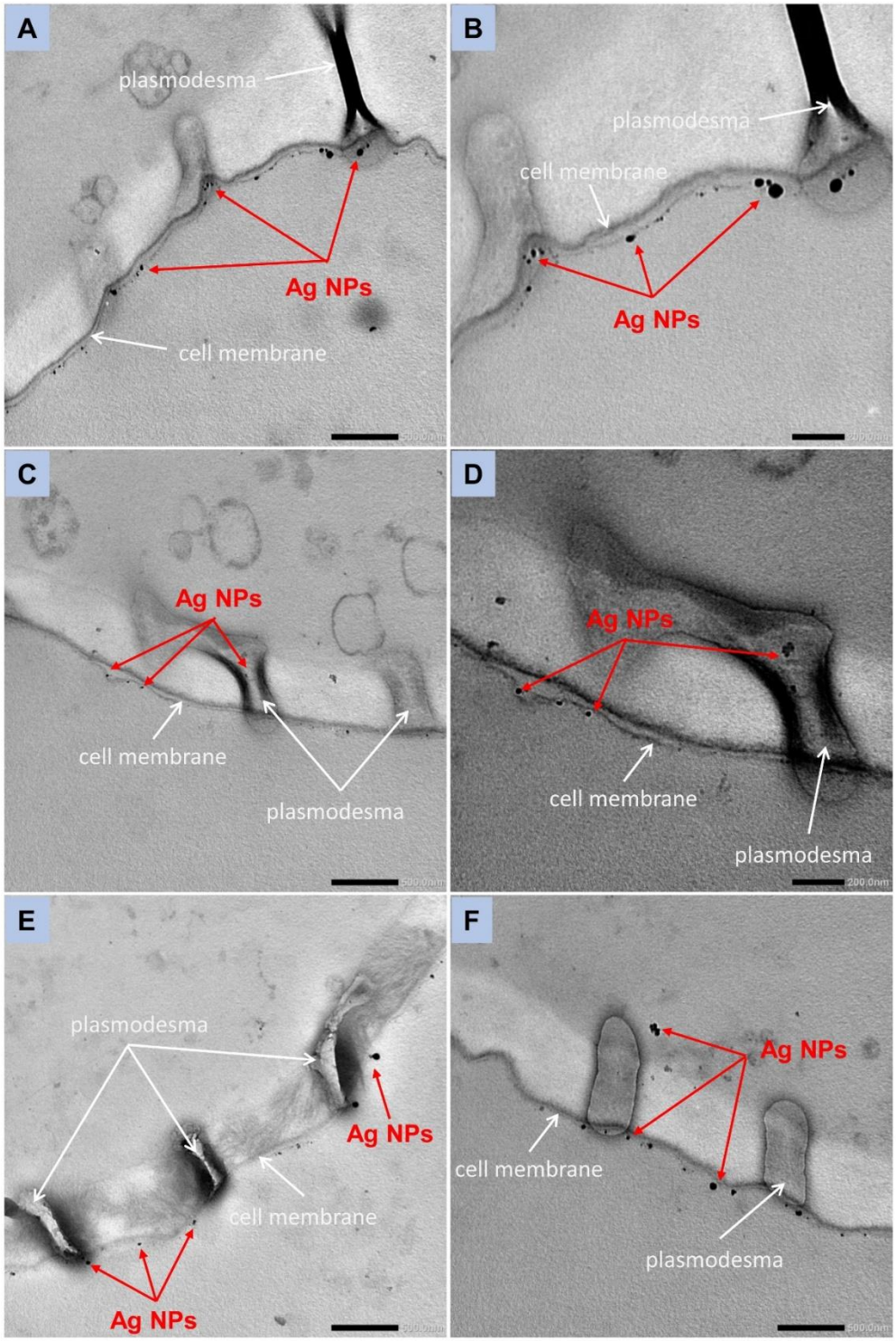

Figure C7. Subcellular TEM images of the leaves of *Arabidopsis* Col-7 after the sorption experiment (10 mg L^{-1} Ag NPs) in the control treatment (i.e., opening buffer without ABA for 1 h). The scale bars are 500 nm in A, C, E, F, and 200 nm for B and D.

Table C2. ***Ag NPs Sorption Kinetics Data***

Time (min)	Fresh leaves (g)		Concentration (C_e, mg L^{-1})		Sorbed amount (Q_e, mg kg^{-1})	
	Rep. 1	Rep. 2	Rep. 1	Rep. 2	Rep. 1	Rep. 2
initial concentration = 2.098 mg L^{-1}, volume = 25 mL						
5	0.41	0.40	1.95	1.91	9.12	11.50
10	0.42	0.43	1.77	1.78	19.26	18.45
20	0.43	0.44	1.69	1.67	23.73	24.65
40	0.41	0.41	1.59	1.57	30.78	32.22
60	0.40	0.41	1.56	1.58	33.27	31.93
90	0.42	0.42	1.57	1.59	31.64	30.64
120	0.41	0.41	1.63	1.64	28.70	27.97

Table C3. ***Ag NPs Sorption Equilibrium Data***

Plants	Ag NPs exposure	Treatments	Replicates	Fresh leaves (g)	Concentration (C_0, mg L^{-1})	Concentration (C_e, mg L^{-1})	Sorbed amount (Q_e, mg kg^{-1})
Ler	1 mg L^{-1}	control	1	0.4526	1.25	0.41	46.25
		control	2	0.4642	1.25	0.50	40.25
		control	3	0.4560	1.25	0.73	28.36
		10 µM ABA	1	0.4679	1.25	1.07	9.69
		10 µM ABA	2	0.4580	1.25	1.15	5.31
		10 µM ABA	3	0.4539	1.25	1.23	1.29
	5 mg L^{-1}	control	1	0.4555	4.55	2.38	118.90
		control	2	0.4677	4.55	2.28	120.93
		control	3	0.4653	4.55	2.05	133.91
		10 µM ABA	1	0.4578	4.55	2.72	99.52
		10 µM ABA	2	0.4475	4.55	3.01	85.94
		10 µM ABA	3	0.4624	4.55	2.66	102.20
	10 mg L^{-1}	control	1	0.4690	9.38	6.07	176.24
		control	2	0.4637	9.38	5.80	193.14
		control	3	0.4627	9.38	6.56	152.49
		10 µM ABA	1	0.4778	9.38	8.42	50.14
		10 µM ABA	2	0.4599	9.38	8.06	71.56
		10 µM ABA	3	0.4631	9.38	8.04	72.36

Table C3 (cont'd)

		control	1	0.4940	1.25	0.67	29.22
		control	2	0.4890	1.25	0.85	20.62
		control	3	0.4540	1.25	0.75	27.61
	1 mg L^{-1}	10 µM ABA	1	0.4530	1.25	0.87	21.27
		10 µM ABA	2	0.4630	1.25	0.85	21.89
		10 µM ABA	3	0.4870	1.25	0.87	19.78
		control	1	0.4800	4.55	2.79	91.58
		control	2	0.4660	4.55	2.07	132.74
		control	3	0.4590	4.55	2.07	134.66
ost1-2	5 mg L^{-1}	10 µM ABA	1	0.4540	4.55	2.51	112.35
		10 µM ABA	2	0.4520	4.55	2.26	126.24
		10 µM ABA	3	0.4810	4.55	2.30	116.96
		control	1	0.5747	14.6	10.22	194.70
		control	2	0.6063	14.6	10.20	185.40
		control	3	0.6053	14.6	9.83	200.96
	10 mg L^{-1}	10 µM ABA	1	0.5499	14.6	10.21	203.76
		10 µM ABA	2	0.5662	14.6	9.83	214.95
		10 µM ABA	3	0.6015	14.6	10.47	175.73

Table C3 (cont'd)

Col-7	1 mg L^{-1}	control	1	0.4581	1.81	1.16	35.65
		control	2	0.4606	1.81	1.25	30.25
		control	3	0.4527	1.81	1.23	32.32
		10 µM ABA	1	0.4692	1.81	1.26	29.16
		10 µM ABA	2	0.4701	1.81	1.29	27.62
		10 µM ABA	3	0.4615	1.81	1.30	27.48
	5 mg L^{-1}	control	1	0.4581	6.86	5.41	78.73
		control	2	0.4723	6.86	5.15	90.23
		control	3	0.4768	6.86	5.27	83.30
		10 µM ABA	1	0.4697	6.86	5.57	68.70
		10 µM ABA	2	0.4642	6.86	5.59	68.22
		10 µM ABA	3	0.4766	6.86	5.68	61.62
	10 mg L^{-1}	control	1	0.4292	12.0	8.45	207.52
		control	2	0.4272	12.0	8.97	177.71
		control	3	0.4295	12.0	9.37	153.71
		10 µM ABA	1	0.4462	12.0	9.27	153.56
		10 µM ABA	2	0.4539	12.0	9.72	126.28
		10 µM ABA	3	0.4618	12.0	8.90	168.18

Table C3 (cont'd)

		control	1	0.4292	1.44	0.53	52.89
		control	2	0.4315	1.44	0.50	54.34
		control	3	0.4164	1.44	0.56	52.96
	1 mg L^{-1}	10 µM ABA	1	0.4378	1.44	0.56	50.03
		10 µM ABA	2	0.4449	1.44	0.60	47.43
		10 µM ABA	3	0.4399	1.44	0.62	46.72
		control	1	0.4623	4.86	3.85	54.30
		control	2	0.4447	4.86	3.46	78.71
scord7	5 mg L^{-1}	control	3	0.4566	4.86	3.52	73.37
		10 µM ABA	1	0.4369	4.86	3.32	87.67
		10 µM ABA	2	0.4334	4.86	3.41	83.52
		10 µM ABA	3	0.4368	4.86	3.51	76.81
		control	1	0.5637	14.6	9.67	222.65
		control	2	0.5626	14.6	9.75	219.65
	10 mg L^{-1}	control	3	0.5615	14.6	9.54	229.50
		10 µM ABA	1	0.5373	14.6	9.85	225.24
		10 µM ABA	2	0.5304	14.6	10.05	218.91
		10 µM ABA	3	0.5442	14.6	9.93	218.99

REFERENCES

REFERENCES

1. Buzea, C.; Pacheco, I. I.; Robbie, K., Nanomaterials and nanoparticles: Sources and toxicity. *Biointerphases* **2007,** *2*, (4), MR17-MR71.

2. Hochella, M. F.; Mogk, D. W.; Ranville, J.; Allen, I. C.; Luther, G. W.; Marr, L. C.; McGrail, B. P.; Murayama, M.; Qafoku, N. P.; Rosso, K. M.; Sahai, N.; Schroeder, P. A.; Vikesland, P.; Westerhoff, P.; Yang, Y., Natural, incidental, and engineered nanomaterials and their impacts on the Earth system. *Science* **2019,** *363*, (6434), eaau8299.

3. Roco, M. C., Overview: Affirmation of nanotechnology between 2000 and 2030. *Nanotechnology Commercialization: Manufacturing Processes and Products* **2017**, 1-23.

4. Roco, M. C., The long view of nanotechnology development: the National Nanotechnology Initiative at 10 years. *Journal of Nanoparticle Research* **2011,** *13*, (2), 427-445.

5. Vance, M. E.; Kuiken, T.; Vejerano, E. P.; McGinnis, S. P.; Hochella Jr, M. F.; Rejeski, D.; Hull, M. S., Nanotechnology in the real world: Redeveloping the nanomaterial consumer products inventory. *Beilstein Journal of Nanotechnology* **2015,** *6*, 1769.

6. Montgomery, M. A.; Elimelech, M., Water and sanitation in developing countries: including health in the equation. In Environmental Science & Technology: 2007; Vol. 41, pp 17-24.

7. Shannon, M. A.; Bohn, P. W.; Elimelech, M.; Georgiadis, J. G.; Marinas, B. J.; Mayes, A. M., Science and technology for water purification in the coming decades. *Nature* **2008,** *452*, (7185), 301-310.

8. Kümmerer, K., Antibiotics in the aquatic environment – A review – Part I. *Chemosphere* **2009,** *75*, (4), 417-434.

9. Balakrishna, K.; Rath, A.; Praveenkumarreddy, Y.; Guruge, K. S.; Subedi, B., A review of the occurrence of pharmaceuticals and personal care products in Indian water bodies. *Ecotoxicology and Environmental Safety* **2017,** *137*, 113-120.

10. Patel, M.; Kumar, R.; Kishor, K.; Mlsna, T.; Pittman, C. U.; Mohan, D., Pharmaceuticals of emerging concern in aquatic systems: Chemistry, occurrence, effects, and removal methods. *Chemical Reviews* **2019,** *119*, (6), 3510-3673.

11. Wang, A.; Hu, X.; Wan, Y.; Mahai, G.; Jiang, Y.; Huo, W.; Zhao, X.; Liang, G.; He, Z.; Xia, W.; Xu, S., A nationwide study of the occurrence and distribution of atrazine and its degradates in tap water and groundwater in China: Assessment of human exposure potential. *Chemosphere* **2020,** *252*, 126533.

12. Li, S.; Wen, J.; He, B.; Wang, J.; Hu, X.; Liu, J., Occurrence of caffeine in the freshwater environment: Implications for ecopharmacovigilance. *Environmental Pollution* **2020,** *263*, 114371.

13. Li, Y.; Ding, J.; Zhang, L.; Liu, X.; Wang, G., Occurrence and ranking of pharmaceuticals in the major rivers of China. *Science of The Total Environment* **2019,** *696*, 133991.

14. Halling-Sørensen, B.; Nors Nielsen, S.; Lanzky, P. F.; Ingerslev, F.; Holten Lützhøft, H. C.; Jørgensen, S. E., Occurrence, fate and effects of pharmaceutical substances in the environment-A review. *Chemosphere* **1998,** *36*, (2), 357-393.

15. Gulkowska, A.; He, Y.; So, M. K.; Yeung, L. W. Y.; Leung, H. W.; Giesy, J. P.; Lam, P. K. S.; Martin, M.; Richardson, B. J., The occurrence of selected antibiotics in Hong Kong coastal waters. *Marine Pollution Bulletin* **2007,** *54*, (8), 1287-1293.

16. Watkinson, A. J.; Murby, E. J.; Kolpin, D. W.; Costanzo, S. D., The occurrence of antibiotics in an urban watershed: From wastewater to drinking water. *Science of The Total Environment* **2009,** *407*, (8), 2711-2723.

17. Oulton, R. L.; Kohn, T.; Cwiertny, D. M., Pharmaceuticals and personal care products in effluent matrices: A survey of transformation and removal during wastewater treatment and implications for wastewater management. *Journal of Environmental Monitoring* **2010,** *12*, (11), 1956-1978.

18. Zhang, H.; Liu, P.; Feng, Y.; Yang, F., Fate of antibiotics during wastewater treatment and antibiotic distribution in the effluent-receiving waters of the Yellow Sea, northern China. *Marine Pollution Bulletin* **2013,** *73*, (1), 282-290.

19. Gulkowska, A.; Leung, H. W.; So, M. K.; Taniyasu, S.; Yamashita, N.; Yeung, L. W. Y.; Richardson, B. J.; Lei, A. P.; Giesy, J. P.; Lam, P. K. S., Removal of antibiotics from wastewater by sewage treatment facilities in Hong Kong and Shenzhen, China. *Water Research* **2008,** *42*, (1), 395-403.

20. Berglund, B., Environmental dissemination of antibiotic resistance genes and correlation to anthropogenic contamination with antibiotics. *Infection Ecology & Epidemiology* **2015,** *5*, (1), 28564.

21. Quoc Tuc, D.; Elodie, M.-G.; Pierre, L.; Fabrice, A.; Marie-Jeanne, T.; Martine, B.; Joelle, E.; Marc, C., Fate of antibiotics from hospital and domestic sources in a sewage network. *Science of The Total Environment* **2017,** *575*, 758-766.

22. Zhao, L.; Deng, J.; Sun, P.; Liu, J.; Ji, Y.; Nakada, N.; Qiao, Z.; Tanaka, H.; Yang, Y., Nanomaterials for treating emerging contaminants in water by adsorption and photocatalysis: Systematic review and bibliometric analysis. *Science of The Total Environment* **2018,** *627*, 1253-1263.

23. Li, S.; Shi, W.; Liu, W.; Li, H.; Zhang, W.; Hu, J.; Ke, Y.; Sun, W.; Ni, J., A duodecennial national synthesis of antibiotics in China's major rivers and seas (2005–2016). *Science of The Total Environment* **2018,** *615*, 906-917.

24. Boxall, A. B. A.; Kolpin, D. W.; Halling-Sørensen, B.; Tolls, J., Peer reviewed: Are veterinary medicines causing environmental risks? *Environmental Science & Technology* **2003,** *37*, (15), 286A-294A.

25. Hyland, K. C.; Blaine, A. C.; Dickenson, E. R.; Higgins, C. P., Accumulation of contaminants of emerging concern in food crops—part 1: Edible strawberries and lettuce grown in reclaimed water. *Environmental Toxicology and Chemistry* **2015a,** *34*, (10), 2213-2221.

26. Hyland, K. C.; Blaine, A. C.; Higgins, C. P., Accumulation of contaminants of emerging concern in food crops—part 2: Plant distribution. *Environmental Toxicology and Chemistry* **2015b,** *34*, (10), 2222-2230.

27. Goldstein, M.; Shenker, M.; Chefetz, B., Insights into the uptake processes of wastewater-borne pharmaceuticals by vegetables. *Environmental Science & Technology* **2014,** *48*, (10), 5593-5600.

28. Aryal, N.; Reinhold, D. M., Phytoaccumulation of antimicrobials from biosolids: Impacts on environmental fate and relevance to human exposure. *Water Research* **2011,** *45*, (17), 5545-5552.

29. Paltiel, O.; Fedorova, G.; Tadmor, G.; Kleinstern, G.; Maor, Y.; Chefetz, B., Human exposure to wastewater-derived pharmaceuticals in fresh produce: A randomized controlled trial focusing on carbamazepine. *Environmental Science & Technology* **2016,** *50*, (8), 4476-4482.

30. Liu, X.; Ma, C.; Yan, Y.; Yao, G.; Tang, Y.; Huo, P.; Shi, W.; Yan, Y., Hydrothermal synthesis of CdSe quantum dots and their photocatalytic activity on degradation of cefalexin. *Industrial & Engineering Chemistry Research* **2013,** *52*, (43), 15015-15023.

31. Torki, F.; Faghihian, H., Photocatalytic activity of NiS, NiO and coupled NiS–NiO for degradation of pharmaceutical pollutant cephalexin under visible light. *RSC Advances* **2017,** *7*, (86), 54651-54661.

32. Song, Y.; Tian, J.; Gao, S.; Shao, P.; Qi, J.; Cui, F., Photodegradation of sulfonamides by g-C_3N_4 under visible light irradiation: Effectiveness, mechanism and pathways. *Applied Catalysis B: Environmental* **2017,** *210*, (Supplement C), 88-96.

33. Elmolla, E. S.; Chaudhuri, M., Degradation of amoxicillin, ampicillin and cloxacillin antibiotics in aqueous solution by the UV/ZnO photocatalytic process. *Journal of Hazardous Materials* **2010,** *173*, (1), 445-449.

34. Guo, Y.; Dai, Y.; Zhao, W.; Li, H.; Xu, B.; Sun, C., Highly efficient photocatalytic degradation of naphthalene by $Co_3O_4/Bi_2O_2CO_3$ under visible light: A novel p–n heterojunction nanocomposite with nanocrystals/lotus-leaf-like nanosheets structure. *Applied Catalysis B: Environmental* **2018,** *237*, 273-287.

35. Loeb, S. K.; Alvarez, P. J. J.; Brame, J. A.; Cates, E. L.; Choi, W.; Crittenden, J.; Dionysiou, D. D.; Li, Q.; Li-Puma, G.; Quan, X.; Sedlak, D. L.; David Waite, T.; Westerhoff, P.; Kim, J.-H., The technology horizon for photocatalytic water treatment: Sunrise or sunset? *Environmental Science & Technology* **2019,** *53*, (6), 2937-2947.

36. Hu, L.; Flanders, P. M.; Miller, P. L.; Strathmann, T. J., Oxidation of sulfamethoxazole and related antimicrobial agents by TiO_2 photocatalysis. *Water Research* **2007,** *41*, (12), 2612-2626.

37. Yang, X.; Liu, X.; Zhang, A.; Lu, D.; Li, G.; Zhang, Q.; Liu, Q.; Jiang, G., Distinguishing the sources of silica nanoparticles by dual isotopic fingerprinting and machine learning. *Nature Communications* **2019,** *10*, (1), 1620.

38. Guinée, J. B.; Heijungs, R.; Vijver, M. G.; Peijnenburg, W. J. G. M., Setting the stage for debating the roles of risk assessment and life-cycle assessment of engineered nanomaterials. *Nature Nanotechnology* **2017,** *12*, 727.

39. Stander, L.; Theodore, L., Environmental implications of nanotechnology—an update. *International journal of environmental research and public health* **2011,** *8*, (2), 470-479.

40. NRC, *A research strategy for environmental, health, and safety aspects of engineered nanomaterials*. National Research Council (NRC), National Academies Press: 2012.

41. Kah, M.; Hofmann, T., Nanopesticide research: Current trends and future priorities. *Environment International* **2014,** *63*, 224-235.

42. Gottschalk, F.; Nowack, B., The release of engineered nanomaterials to the environment. *Journal of Environmental Monitoring* **2011,** *13*, (5), 1145-1155.

43. Benn, T. M.; Westerhoff, P., Nanoparticle silver released into water from commercially available sock fabrics. *Environmental Science & Technology* **2008,** *42*, (11), 4133-4139.

44. Kaegi, R.; Ulrich, A.; Sinnet, B.; Vonbank, R.; Wichser, A.; Zuleeg, S.; Simmler, H.; Brunner, S.; Vonmont, H.; Burkhardt, M.; Boller, M., Synthetic TiO_2 nanoparticle emission from exterior facades into the aquatic environment. *Environmental Pollution* **2008,** *156*, (2), 233-239.

45. Mitrano, D. M.; Lesher, E. K.; Bednar, A.; Monserud, J.; Higgins, C. P.; Ranville, J. F., Detecting nanoparticulate silver using single-particle inductively coupled plasma–mass spectrometry. *Environmental Toxicology and Chemistry* **2012,** *31*, (1), 115-121.

46. Gottschalk, F.; Sonderer, T.; Scholz, R. W.; Nowack, B., Modeled environmental concentrations of engineered nanomaterials (TiO_2, ZnO, Ag, CNT, Fullerenes) for different regions. *Environmental Science & Technology* **2009,** *43*, (24), 9216-9222.

47. Mueller, N. C.; Nowack, B., Exposure modeling of engineered nanoparticles in the environment. *Environmental Science & Technology* **2008,** *42*, (12), 4447-4453.

48. Gardea-Torresdey, J. L.; Rico, C. M.; White, J. C., Trophic transfer, transformation, and impact of engineered nanomaterials in terrestrial environments. *Environmental Science & Technology* **2014,** *48*, (5), 2526-2540.

49. Larue, C.; Castillo-Michel, H.; Sobanska, S.; Cécillon, L.; Bureau, S.; Barthès, V.; Ouerdane, L.; Carrière, M.; Sarret, G., Foliar exposure of the crop Lactuca sativa to silver nanoparticles: Evidence for internalization and changes in Ag speciation. *Journal of Hazardous Materials* **2014,** *264*, 98-106.

50. Chavez Soria, N. G.; Montes, A.; Bisson, M. A.; Atilla-Gokcumen, G. E.; Aga, D. S., Mass spectrometry-based metabolomics to assess uptake of silver nanoparticles by *Arabidopsis thaliana*. *Environmental Science: Nano* **2017,** *4*, (10), 1944-1953.

51. Cvjetko, P.; Zovko, M.; Štefanić, P. P.; Biba, R.; Tkalec, M.; Domijan, A.-M.; Vrček, I. V.; Letofsky-Papst, I.; Šikić, S.; Balen, B., Phytotoxic effects of silver nanoparticles in tobacco plants. *Environmental Science and Pollution Research* **2018,** *25*, (6), 5590-5602.

52. Doolette, C. L.; McLaughlin, M. J.; Kirby, J. K.; Navarro, D. A., Bioavailability of silver and silver sulfide nanoparticles to lettuce (*Lactuca sativa*): Effect of agricultural amendments on plant uptake. *Journal of Hazardous Materials* **2015,** *300*, 788-795.

53. Fernandes, J. P.; Mucha, A. P.; Francisco, T.; Gomes, C. R.; Almeida, C. M. R., Silver nanoparticles uptake by salt marsh plants – Implications for phytoremediation processes and effects in microbial community dynamics. *Marine Pollution Bulletin* **2017,** *119*, (1), 176-183.

54. Nath, J.; Dror, I.; Landa, P.; Vanek, T.; Kaplan-Ashiri, I.; Berkowitz, B., Synthesis and characterization of isotopically-labeled silver, copper and zinc oxide nanoparticles for tracing studies in plants. *Environmental Pollution* **2018,** *242*, 1827-1837.

55. Pappas, S. A.; Turaga, U.; Kumar, N.; Ramkumar, S.; Kendall, R. J., Uptake of silver from polyvinylpyrrolidine coated silver nanoparticles in a terrestrial system. *International Journal of Environmental & Agriculture Research* **2017,** *3*, 104-114.

56. Vinković, T.; Novák, O.; Strnad, M.; Goessler, W.; Jurašin, D. D.; Parađiković, N.; Vrček, I. V., Cytokinin response in pepper plants (*Capsicum annuum* L.) exposed to silver nanoparticles. *Environmental Research* **2017,** *156*, 10-18.

57. Zhang, W.-Y.; Wang, Q.; Li, M.; Dang, F.; Zhou, D.-M., Nonselective uptake of silver and gold nanoparticles by wheat. *Nanotoxicology* **2019,** *13*, (8), 1073-1086.

58. Lee, W.-M.; An, Y.-J.; Yoon, H.; Kweon, H.-S., Toxicity and bioavailability of copper nanoparticles to the terrestrial plants mung bean (*Phaseolus radiatus*) and wheat (*Triticum aestivum*): Plant agar test for water-insoluble nanoparticles. *Environmental Toxicology and Chemistry* **2008,** *27*, (9), 1915-1921.

59. Zhao, L.; Peralta-Videa, J. R.; Varela-Ramirez, A.; Castillo-Michel, H.; Li, C.; Zhang, J.; Aguilera, R. J.; Keller, A. A.; Gardea-Torresdey, J. L., Effect of surface coating and organic matter on the uptake of CeO_2 NPs by corn plants grown in soil: Insight into the uptake mechanism. *Journal of Hazardous Materials* **2012,** *225-226*, 131-138.

60. Sattelmacher, B., The apoplast and its significance for plant mineral nutrition. *New Phytologist* **2001,** *149*, (2), 167-192.

61. Roberts, A. G.; Oparka, K. J., Plasmodesmata and the control of symplastic transport. *Plant, Cell & Environment* **2003,** *26*, (1), 103-124.

62. Pérez-de-Luque, A., Interaction of nanomaterials with plants: what do we need for real applications in agriculture? *Frontiers in Environmental Science* **2017,** *5*, (12).

63. Lin, D.; Xing, B., Root uptake and phytotoxicity of ZnO nanoparticles. *Environmental Science & Technology* **2008,** *42*, (15), 5580-5585.

64. Lv, J.; Christie, P.; Zhang, S., Uptake, translocation, and transformation of metal-based nanoparticles in plants: Recent advances and methodological challenges. *Environmental Science: Nano* **2019,** *6*, (1), 41-59.

65. Ma, X.; Geiser-Lee, J.; Deng, Y.; Kolmakov, A., Interactions between engineered nanoparticles (ENPs) and plants: Phytotoxicity, uptake and accumulation. *Science of The Total Environment* **2010,** *408*, (16), 3053-3061.

66. Su, Y.; Ashworth, V.; Kim, C.; Adeleye, A. S.; Rolshausen, P.; Roper, C.; White, J.; Jassby, D., Delivery, uptake, fate, and transport of engineered nanoparticles in plants: A critical review and data analysis. *Environmental Science: Nano* **2019,** *6*, (8), 2311-2331.

67. Lv, J.; Zhang, S.; Luo, L.; Zhang, J.; Yang, K.; Christie, P., Accumulation, speciation and uptake pathway of ZnO nanoparticles in maize. *Environmental Science: Nano* **2015,** *2*, (1), 68-77.

68. Kurepa, J.; Paunesku, T.; Vogt, S.; Arora, H.; Rabatic, B. M.; Lu, J.; Wanzer, M. B.; Woloschak, G. E.; Smalle, J. A., Uptake and distribution of ultrasmall anatase TiO_2 alizarin red S nanoconjugates in *Arabidopsis thaliana*. *Nano Letters* **2010,** *10*, (7), 2296-2302.

69. Liu, Q.; Chen, B.; Wang, Q.; Shi, X.; Xiao, Z.; Lin, J.; Fang, X., Carbon nanotubes as molecular transporters for walled plant cells. *Nano Letters* **2009,** *9*, (3), 1007-1010.

70. Navarro, E.; Baun, A.; Behra, R.; Hartmann, N. B.; Filser, J.; Miao, A.-J.; Quigg, A.; Santschi, P. H.; Sigg, L., Environmental behavior and ecotoxicity of engineered nanoparticles to algae, plants, and fungi. *Ecotoxicology* **2008,** *17*, (5), 372-386.

71. Abbas, Q.; Liu, G.; Yousaf, B.; Ali, M. U.; Ullah, H.; Ahmed, R., Effects of biochar on uptake, acquisition and translocation of silver nanoparticles in rice (*Oryza sativa* L.) in relation to growth, photosynthetic traits and nutrients displacement. *Environmental Pollution* **2019,** *250*, 728-736.

72. Hu, B.; Ai, Y.; Jin, J.; Hayat, T.; Alsaedi, A.; Zhuang, L.; Wang, X., Efficient elimination of organic and inorganic pollutants by biochar and biochar-based materials. *Biochar* **2020,** *2*, (1), 47-64.

73. Servin, A. D.; De la Torre-Roche, R.; Castillo-Michel, H.; Pagano, L.; Hawthorne, J.; Musante, C.; Pignatello, J.; Uchimiya, M.; White, J. C., Exposure of agricultural crops to nanoparticle CeO_2 in biochar-amended soil. *Plant Physiology and Biochemistry* **2017,** *110*, 147-157.

74. Sima, X.-F.; Shen, X.-C.; Fang, T.; Yu, H.-Q.; Jiang, H., Efficiently reducing the plant growth inhibition of CuO NPs using rice husk-derived biochar: Experimental demonstration and mechanism investigation. *Environmental Science: Nano* **2017,** *4*, (8), 1722-1732.

75. Bergeson, L. L., Nanosilver pesticide products: What does the future hold? *Environmental Quality Management* **2010,** *19*, (4), 73-82.

76. Gogos, A.; Knauer, K.; Bucheli, T. D., Nanomaterials in plant protection and fertilization: Current state, foreseen applications, and research priorities. *Journal of Agricultural and Food Chemistry* **2012,** *60*, (39), 9781-9792.

77. Kah, M.; Beulke, S.; Tiede, K.; Hofmann, T., Nanopesticides: State of knowledge, environmental fate, and exposure modelling. *Critical Reviews in Environmental Science and Technology* **2013,** *43*, (16), 1823-1867.

78. Jung, J.-H.; Kim, S.-W.; Min, J.-S.; Kim, Y.-J.; Lamsal, K.; Kim, K. S.; Lee, Y. S., The effect of nano-silver liquid against the white rot of the green onion caused by *Sclerotium cepivorum*. *Mycobiology* **2010,** *38*, (1), 39-45.

79. Lu, J.; Li, F.; Guo, T.; Lin, L.; Hou, M.; Liu, T., TiO_2 photocatalytic antifungal technique for crops diseases control. *Journal of Environmental Sciences* **2006,** *18*, (2), 397-401.

80. Prado, A. G. S.; Moura, A. O.; Nunes, A. R., Nanosized silica modified with carboxylic acid as support for controlled release of herbicides. *Journal of Agricultural and Food Chemistry* **2011,** *59*, (16), 8847-8852.

81. Rondeau-Mouro, C.; Defer, D.; Leboeuf, E.; Lahaye, M., Assessment of cell wall porosity in *Arabidopsis thaliana* by NMR spectroscopy. *International Journal of Biological Macromolecules* **2008,** *42*, (2), 83-92.

82. Eichert, T.; Kurtz, A.; Steiner, U.; Goldbach, H. E., Size exclusion limits and lateral heterogeneity of the stomatal foliar uptake pathway for aqueous solutes and water-suspended nanoparticles. *Physiologia Plantarum* **2008,** *134*, (1), 151-160.

83. Chuang, Y.-H.; Zhang, Y.; Zhang, W.; Boyd, S. A.; Li, H., Comparison of accelerated solvent extraction and quick, easy, cheap, effective, rugged and safe method for extraction and determination of pharmaceuticals in vegetables. *Journal of Chromatography A* **2015,** *1404*, 1-9.

84. Kookana, R. S.; Williams, M.; Boxall, A. B. A.; Larsson, D. G. J.; Gaw, S.; Choi, K.; Yamamoto, H.; Thatikonda, S.; Zhu, Y.-G.; Carriquiriborde, P., Potential ecological footprints of active pharmaceutical ingredients: an examination of risk factors in low-, middle- and high-income countries. *Philosophical Transactions of the Royal Society B: Biological Sciences* **2014,** *369*, (1656), 20130586.

85. Williams-Nguyen, J.; Sallach, J. B.; Bartelt-Hunt, S.; Boxall, A. B.; Durso, L. M.; McLain, J. E.; Singer, R. S.; Snow, D. D.; Zilles, J. L., Antibiotics and antibiotic resistance in agroecosystems: State of the science. *Journal of Environmental Quality* **2016,** *45*, (2), 394-406.

86. Zhu, Y.-G.; Zhao, Y.; Li, B.; Huang, C.-L.; Zhang, S.-Y.; Yu, S.; Chen, Y.-S.; Zhang, T.; Gillings, M. R.; Su, J.-Q., Continental-scale pollution of estuaries with antibiotic resistance genes. *Nature Microbiology* **2017,** *2*, 16270.

87. Gullberg, E.; Cao, S.; Berg, O. G.; Ilbäck, C.; Sandegren, L.; Hughes, D.; Andersson, D. I., Selection of resistant bacteria at very low antibiotic concentrations. *PLoS pathogens* **2011,** *7*, (7), e1002158.

88. Prosser, R. S.; Sibley, P. K., Human health risk assessment of pharmaceuticals and personal care products in plant tissue due to biosolids and manure amendments, and wastewater irrigation. *Environment International* **2015,** *75*, 223-233.

89. Minh, T. B.; Leung, H. W.; Loi, I. H.; Chan, W. H.; So, M. K.; Mao, J. Q.; Choi, D.; Lam, J. C. W.; Zheng, G.; Martin, M.; Lee, J. H. W.; Lam, P. K. S.; Richardson, B. J., Antibiotics in the Hong Kong metropolitan area: Ubiquitous distribution and fate in Victoria Harbour. *Marine Pollution Bulletin* **2009,** *58*, (7), 1052-1062.

90. Sakthivel, S.; Neppolian, B.; Shankar, M. V.; Arabindoo, B.; Palanichamy, M.; Murugesan, V., Solar photocatalytic degradation of azo dye: comparison of photocatalytic efficiency of ZnO and TiO_2. *Solar Energy Materials and Solar Cells* **2003,** *77*, (1), 65-82.

91. Lee, K. M.; Lai, C. W.; Ngai, K. S.; Juan, J. C., Recent developments of zinc oxide based photocatalyst in water treatment technology: A review. *Water Research* **2016,** *88*, (Supplement C), 428-448.

92. Schmidt-Mende, L.; MacManus-Driscoll, J. L., ZnO – nanostructures, defects, and devices. *Materials Today* **2007,** *10*, (5), 40-48.

93. Bitenc, M.; Horvat, B.; Likozar, B.; Dražić, G.; Orel, Z. C., The impact of ZnO load, stability and morphology on the kinetics of the photocatalytic degradation of caffeine and resazurin. *Applied Catalysis B: Environmental* **2013,** *136-137*, 202-209.

94. Choina, J.; Bagabas, A.; Fischer, C.; Flechsig, G. U.; Kosslick, H.; Alshammari, A.; Schulz, A., The influence of the textural properties of ZnO nanoparticles on adsorption and photocatalytic remediation of water from pharmaceuticals. *Catalysis Today* **2015,** *241*, 47-54.

95. Ko, F.-H.; Lo, W.-J.; Chang, Y.-C.; Guo, J.-Y.; Chen, C.-M., ZnO nanowires coated stainless steel meshes as hierarchical photocatalysts for catalytic photodegradation of four kinds of organic pollutants. *Journal of Alloys and Compounds* **2016,** *678*, (Supplement C), 137-146.

96. Kuo, T.-J.; Lin, C.-N.; Kuo, C.-L.; Huang, M. H., Growth of ultralong ZnO nanowires on silicon substrates by vapor transport and their use as recyclable photocatalysts. *Chemistry of Materials* **2007,** *19*, (21), 5143-5147.

97. Tian, Z. R.; Voigt, J. A.; Liu, J.; McKenzie, B.; McDermott, M. J.; Rodriguez, M. A.; Konishi, H.; Xu, H., Complex and oriented ZnO nanostructures. *Nature Materials* **2003,** *2*, 821.

98. Mirzaei, A.; Chen, Z.; Haghighat, F.; Yerushalmi, L., Removal of pharmaceuticals and endocrine disrupting compounds from water by zinc oxide-based photocatalytic degradation: A review. *Sustainable Cities and Society* **2016,** *27*, 407-418.

99. Wan, Q.; Wang, T. H.; Zhao, J. C., Enhanced photocatalytic activity of ZnO nanotetrapods. *Applied Physics Letters* **2005,** *87*, (8), 083105.

100. Yang, J. L.; An, S. J.; Park, W. I.; Yi, G.-C.; Choi, W., Photocatalysis using ZnO thin films and nanoneedles grown by metal–organic chemical vapor deposition. *Advanced Materials* **2004,** *16*, (18), 1661-1664.

101. Zhang, Y.; Huang, X.; Yeom, J., A floatable piezo-photocatalytic platform based on semi-embedded ZnO nanowire array for high-performance water decontamination. *Nano-Micro Letters* **2019,** *11*, (1), 11.

102. Lu, M.-Y.; Tseng, Y.-T.; Chiu, C.-Y., Angle-dependent photodegradation over ZnO nanowire arrays on flexible paper substrates. *Nanoscale Research Letters* **2014,** *9*, (1), 667.

103. El Mragui, A.; Daou, I.; Zegaoui, O., Influence of the preparation method and $ZnO/(ZnO + TiO_2)$ weight ratio on the physicochemical and photocatalytic properties of $ZnO\text{-}TiO_2$ nanomaterials. *Catalysis Today* **2018**.

104. Chan, K. H.; Chu, W., Effect of humic acid on the photolysis of the pesticide atrazine in a surfactant-aided soil-washing system in acidic condition. *Water Research* **2005,** *39*, (10), 2154-2166.

105. Ismail, L.; Ferronato, C.; Fine, L.; Jaber, F.; Chovelon, J.-M., Effect of water constituents on the degradation of sulfaclozine in the three systems: UV/TiO_2, $UV/K_2S_2O_8$, and $UV/TiO_2/K_2S_2O_8$. *Environmental Science and Pollution Research* **2017**.

106. Yang, Y.; Jiang, J.; Lu, X.; Ma, J.; Liu, Y., Production of sulfate radical and hydroxyl radical by reaction of ozone with peroxymonosulfate: A novel advanced oxidation process. *Environmental Science & Technology* **2015,** *49*, (12), 7330-7339.

107. Yang, J.; Li, J.; Dong, W.; Ma, J.; Cao, J.; Li, T.; Li, J.; Gu, J.; Liu, P., Study on enhanced degradation of atrazine by ozonation in the presence of hydroxylamine. *Journal of Hazardous Materials* **2016,** *316*, (Supplement C), 110-121.

108. Zhao, Q.; Feng, L.; Cheng, X.; Chen, C.; Zhang, L., Photodegradation of amoxicillin in aqueous solution under simulated irradiation: influencing factors and mechanisms. *Water Science and Technology* **2013,** *67*, (7), 1605-1611.

109. Pacholski, C.; Kornowski, A.; Weller, H., Self-assembly of ZnO: from nanodots to nanorods. *Angewandte Chemie International Edition* **2002,** *41*, (7), 1188-1191.

110. Zhao, J.-H.; Liu, C.-J.; Lv, Z.-H., Photoluminescence of ZnO nanoparticles and nanorods. *Optik - International Journal for Light and Electron Optics* **2016,** *127*, (3), 1421-1423.

111. Birkigt, J.; Gilevska, T.; Ricken, B.; Richnow, H.-H.; Vione, D.; Corvini, P. F. X.; Nijenhuis, I.; Cichocka, D., Carbon stable isotope fractionation of sulfamethoxazole during biodegradation by *Microbacterium* sp. strain BR1 and upon direct photolysis. *Environmental Science & Technology* **2015,** *49*, (10), 6029-6036.

112. Méndez-Díaz, J. D.; Shimabuku, K. K.; Ma, J.; Enumah, Z. O.; Pignatello, J. J.; Mitch, W. A.; Dodd, M. C., Sunlight-driven photochemical halogenation of dissolved organic matter in seawater: A natural abiotic source of organobromine and organoiodine. *Environmental Science & Technology* **2014,** *48*, (13), 7418-7427.

113. Bansal, P.; Verma, A.; Aggarwal, K.; Singh, A.; Gupta, S., Investigations on the degradation of an antibiotic Cephalexin using suspended and supported TiO_2: Mineralization and durability studies. *The Canadian Journal of Chemical Engineering* **2016,** *94*, (7), 1269-1276.

114. Li, N.; Tian, Y.; Zhao, J.; Zhang, J.; Zuo, W.; Kong, L.; Cui, H., Z-scheme 2D/3D g-C_3N_4@ZnO with enhanced photocatalytic activity for cephalexin oxidation under solar light. *Chemical Engineering Journal* **2018,** *352*, 412-422.

115. Qian, Y.; Xue, G.; Chen, J.; Luo, J.; Zhou, X.; Gao, P.; Wang, Q., Oxidation of cefalexin by thermally activated persulfate: Kinetics, products, and antibacterial activity change. *Journal of Hazardous Materials* **2018,** *354*, 153-160.

116. Huang, Y.; Kong, M.; Westerman, D.; Xu, E. G.; Coffin, S.; Cochran, K. H.; Liu, Y.; Richardson, S. D.; Schlenk, D.; Dionysiou, D. D., Effects of HCO_3^- on degradation of toxic contaminants of emerging concern by UV/NO_3^-. *Environmental Science & Technology* **2018,** *52*, (21), 12697-12707.

117. Fang, H.; Gao, Y.; Li, G.; An, J.; Wong, P.-K.; Fu, H.; Yao, S.; Nie, X.; An, T., Advanced oxidation kinetics and mechanism of preservative propylparaben degradation in aqueous suspension of TiO_2 and risk assessment of its degradation products. *Environmental Science & Technology* **2013,** *47*, (6), 2704-2712.

118. Ye, L.; Liu, J.; Jiang, Z.; Peng, T.; Zan, L., Facets coupling of BiOBr-g-C_3N_4 composite photocatalyst for enhanced visible-light-driven photocatalytic activity. *Applied Catalysis B: Environmental* **2013,** *142-143*, 1-7.

119. Chuang, Y.-H.; Liu, C.-H.; Hammerschmidt, R.; Zhang, W.; Boyd, S. A.; Li, H., Metabolic demethylation and oxidation of caffeine during uptake by lettuce. *Journal of Agricultural and Food Chemistry* **2018,** *66*, (30), 7907-7915.

120. McLaren, A.; Valdes-Solis, T.; Li, G.; Tsang, S. C., Shape and size effects of ZnO nanocrystals on photocatalytic activity. *Journal of the American Chemical Society* **2009,** *131*, (35), 12540-12541.

121. Mohd Omar, F.; Abdul Aziz, H.; Stoll, S., Aggregation and disaggregation of ZnO nanoparticles: Influence of pH and adsorption of Suwannee River humic acid. *Science of The Total Environment* **2014,** *468-469*, 195-201.

122. Divband, B.; Khatamian, M.; Eslamian, G. R. K.; Darbandi, M., Synthesis of Ag/ZnO nanostructures by different methods and investigation of their photocatalytic efficiency for 4-nitrophenol degradation. *Applied Surface Science* **2013,** *284*, 80-86.

123. Eskandarloo, H.; Badiei, A.; Behnajady, M. A.; Ziarani, G. M., Ultrasonic-assisted degradation of phenazopyridine with a combination of Sm-doped ZnO nanoparticles and inorganic oxidants. *Ultrasonics Sonochemistry* **2016,** *28*, 169-177.

124. Ivetić, T. B.; Dimitrievska, M. R.; Finčur, N. L.; Đačanin, L. R.; Gúth, I. O.; Abramović, B. F.; Lukić-Petrović, S. R., Effect of annealing temperature on structural and optical properties of Mg-doped ZnO nanoparticles and their photocatalytic efficiency in alprazolam degradation. *Ceramics International* **2014,** *40*, (1, Part B), 1545-1552.

125. Li, Y.; Wang, Y.; Liu, L.; Wang, D.; Zhang, W., Ag/ZnO hollow sphere composites: Reusable photocatalyst for photocatalytic degradation of 17α-ethinylestradiol. *Environmental Science and Pollution Research* **2014,** *21*, (7), 5177-5186.

126. Sin, J.-C.; Lam, S.-M.; Lee, K.-T.; Mohamed, A. R., Degrading two endocrine-disrupting chemicals from water by UV irradiation with the presence of nanophotocatalysts. *Desalination and Water Treatment* **2013,** *51*, (16-18), 3505-3520.

127. Kozuch, S.; Martin, J. M. L., "Turning over" definitions in catalytic cycles. *ACS Catalysis* **2012,** *2*, (12), 2787-2794.

128. Stumm, W.; Morgan, J. J., *Aquatic chemistry: Chemical equilibria and rates in natural waters*. John Wiley & Sons: 2012; Vol. 126.

129. Zhang, W.; Li, Y.; Su, Y.; Mao, K.; Wang, Q., Effect of water composition on TiO_2 photocatalytic removal of endocrine disrupting compounds (EDCs) and estrogenic activity from secondary effluent. *Journal of Hazardous Materials* **2012,** *215-216*, (Supplement C), 252-258.

130. Guillard, C.; Puzenat, E.; Lachheb, H.; Houas, A.; Herrmann, J.-M., Why inorganic salts decrease the TiO_2 photocatalytic efficiency. *International Journal of Photoenergy* **2005,** *7*, (1), 1-9.

131. Lado Ribeiro, A. R.; Moreira, N. F. F.; Li Puma, G.; Silva, A. M. T., Impact of water matrix on the removal of micropollutants by advanced oxidation technologies. *Chemical Engineering Journal* **2019,** *363*, 155-173.

132. Wang, Y.; Roddick, F. A.; Fan, L., Direct and indirect photolysis of seven micropollutants in secondary effluent from a wastewater lagoon. *Chemosphere* **2017,** *185*, 297-308.

133. Zhou, H.; Yan, S.; Lian, L.; Song, W., Triplet-state photochemistry of dissolved organic matter: Triplet-state energy distribution and surface electric charge conditions. *Environmental Science & Technology* **2019,** *53*, (5), 2482-2490.

134. Zhou, Z.; Chen, B.; Qu, X.; Fu, H.; Zhu, D., Dissolved black carbon as an efficient sensitizer in the photochemical transformation of 17*β*-estradiol in aqueous solution. *Environmental Science & Technology* **2018,** *52*, (18), 10391-10399.

135. Wang, J.; Chen, J.; Qiao, X.; Zhang, Y.-n.; Uddin, M.; Guo, Z., Disparate effects of DOM extracted from coastal seawaters and freshwaters on photodegradation of 2,4-Dihydroxybenzophenone. *Water Research* **2019,** *151*, 280-287.

136. Kopinke, F.-D.; Georgi, A., What controls selectivity of hydroxyl radicals in aqueous solution? Indications for a cage effect. *The Journal of Physical Chemistry A* **2017,** *121*, (41), 7947-7955.

137. Hinojosa Guerra, M. M.; Oller Alberola, I.; Malato Rodriguez, S.; Agüera López, A.; Acevedo Merino, A.; Quiroga Alonso, J. M., Oxidation mechanisms of amoxicillin and paracetamol in the photo-Fenton solar process. *Water Research* **2019**.

138. Hsu, M.-H.; Kuo, T.-H.; Chen, Y.-E.; Huang, C.-H.; Hsu, C.-C.; Lin, A. Y.-C., Substructure reactivity affecting the manganese dioxide oxidation of cephalosporins. *Environmental Science & Technology* **2018,** *52*, (16), 9188-9195.

139. Yan, J.; Li, J.; Peng, J.; Zhang, H.; Zhang, Y.; Lai, B., Efficient degradation of sulfamethoxazole by the $CuO@Al_2O_3$ (EPC) coupled PMS system: Optimization, degradation pathways and toxicity evaluation. *Chemical Engineering Journal* **2019,** *359*, 1097-1110.

140. Chen, P.; Zhang, Q.; Shen, L.; Li, R.; Tan, C.; Chen, T.; Liu, H.; Liu, Y.; Cai, Z.; Liu, G.; Lv, W., Insights into the synergetic mechanism of a combined vis-RGO/TiO_2/peroxodisulfate system for the degradation of PPCPs: Kinetics, environmental factors and products. *Chemosphere* **2019,** *216*, 341-351.

141. Piccinno, F.; Gottschalk, F.; Seeger, S.; Nowack, B., Industrial production quantities and uses of ten engineered nanomaterials in Europe and the world. *Journal of Nanoparticle Research* **2012,** *14*, (9), 1109.

142. Stegemeier, J. P.; Colman, B. P.; Schwab, F.; Wiesner, M. R.; Lowry, G. V., Uptake and distribution of silver in the aquatic plant *Landoltia punctata* (Duckweed) exposed to silver and silver sulfide nanoparticles. *Environmental Science & Technology* **2017,** *51*, (9), 4936-4943.

143. Li, C. C.; Dang, F.; Li, M.; Zhu, M.; Zhong, H.; Hintelmann, H.; Zhou, D. M., Effects of exposure pathways on the accumulation and phytotoxicity of silver nanoparticles in soybean and rice. *Nanotoxicology* **2017,** *11*, (5), 699-709.

144. Saleeb, N.; Gooneratne, R.; Cavanagh, J.; Bunt, C.; Hossain, A. K. M. M.; Gaw, S.; Robinson, B., The mobility of silver nanoparticles and silver ions in the soil-plant system. *Journal of Environmental Quality* **2019,** *48*, (6), 1835-1841.

145. Dimkpa, C. O.; McLean, J. E.; Martineau, N.; Britt, D. W.; Haverkamp, R.; Anderson, A. J., Silver nanoparticles disrupt wheat (*Triticum aestivum* L.) growth in a sand matrix. *Environmental Science & Technology* **2013,** *47*, (2), 1082-1090.

146. Yang, Q.; Shan, W.; Hu, L.; Zhao, Y.; Hou, Y.; Yin, Y.; Liang, Y.; Wang, F.; Cai, Y.; Liu, J.; Jiang, G., Uptake and transformation of silver nanoparticles and ions by rice plants revealed by dual stable isotope tracing. *Environmental Science & Technology* **2019,** *53*, (2), 625-633.

147. Pradas del Real, A. E.; Vidal, V.; Carrière, M.; Castillo-Michel, H.; Levard, C.; Chaurand, P.; Sarret, G., Silver nanoparticles and wheat roots: A complex interplay. *Environmental Science & Technology* **2017,** *51*, (10), 5774-5782.

148. Geisler-Lee, J.; Wang, Q.; Yao, Y.; Zhang, W.; Geisler, M.; Li, K.; Huang, Y.; Chen, Y.; Kolmakov, A.; Ma, X., Phytotoxicity, accumulation and transport of silver nanoparticles by *Arabidopsis thaliana*. *Nanotoxicology* **2012,** *7*, (3), 323-337.

149. Ma, X.; Yan, J., Plant uptake and accumulation of engineered metallic nanoparticles from lab to field conditions. *Current Opinion in Environmental Science & Health* **2018,** *6*, 16-20.

150. Li, Y.; Chen, H.; Wang, F.; Zhao, F.; Han, X.; Geng, H.; Gao, L.; Chen, H.; Yuan, R.; Yao, J., Environmental behavior and associated plant accumulation of silver nanoparticles in the presence of dissolved humic and fulvic acid. *Environmental Pollution* **2018,** *243*, 1334-1342.

151. Zhang, W.; Musante, C.; White, J. C.; Schwab, P.; Wang, Q.; Ebbs, S. D.; Ma, X., Bioavailability of cerium oxide nanoparticles to *Raphanus sativus* L. in two soils. *Plant Physiology and Biochemistry* **2017,** *110*, 185-193.

152. Li, M.; Wang, P.; Dang, F.; Zhou, D.-M., The transformation and fate of silver nanoparticles in paddy soil: Effects of soil organic matter and redox conditions. *Environmental Science: Nano* **2017,** *4*, (4), 919-928.

153. Rauret, G.; López-Sánchez, J. F.; Sahuquillo, A.; Rubio, R.; Davidson, C.; Ure, A.; Quevauviller, P., Improvement of the BCR three step sequential extraction procedure prior to the certification of new sediment and soil reference materials. *Journal of Environmental Monitoring* **1999,** *1*, (1), 57-61.

154. Ure, A. M.; Quevauviller, P.; Muntau, H.; Griepink, B., Speciation of heavy metals in soils and sediments. An account of the improvement and harmonization of extraction techniques undertaken under the Auspices of the BCR of the Commission of the European Communities. *International Journal of Environmental Analytical Chemistry* **1993,** *51*, (1-4), 135-151.

155. Zhang, W.; Dan, Y.; Shi, H.; Ma, X., Effects of aging on the fate and bioavailability of cerium oxide nanoparticles to radish (*Raphanus sativus L.*) in soil. *ACS Sustainable Chemistry & Engineering* **2016,** *4*, (10), 5424-5431.

156. Zhong, X.-l.; Zhou, S.-l.; Zhu, Q.; Zhao, Q.-g., Fraction distribution and bioavailability of soil heavy metals in the Yangtze River Delta—A case study of Kunshan City in Jiangsu Province, China. *Journal of Hazardous Materials* **2011,** *198*, 13-21.

157. Choleva, T. G.; Tsogas, G. Z.; Vlessidis, A. G.; Giokas, D. L., Development of a sequential extraction and speciation procedure for assessing the mobility and fractionation of metal nanoparticles in soils. *Environmental Pollution* **2020,** *263*, 114407.

158. Thuesombat, P.; Hannongbua, S.; Akasit, S.; Chadchawan, S., Effect of silver nanoparticles on rice (*Oryza sativa* L. cv. *KDML 105*) seed germination and seedling growth. *Ecotoxicology and Environmental Safety* **2014,** *104*, 302-309.

159. Holden, P. A.; Gardea-Torresdey, J. L.; Klaessig, F.; Turco, R. F.; Mortimer, M.; Hund-Rinke, K.; Cohen Hubal, E. A.; Avery, D.; Barceló, D.; Behra, R.; Cohen, Y.; Deydier-Stephan, L.; Ferguson, P. L.; Fernandes, T. F.; Herr Harthorn, B.; Henderson, W. M.; Hoke, R. A.; Hristozov, D.; Johnston, J. M.; Kane, A. B.; Kapustka, L.; Keller, A. A.; Lenihan, H. S.; Lovell, W.; Murphy, C. J.; Nisbet, R. M.; Petersen, E. J.; Salinas, E. R.; Scheringer, M.; Sharma, M.; Speed, D. E.; Sultan, Y.; Westerhoff, P.; White, J. C.; Wiesner, M. R.; Wong, E. M.; Xing, B.; Steele Horan, M.; Godwin, H. A.; Nel, A. E., Considerations of environmentally relevant test conditions for improved evaluation of ecological hazards of engineered nanomaterials. *Environmental Science & Technology* **2016,** *50*, (12), 6124-6145.

160. Holden, P. A.; Klaessig, F.; Turco, R. F.; Priester, J. H.; Rico, C. M.; Avila-Arias, H.; Mortimer, M.; Pacpaco, K.; Gardea-Torresdey, J. L., Evaluation of exposure concentrations used in assessing manufactured nanomaterial environmental hazards: Are they relevant? *Environmental Science & Technology* **2014,** *48*, (18), 10541-10551.

161. He, J.; Wang, D.; Zhou, D., Transport and retention of silver nanoparticles in soil: Effects of input concentration, particle size and surface coating. *Science of The Total Environment* **2019,** *648*, 102-108.

162. Li, Y.; He, J.; Qi, H.; Li, H.; Boyd, S. A.; Zhang, W., Impact of biochar amendment on the uptake, fate and bioavailability of pharmaceuticals in soil-radish systems. *Journal of Hazardous Materials* **2020,** *398*, 122852.

163. Deng, R.; Lin, D.; Zhu, L.; Majumdar, S.; White, J. C.; Gardea-Torresdey, J. L.; Xing, B., Nanoparticle interactions with co-existing contaminants: Joint toxicity, bioaccumulation and risk. *Nanotoxicology* **2017,** *11*, (5), 591-612.

164. Li, Y.; Sallach, J. B.; Zhang, W.; Boyd, S. A.; Li, H., Insight into the distribution of pharmaceuticals in soil-water-plant systems. *Water Research* **2019,** *152*, 38-46.

165. Wang, Z.; Shan, X.-q.; Zhang, S., Comparison between fractionation and bioavailability of trace elements in rhizosphere and bulk soils. *Chemosphere* **2002,** *46*, (8), 1163-1171.

166. Cornelis, G.; Kirby, J. K.; Beak, D.; Chittleborough, D.; McLaughlin, M. J., A method for determination of retention of silver and cerium oxide manufactured nanoparticles in soils. *Environmental Chemistry* **2010,** *7*, (3), 298-308.

167. Yang, J.; Jiang, F.; Ma, C.; Rui, Y.; Rui, M.; Adeel, M.; Cao, W.; Xing, B., Alteration of crop yield and quality of wheat upon exposure to silver nanoparticles in a life cycle study. *Journal of Agricultural and Food Chemistry* **2018,** *66*, (11), 2589-2597.

168. Rawat, S.; Pullagurala, V. L. R.; Hernandez-Molina, M.; Sun, Y.; Niu, G.; Hernandez-Viezcas, J. A.; Peralta-Videa, J. R.; Gardea-Torresdey, J. L., Impacts of copper oxide nanoparticles on bell pepper (*Capsicum annum* L.) plants: a full life cycle study. *Environmental Science: Nano* **2018,** *5*, (1), 83-95.

169. Wang, R.; Du, H.; Wang, Y.; Wang, D.; Sun, Q.; Zhou, D., Retention of silver nanoparticles and silver ion to natural soils: Effects of soil physicochemical properties. *Journal of Soils and Sediments* **2018,** *18*, (7), 2491-2499.

170. Cornelis, G.; DooletteMadeleine Thomas, C.; McLaughlin, M. J.; Kirby, J. K.; Beak, D. G.; Chittleborough, D., Retention and dissolution of engineered silver nanoparticles in natural soils. *Soil Science Society of America Journal* **2012,** *76*, (3), 891-902.

171. Hoppe, M.; Mikutta, R.; Utermann, J.; Duijnisveld, W.; Guggenberger, G., Retention of sterically and electrosterically stabilized silver nanoparticles in soils. *Environmental Science & Technology* **2014,** *48*, (21), 12628-12635.

172. Jacobson, A. R.; McBride, M. B.; Baveye, P.; Steenhuis, T. S., Environmental factors determining the trace-level sorption of silver and thallium to soils. *Science of The Total Environment* **2005,** *345*, (1), 191-205.

173. Wang, D.; Zhang, W.; Hao, X.; Zhou, D., Transport of biochar particles in saturated granular media: Effects of pyrolysis temperature and particle size. *Environmental Science & Technology* **2013,** *47*, (2), 821-828.

174. Dong, X.; Ma, L. Q.; Li, Y., Characteristics and mechanisms of hexavalent chromium removal by biochar from sugar beet tailing. *Journal of Hazardous Materials* **2011,** *190*, (1), 909-915.

175. Klüpfel, L.; Keiluweit, M.; Kleber, M.; Sander, M., Redox properties of plant biomass-derived black carbon (biochar). *Environmental Science & Technology* **2014,** *48*, (10), 5601-5611.

176. Prévoteau, A.; Ronsse, F.; Cid, I.; Boeckx, P.; Rabaey, K., The electron donating capacity of biochar is dramatically underestimated. *Scientific Reports* **2016,** *6*, (1), 32870.

177. Xu, X.; Huang, H.; Zhang, Y.; Xu, Z.; Cao, X., Biochar as both electron donor and electron shuttle for the reduction transformation of Cr(VI) during its sorption. *Environmental Pollution* **2019,** *244*, 423-430.

178. Yang, Y.; Li, S.; Bi, X.; Wu, P.; Liu, T.; Li, F.; Liu, C., Lead, Zn, and Cd in slags, stream sediments, and soils in an abandoned Zn smelting region, southwest of China, and Pb and S isotopes as source tracers. *Journal of Soils and Sediments* **2010,** *10*, (8), 1527-1539.

179. Zhang, S.; Song, J.; Cheng, Y.; Lv, M., Proper management of lead-contaminated agricultural lands against the exceedance of lead in agricultural produce: Derivation of local soil criteria. *Science of The Total Environment* **2018,** *634*, 321-330.

180. Jamieson, T.; Sager, E.; Guéguen, C., Characterization of biochar-derived dissolved organic matter using UV–visible absorption and excitation–emission fluorescence spectroscopies. *Chemosphere* **2014,** *103*, 197-204.

181. Liu, C.-H.; Teppen, B. J.; Mao, J.; Lehmann, J.; Zhang, W., Quantification and characterization of dissolved organic carbon from biochars. *Geoderma* **2019,** *335*, 161-169.

182. Qu, X.; Fu, H.; Mao, J.; Ran, Y.; Zhang, D.; Zhu, D., Chemical and structural properties of dissolved black carbon released from biochars. *Carbon* **2016,** *96*, 759-767.

183. Römkens, P. F.; Guo, H.-Y.; Chu, C.-L.; Liu, T.-S.; Chiang, C.-F.; Koopmans, G. F., Characterization of soil heavy metal pools in paddy fields in Taiwan: Chemical extraction and solid-solution partitioning. *Journal of Soils and Sediments* **2009,** *9*, (3), 216-228.

184. Bose, S.; Bhattacharyya, A. K., Heavy metal accumulation in wheat plant grown in soil amended with industrial sludge. *Chemosphere* **2008,** *70*, (7), 1264-1272.

185. Gao, X.; Avellan, A.; Laughton, S.; Vaidya, R.; Rodrigues, S. M.; Casman, E. A.; Lowry, G. V., CuO nanoparticle dissolution and toxicity to wheat (*Triticum aestivum*) in rhizosphere soil. *Environmental Science & Technology* **2018,** *52*, (5), 2888-2897.

186. Chen, H.; Yada, R., Nanotechnologies in agriculture: New tools for sustainable development. *Trends in Food Science & Technology* **2011,** *22*, (11), 585-594.

187. Ghormade, V.; Deshpande, M. V.; Paknikar, K. M., Perspectives for nano-biotechnology enabled protection and nutrition of plants. *Biotechnology Advances* **2011,** *29*, (6), 792-803.

188. Khot, L. R.; Sankaran, S.; Maja, J. M.; Ehsani, R.; Schuster, E. W., Applications of nanomaterials in agricultural production and crop protection: A review. *Crop Protection* **2012,** *35*, 64-70.

189. Morones, J. R.; Elechiguerra, J. L.; Camacho, A.; Holt, K.; Kouri, J. B.; Ramírez, J. T.; Yacaman, M. J., The bactericidal effect of silver nanoparticles. *Nanotechnology* **2005,** *16*, (10), 2346-2353.

190. Keller, A. A.; Lazareva, A., Predicted releases of engineered nanomaterials: From global to regional to local. *Environmental Science & Technology Letters* **2014,** *1*, (1), 65-70.

191. Zhang, Z.; Kong, F.; Vardhanabhuti, B.; Mustapha, A.; Lin, M., Detection of engineered silver nanoparticle contamination in pears. *Journal of Agricultural and Food Chemistry* **2012,** *60*, (43), 10762-10767.

192. Rico, C. M.; Majumdar, S.; Duarte-Gardea, M.; Peralta-Videa, J. R.; Gardea-Torresdey, J. L., Interaction of nanoparticles with edible plants and their possible implications in the food chain. *Journal of Agricultural and Food Chemistry* **2011,** *59*, (8), 3485-3498.

193. Ovissipour, M.; Sablani, S. S.; Rasco, B., Engineered nanoparticle adhesion and removal from tomato surfaces. *Journal of Agricultural and Food Chemistry* **2013,** *61*, (42), 10183-10190.

194. Miralles, P.; Church, T. L.; Harris, A. T., Toxicity, uptake, and translocation of engineered nanomaterials in vascular plants. *Environmental Science & Technology* **2012,** *46*, (17), 9224-9239.

195. Spielman-Sun, E.; Lombi, E.; Donner, E.; Avellan, A.; Etschmann, B.; Howard, D.; Lowry, G. V., Temporal evolution of copper distribution and speciation in roots of *Triticum aestivum* exposed to CuO, $Cu(OH)_2$, and CuS nanoparticles. *Environmental Science & Technology* **2018,** *52*, (17), 9777-9784.

196. Dwivedi, A. D.; Yoon, H.; Singh, J. P.; Chae, K. H.; Rho, S.-c.; Hwang, D. S.; Chang, Y.-S., Uptake, distribution, and transformation of zerovalent iron nanoparticles in the edible plant *Cucumis sativus*. *Environmental Science & Technology* **2018,** *52*, (17), 10057-10066.

197. Eichert, T.; Goldbach, H. E., Equivalent pore radii of hydrophilic foliar uptake routes in stomatous and astomatous leaf surfaces – further evidence for a stomatal pathway. *Physiologia Plantarum* **2008,** *132*, (4), 491-502.

198. Larue, C.; Castillo-Michel, H.; Sobanska, S.; Trcera, N.; Sorieul, S.; Cécillon, L.; Ouerdane, L.; Legros, S.; Sarret, G., Fate of pristine TiO_2 nanoparticles and aged paint-containing TiO_2 nanoparticles in lettuce crop after foliar exposure. *Journal of Hazardous Materials* **2014,** *273*, 17-26.

199. Zhao, L.; Huang, Y.; Adeleye, A. S.; Keller, A. A., Metabolomics reveals $Cu(OH)_2$ nanopesticide-activated anti-oxidative pathways and decreased beneficial antioxidants in spinach leaves. *Environmental Science & Technology* **2017,** *51*, (17), 10184-10194.

200. Schwab, F.; Zhai, G.; Kern, M.; Turner, A.; Schnoor, J. L.; Wiesner, M. R., Barriers, pathways and processes for uptake, translocation and accumulation of nanomaterials in plants – Critical review. *Nanotoxicology* **2016,** *10*, (3), 257-278.

201. Raliya, R.; Nair, R.; Chavalmane, S.; Wang, W.-N.; Biswas, P., Mechanistic evaluation of translocation and physiological impact of titanium dioxide and zinc oxide nanoparticles on the tomato (Solanum lycopersicum L.) plant. *Metallomics* **2015,** *7*, (12), 1584-1594.

202. Savvides, A.; Fanourakis, D.; van Ieperen, W., Co-ordination of hydraulic and stomatal conductances across light qualities in cucumber leaves. *Journal of Experimental Botany* **2011,** *63*, (3), 1135-1143.

203. Wang, W.-N.; Tarafdar, J. C.; Biswas, P., Nanoparticle synthesis and delivery by an aerosol route for watermelon plant foliar uptake. *Journal of Nanoparticle Research* **2013,** *15*, (1), 1417.

204. Hong, J.; Peralta-Videa, J. R.; Rico, C.; Sahi, S.; Viveros, M. N.; Bartonjo, J.; Zhao, L.; Gardea-Torresdey, J. L., Evidence of translocation and physiological impacts of foliar applied CeO_2 nanoparticles on cucumber (*Cucumis sativus*) plants. *Environmental Science & Technology* **2014,** *48*, (8), 4376-4385.

205. Birbaum, K.; Brogioli, R.; Schellenberg, M.; Martinoia, E.; Stark, W. J.; Günther, D.; Limbach, L. K., No evidence for cerium dioxide nanoparticle translocation in maize plants. *Environmental Science & Technology* **2010,** *44*, (22), 8718-8723.

206. Melotto, M.; Underwood, W.; Koczan, J.; Nomura, K.; He, S. Y., Plant stomata function in innate immunity against bacterial invasion. *Cell* **2006,** *126*, (5), 969-980.

207. Fan, L.-M.; Zhao, Z.; Assmann, S. M., Guard cells: A dynamic signaling model. *Current Opinion in Plant Biology* **2004,** *7*, (5), 537-546.

208. Julian I Schroeder; Gethyn J Allen; Veronique Hugouvieux; June M Kwak, a.; Waner, D., Guard cell signal transduction. *Annual Review of Plant Physiology and Plant Molecular Biology* **2001,** *52*, (1), 627-658.

209. Zeng, W.; Brutus, A.; Kremer, J. M.; Withers, J. C.; Gao, X.; Jones, A. D.; He, S. Y., A genetic screen reveals Arabidopsis stomatal and/or apoplastic defenses against *Pseudomonas syringae* pv. *tomato* DC3000. *PLoS pathogens* **2011,** *7*, (10), e1002291-e1002291.

210. Zhang, L.; Paasch, B. C.; Chen, J.; Day, B.; He, S. Y., An important role of l-fucose biosynthesis and protein fucosylation genes in Arabidopsis immunity. *New Phytologist* **2019,** *222*, (2), 981-994.

211. Yang, X.; Pan, H.; Wang, P.; Zhao, F.-J., Particle-specific toxicity and bioavailability of cerium oxide (CeO_2) nanoparticles to *Arabidopsis thaliana*. *Journal of Hazardous Materials* **2017,** *322*, 292-300.

212. Chen, T.; Nomura, K.; Wang, X.; Sohrabi, R.; Xu, J.; Yao, L.; Paasch, B. C.; Ma, L.; Kremer, J.; Cheng, Y.; Zhang, L.; Wang, N.; Wang, E.; Xin, X.-F.; He, S. Y., A plant genetic network for preventing dysbiosis in the phyllosphere. *Nature* **2020,** *580*, (7805), 653-657.

213. Abraham, P. M.; Barnikol, S.; Baumann, T.; Kuehn, M.; Ivleva, N. P.; Schaumann, G. E., Sorption of silver nanoparticles to environmental and model surfaces. *Environmental Science & Technology* **2013,** *47*, (10), 5083-5091.

214. Arora, S.; Sharma, P.; Kumar, S.; Nayan, R.; Khanna, P. K.; Zaidi, M. G. H., Gold-nanoparticle induced enhancement in growth and seed yield of *Brassica juncea*. *Plant Growth Regulation* **2012,** *66*, (3), 303-310.

215. Avellan, A.; Yun, J.; Zhang, Y.; Spielman-Sun, E.; Unrine, J. M.; Thieme, J.; Li, J.; Lombi, E.; Bland, G.; Lowry, G. V., Nanoparticle size and coating chemistry control foliar uptake pathways, translocation, and leaf-to-rhizosphere transport in wheat. *ACS Nano* **2019,** *13*, (5), 5291-5305.

216. Raliya, R.; Franke, C.; Chavalmane, S.; Nair, R.; Reed, N.; Biswas, P., Quantitative understanding of nanoparticle uptake in watermelon plants. *Frontiers in Plant Science* **2016,** *7*, (1288).

217. Shen, C.; Li, B.; Wang, C.; Huang, Y.; Jin, Y., Surface roughness effect on deposition of nano-and micro-sized colloids in saturated columns at different solution ionic strengths. *Vadose Zone Journal* **2011,** *10*, (3), 1071-1081.

218. Shen, C.; Wang, F.; Li, B.; Jin, Y.; Wang, L.-P.; Huang, Y., Application of DLVO energy map to evaluate interactions between spherical colloids and rough surfaces. *Langmuir* **2012,** *28*, (41), 14681-14692.

219. Fernandes, P. É.; São José, J. F. B.; Zerdas, E. R. M. A.; Andrade, N. J.; Fernandes, C. M.; Silva, L. D., Influence of the hydrophobicity and surface roughness of mangoes and tomatoes on the adhesion of *Salmonella enterica* serovar Typhimurium and evaluation of cleaning procedures using surfactin. *Food Control* **2014,** *41*, 21-26.

220. Zhai, G.; Walters, K. S.; Peate, D. W.; Alvarez, P. J. J.; Schnoor, J. L., Transport of gold nanoparticles through plasmodesmata and precipitation of gold ions in woody poplar. *Environmental Science & Technology Letters* **2014,** *1*, (2), 146-151.

221. Kohan-Baghkheirati, E.; Geisler-Lee, J., Gene expression, protein function and pathways of Arabidopsis thaliana responding to silver nanoparticles in comparison to silver ions, cold, salt, drought, and heat. *Nanomaterials* **2015,** *5*, (2), 436-467.

222. Narayanan, K. B.; Sakthivel, N., Green synthesis of biogenic metal nanoparticles by terrestrial and aquatic phototrophic and heterotrophic eukaryotes and biocompatible agents. *Advances in Colloid and Interface Science* **2011,** *169*, (2), 59-79.